SECURITY INFORMATION

218
Copy
RM L51J15

[redacted]

NACA

RESEARCH MEMORANDUM

TESTS AT MACH NUMBER 1.62 OF A SERIES OF MISSILE CONFIGURATIONS HAVING TANDEM CRUCIFORM LIFTING SURFACES

By Carl E. Grigsby

Langley Aeronautical Laboratory
Langley Field, Va.

[redacted]

NATIONAL ADVISORY COMMITTEE FOR AERONAUTICS
WASHINGTON
January 11, 1952

[redacted]

Classification cancelled (or changed to UNCLASSIFIED)

By Author NASA Tech Pub Announcement #124

(OFFICER AUTHORIZED TO CHANGE) 4 Nov 57

By NMB

GRADE OF OFFICER MAKING CHANGE)

30 Mar 61

DATE

NATIONAL ADVISORY COMMITTEE FOR AERONAUTICS

RESEARCH MEMORANDUM

TESTS AT MACH NUMBER 1.62 OF A SERIES OF MISSILE CONFIGURATIONS HAVING TANDEM CRUCIFORM LIFTING SURFACES

By Carl E. Grigsby

SUMMARY

An investigation at a Mach number of 1.62 was made in the Langley 9-inch supersonic tunnel of a series of missile configurations having tandem lifting surfaces of low aspect ratio and of nearly equal span. Some of the variables investigated were interdigitation angle, wing and tail plan form, and longitudinal location of wing with respect to tail. All configurations were tested through an angle-of-attack range from -5° to 15° at roll angles of 0° and 45°. Lift, drag, and pitching-moment data are presented, together with center-of-pressure locations and tail-lift efficiency factors.

INTRODUCTION

As part of a missile development program, an investigation has been made in the Langley 9-inch supersonic tunnel of a number of missile configurations. Breakdown tests were made on a total of ten configurations comprising combinations of five wings and six tails at 0° and 45° angle of roll. For each configuration, tests were made with two longitudinal wing locations relative to the tail and with wings in line and interdigitated 45° with respect to the tail. In order to expedite release of these data, no analyses of results are presented.

SYMBOLS

S	maximum cross-sectional area of body
d	maximum body diameter
r	radius
x	distance from nose of body
α	angle of attack
ϕ	angle of roll of model relative to angle-of-attack plane, positive when model, viewed from rear, is rotated clockwise ($\phi = 0^\circ$ when opposite tail panels are in angle-of-attack plane)
θ	angle between a plane through opposite tail panels and a plane through opposite wing panels, positive when wings are rotated clockwise with respect to tails, when the model is viewed from rear. The angle θ is always less than 90°, and its value appears as the superscript for W in the complete-model-configuration designations.
T_o	stagnation temperature
p_o	stagnation pressure
M	Mach number
ρ	stream density
V	velocity
q	dynamic pressure $\left(\frac{\rho V^2}{2}\right)$
R	Reynolds number
C_L	lift coefficient $\left(\frac{\text{Lift}}{qS}\right)$
C_D	drag coefficient $\left(\frac{\text{Drag}}{qS}\right)$
C_m	pitching-moment coefficient $\left(\frac{\text{Moment about center of gravity}}{qSd}\right)$

c.p. center of pressure; distance measured in body diameters from center of gravity unless otherwise specified

η_t tail-lift efficiency factor

B configuration of body

BT configuration of body and tails

BW configuration of body and wings

BWT configuration of body, wings, and tails

Subscripts:

1,2,...6 refers to a particular wing or tail plan form (see figs. 1 and 2)

F wing in forward location

min minimum

R wing in rear location

α slope of coefficient curve referred to angle of attack

Superscripts:

Numerical superscript for W gives value of θ. (See definition of θ.)

APPARATUS AND MODELS

The Langley 9-inch supersonic tunnel is a closed-return, direct-drive type in which the pressure and humidity are controlled. The test Mach number is varied by means of interchangeable nozzle blocks forming test sections approximately 9 inches square. Eleven fine-mesh turbulence-damping screens are provided in the settling chamber ahead of the nozzles. During the tests the amount of water vapor in the tunnel air was kept at sufficiently low values so that the effects of condensation in the supersonic nozzle were negligible.

A drawing of the models showing the relative locations of the wings and tails is presented in figure 1. A detailed drawing of the wings and tails is given in figure 2, and the principal dimensions and areas are

given in table I. It should be noted that the W_1 and T_1 surfaces differ from the W_2 and T_2 surfaces only in the thickness ratio and leading-edge bevel.

The sting and sting-windshield arrangement used in these tests is shown in figure 3. At each angle of attack, the model, sting, and sting windshield were translated across the tunnel so that a fixed point on the model could be kept on the center line of the tunnel. By use of this arrangement, configurations which at 0° angle of attack were free from shock reflections could be tested through the whole angle range of $\pm 15^{\circ}$. Throughout the tests the gap between the rear of the model and the movable windshield was maintained at less than 0.010 inch.

TEST METHODS

Measurements of lift, drag, and pitching moment were made by means of external self-balancing mechanical scales through an angle-of-attack range of -5° to 15°. An optical system employing a small mirror mounted in the rear of the body was used to measure angles of attack. Measurements were made of the pressure in the sting-shield-and-balance enclosing box, which tests have shown to be equal to the model base pressure, and the drag results were corrected to the condition of base pressure equal to stream pressure.

The test conditions were as follows:

M	1.62
T_o, °F	100
p_o, atm	1
q, lb/sq ft	890
R, per inch	0.348×10^6

PRECISION OF DATA

The precision of the data has been evaluated by estimating the uncertainties in the balance measurements involved in a given quantity and combining these errors by a method based on the theory of least squares.

A summary table of precision estimates follows:

Lift coefficient, C_L	± 0.0024
Drag coefficient, C_D	± 0.0033
Pitching-moment coefficient, C_m	± 0.035
Angle of attack, α	$\pm 0.01^\circ$
Mach number, M	± 0.01

The precision of the calculated quantities - center-of-pressure location and tail efficiency - which were obtained from faired curves varies with each configuration and with angle of attack. Because these quantities are obtained by division, the errors would be largest in the low-angle-of-attack range. The errors are not as great at 0° angle of attack, however, because slope values were used in the computations. Thus, the greatest doubt exists in the shape of the curves between 0° and 4° angle of attack.

PRESENTATION OF DATA

The basic lift, drag, and pitching-moment data are presented in figures 4 to 20. The pitching-moment coefficients are referenced to the center-of-gravity location shown in figure 1. As an aid in locating the figures, they are listed in table II in order of presentation. The lift and pitching-moment slopes at 0° angle of attack, together with the minimum drag coefficients for all configurations, are summarized in table III. Although the data are presented without analysis, they have been reduced to show the variation of center-of-pressure location and tail-lift efficiency factor. These results are shown in figures 21 to 31. The tail-lift efficiency factor η_t was obtained from the lift results as follows:

$$\eta_t = \frac{C_{L_{BWT}} - C_{L_{BW}}}{C_{L_{BT}} - C_{L_B}}$$

The center-of-pressure characteristics of the incremental wing lift are presented in figure 32. The location of the center of pressure of the lift due to adding the wing is obtained from the relation

$$\text{c.p.} = \frac{C_{m_{BW}} - C_{m_B}}{C_{L_{BW}} - C_{L_B}}$$

Langley Aeronautical Laboratory
National Advisory Committee for Aeronautics
Langley Field, Va.

TABLE I.- MODEL DIMENSIONS

Plan form	L.E. sweep (deg)	T.E. sweep (deg)	Total span (in.)	Root chord (in.)	Tip chord (in.)	Thickness (% root chord)	Area (sq in.)		Aspect ratio	
							Total	Exposed	Total	Exposed
W_1 and T_1	0	0	2.00	1.00	1.00	6	2.00	1.30	2.00	1.30
W_2 and T_2	0	0	2.00	1.00	1.00	3	2.00	1.30	2.00	1.30
W_3	0	0	2.00	1.50	1.50	2	3.00	1.95	1.33	.87
*T_3	-	-	2.00	.52	.52	6	----	----	----	----
T_6	0	0	2.83	.62	.62	5	1.75	1.32	4.57	3.44
W_4 and T_4	0	-57	2.00	1.00	0	3	----	.65	----	2.60
W_5 and T_5	57	0	2.00	1.00	0	3	----	.65	----	2.60

*T_3 is a strut-supported ring of 2.00-inch diameter and 0.52-inch chord. (See detail on fig. 2.)

Fuselage ordinates:

Station 0 to 3.125 . . . . $r = 1.40\left[\frac{x}{6.25} - \left(\frac{x}{6.25}\right)^2\right]$

Station 3.125 to 9.000 . . . . Constant diameter of 0.700

TABLE II.- INDEX OF FIGURES

Figure	Legend
1	Detail of models.
2	Detail of wings and tails.
3	Model installation in tunnel.
4	Lift, drag, and pitching-moment characteristics of body alone.
5	Lift, drag, and pitching-moment characteristics of model combinations of B and T.
6	Lift, drag, and pitching-moment characteristics of model combinations of B and W_1.
7	Lift, drag, and pitching-moment characteristics of model combinations of B and W_2.
8	Lift, drag, and pitching-moment characteristics of model combinations of B and W_3.
9	Lift, drag, and pitching-moment characteristics of model combinations of B and W_4.
10	Lift, drag, and pitching-moment characteristics of model combinations of B and W_5.
11	Lift, drag, and pitching-moment characteristics of model combinations of B, W_1, and T_1.
12	Lift, drag, and pitching-moment characteristics of model combinations of B, W_2, and T_2.
13	Lift, drag, and pitching-moment characteristics of model combinations of B, W_3, and T_2.
14	Lift, drag, and pitching-moment characteristics of model combinations of B, W_4, and T_4.
15	Lift, drag, and pitching-moment characteristics of model combinations of B, W_5, and T_4.
16	Lift, drag, and pitching-moment characteristics of model combinations of B, W_5, and T_5.

NACA

TABLE II.- INDEX OF FIGURES - Continued

Figure	Legend
17	Lift, drag, and pitching-moment characteristics of model combinations of B, W_2, and T_3.
18	Lift, drag, and pitching-moment characteristics of model combinations of B, W_3, and T_3.
19	Lift, drag, and pitching-moment characteristics of model combinations of B, W_2, and T_6.
20	Lift, drag, and pitching-moment characteristics of model combinations of B, W_3, and T_6.
21	Center-of-pressure characteristics and body-wing-tail interference factors for configurations having W_1 and T_1.
22	Center-of-pressure characteristics and body-wing-tail interference factors for configurations having W_2 and T_2.
23	Center-of-pressure characteristics and body-wing-tail interference factors for configurations having W_3 and T_2.
24	Center-of-pressure characteristics and body-wing-tail interference factors for configurations having W_4 and T_4.
25	Center-of-pressure characteristics and body-wing-tail interference factors for configurations having W_5 and T_4.
26	Center-of-pressure characteristics and body-wing-tail interference factors for configurations having W_5 and T_5.
27	Center-of-pressure characteristics and body-wing-tail interference factors for configurations having W_2 and T_3.
28	Center-of-pressure characteristics and body-wing-tail interference factors for configurations having W_3 and T_3.
29	Center-of-pressure characteristics and body-wing-tail interference factors for configurations having W_2 and T_6.
30	Center-of-pressure characteristics and body-wing-tail interference factors for configurations having W_3 and T_6.

TABLE II.- INDEX OF FIGURES - Concluded

Figure	Legend
31	Center-of-pressure characteristics of the body and BT configurations.
32	Center-of-pressure characteristics of the incremental wing lift, $\dfrac{C_{m_{BW}} - C_{m_B}}{C_{L_{BW}} - C_{L_B}}$.

TABLE III.- SUMMARY OF RESULTS

Configuration	$(C_{L_\alpha})_{L \to 0}$		$C_{D_{min}}$		$(C_{m_\alpha})_{L \to 0}$	
	$\phi = 0^\circ$	$\phi = 45^\circ$	$\phi = 0^\circ$	$\phi = 45^\circ$	$\phi = 0^\circ$	$\phi = 45^\circ$
B	0.0410	------	0.087	-----	0.170	------
BT_1	0.2610	0.2515	0.397	0.397	-1.082	-1.060
BT_2	.2425	.2425	.200	.200	-1.007	-1.007
BT_3	.3530	.3530	.475	.475	-1.843	-1.843
BT_4	.1623	.1623	.178	.178	-.523	-.523
BT_5	.1485	.1485	.140	.140	-.490	-.463
BT_6	.2640	.2650	.290	.328	-1.173	-1.173
BW_{1F}	0.2625	0.2560	0.458	0.458	0.415	0.438
BW_{1R}	.2650	.2650	.445	.445	-.058	-.058
BW_{2F}	.2590	.2590	.270	.270	.429	.420
BW_{2R}	.2660	.2660	.270	.258	-.069	-.054
BW_{3F}	.2955	.2965	.300	.289	.511	.511
BW_{3R}	.2890	.2890	.272	.262	-.025	-.041
BW_{4F}	.1535	.1535	.248	.248	.309	.323
BW_{4R}	.1535	.1535	.226	.226	.062	.074
BW_{5F}	.1590	.1575	.210	.210	.265	.253
BW_{5R}	.1580	.1545	.195	.195	0	0
$BW_{1F}{}^{0}T_1$	0.3240	0.3240	0.605	0.605	0.058	0.095
$BW_{1R}{}^{0}T_1$	.3225	.3205	.600	.600	-.430	-.364
$BW_{1F}{}^{45}T_1$	.4125	.4125	.600	.600	-.439	-.451
$BW_{1R}{}^{45}T_1$	.4185	.4185	.595	.595	-.962	-.925
$BW_{2F}{}^{0}T_2$	0.3110	0.3110	0.372	0.380	0.059	0.179
$BW_{2R}{}^{0}T_2$	.3100	.3000	.370	.370	-.339	-.305
$BW_{2F}{}^{45}T_2$	.4010	.4010	.375	.375	-.382	-.382
$BW_{2R}{}^{45}T_2$	.4090	.4090	.360	.360	-.905	-.905
$BW_{3F}{}^{0}T_2$	0.3080	0.3080	0.400	0.400	0.395	0.395
$BW_{3R}{}^{0}T_2$	.3080	.3080	.385	.385	-.123	-.123
$BW_{3F}{}^{45}T_2$	.4200	.4200	.397	.397	-.235	-.235
$BW_{3R}{}^{45}T_2$	.4300	.4300	.380	.380	-.813	-.813

NACA

TABLE III.- SUMMARY OF RESULTS - Concluded

Configuration	$(C_{L_\alpha})_{L \to 0}$		$C_{D_{min}}$		$(C_{m_\alpha})_{L \to 0}$	
	$\phi = 0^\circ$	$\phi = 45^\circ$	$\phi = 0^\circ$	$\phi = 45^\circ$	$\phi = 0^\circ$	$\phi = 45^\circ$
$BW_{4F}{}^{0}T_4$	0.2210	0.2140	0.330	0.330	-0.030	-0.030
$BW_{4R}{}^{0}T_4$	.2220	.2140	.310	.310	-.275	-.257
$BW_{4F}{}^{45}T_4$	.2505	.2505	.328	.328	-.252	-.229
$BW_{4R}{}^{45}T_4$	.2495	.2495	.310	.315	-.483	-.483
$BW_{5F}{}^{0}T_4$	0.2305	0.2255	0.295	0.280	-0.110	-0.086
$BW_{5R}{}^{0}T_4$	.2245	.2245	.275	.275	-.375	-.357
$BW_{5F}{}^{45}T_4$	.2610	.2610	.293	.293	-.303	-.303
$BW_{5R}{}^{45}T_4$	.2590	.2590	.275	.275	-.555	-.555
$BW_{5F}{}^{0}T_5$	0.2050	0.2020	0.260	0.260	-0.037	-0.030
$BW_{5R}{}^{0}T_5$	.2045	.2005	.250	.245	-.339	-.248
$BW_{5F}{}^{45}T_5$	.2400	.2400	.268	.268	-.262	-.246
$BW_{5R}{}^{45}T_5$	.2385	.2385	.260	.243	-.529	-.494
$BW_{2F}{}^{0}T_3$	0.4015	0.4015	0.655	0.655	-0.538	-0.538
$BW_{2R}{}^{0}T_3$	.4115	.4115	.633	.633	-1.101	-1.101
$BW_{2F}{}^{45}T_3$	.4425	.4425	.652	.652	-.759	-.786
$BW_{2R}{}^{45}T_3$	.4520	.4520	.640	.640	-1.308	-1.289
$BW_{3F}{}^{0}T_3$	0.4135	0.4135	0.680	0.680	-0.250	-0.274
$BW_{3R}{}^{0}T_3$	.4205	.4205	.662	.662	-.886	-.886
$BW_{3F}{}^{45}T_3$	.4470	.4470	.675	.675	-.533	-.521
$BW_{3R}{}^{45}T_3$	.4715	.4715	.668	.668	-1.181	-1.181
$BW_{2F}{}^{45}T_6$	0.4450	0.4450	0.458	0.458	-0.658	-0.658
$BW_{2R}{}^{45}T_6$	.4440	.4440	.445	.445	-1.157	-1.157
$BW_{3F}{}^{45}T_6$	0.4615	0.4615	0.485	0.485	-0.542	-0.521
$BW_{3R}{}^{45}T_6$	.4740	.4740	.468	.468	-1.111	-1.111

NACA

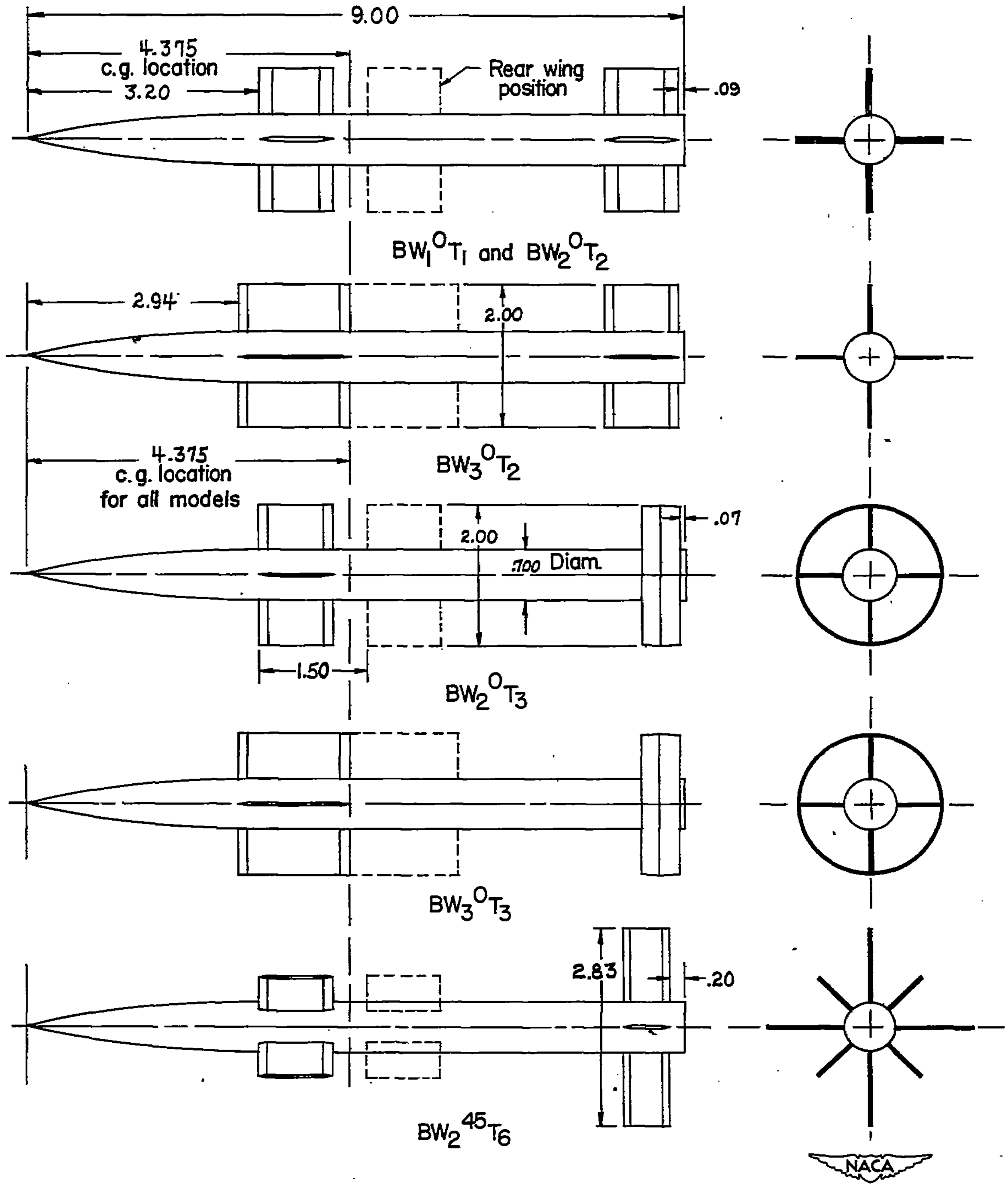

Figure 1.- Detail of models.

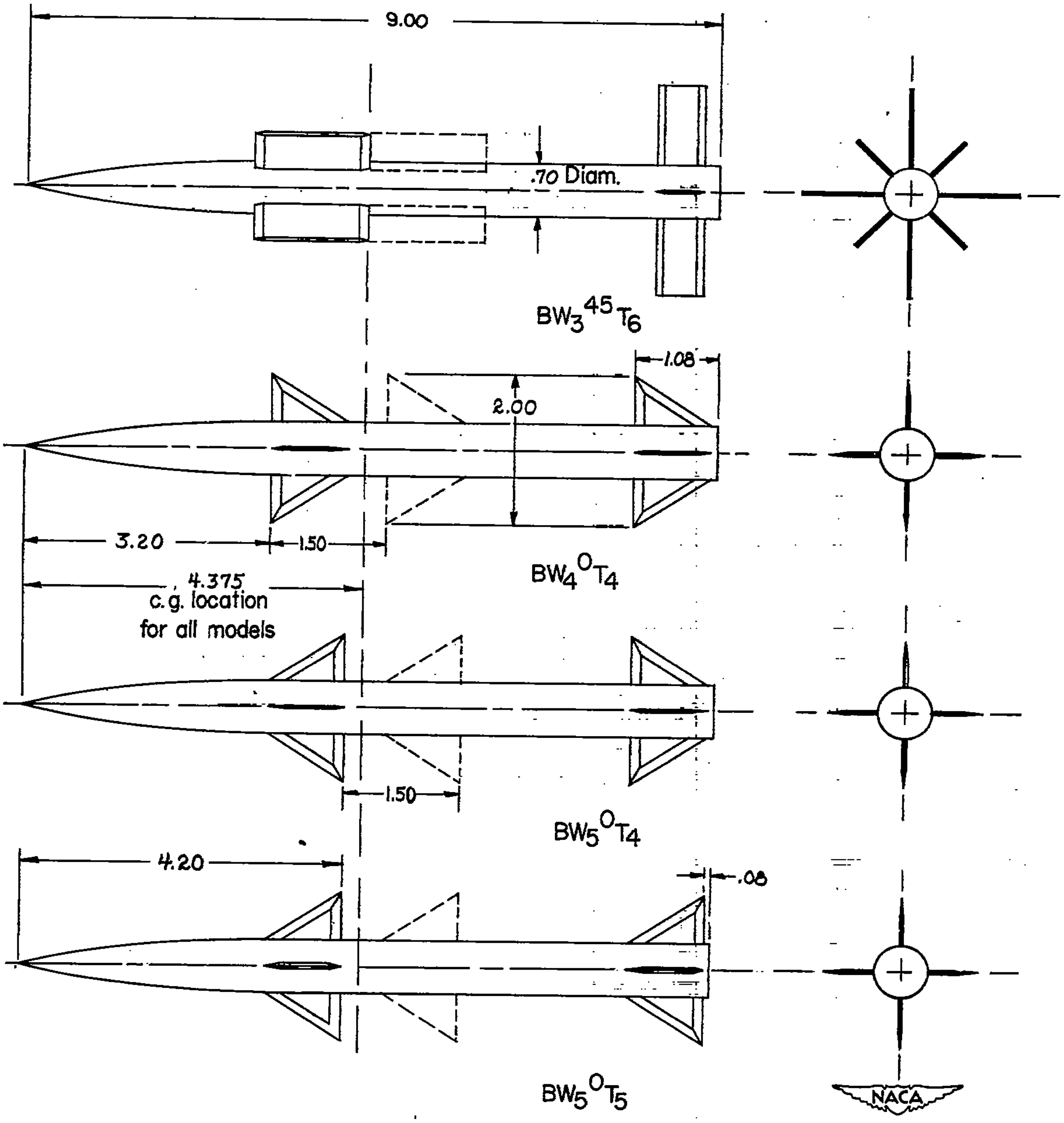

Figure 1.- Concluded.

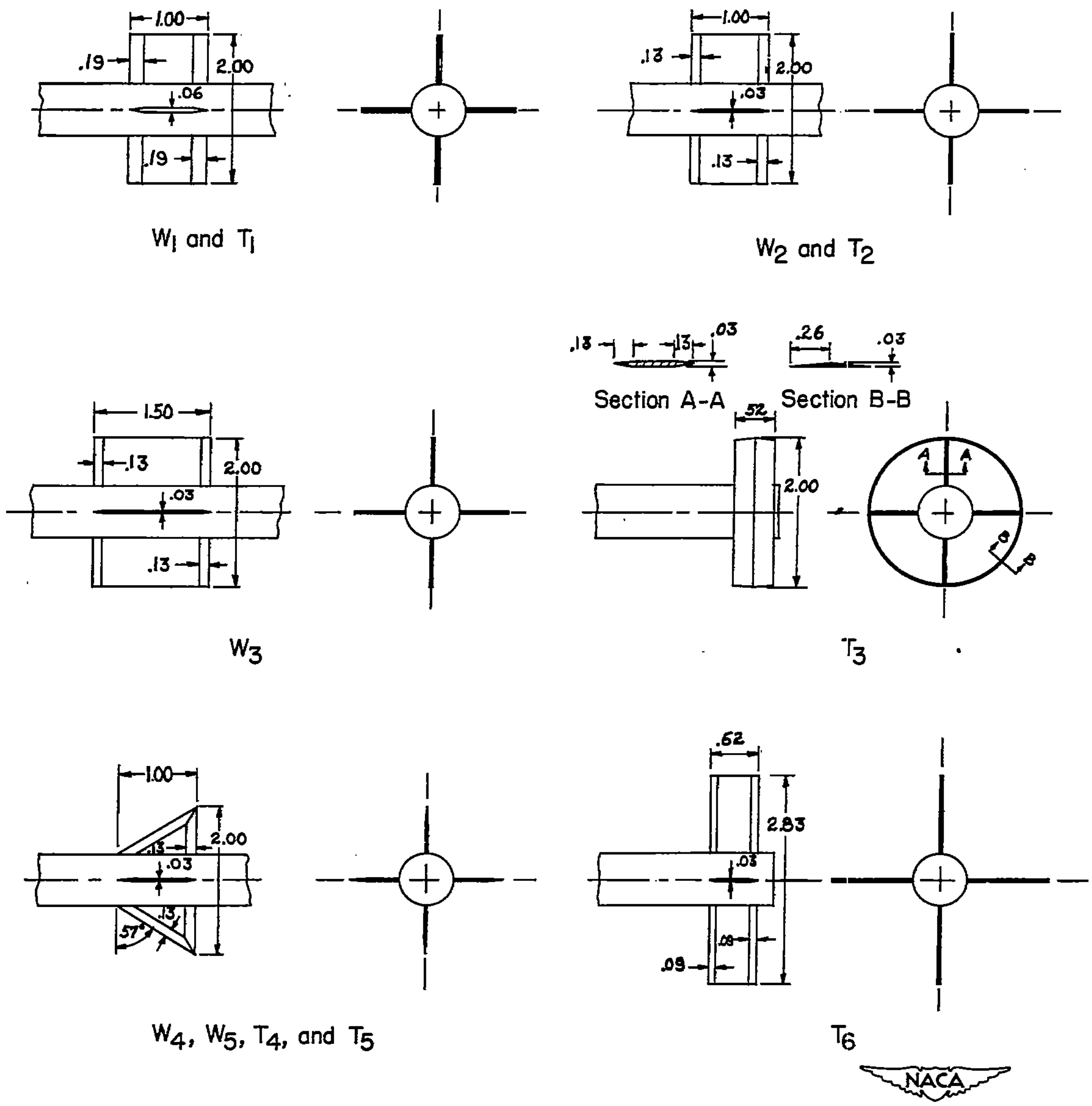

Figure 2.- Detail of wings and tails.

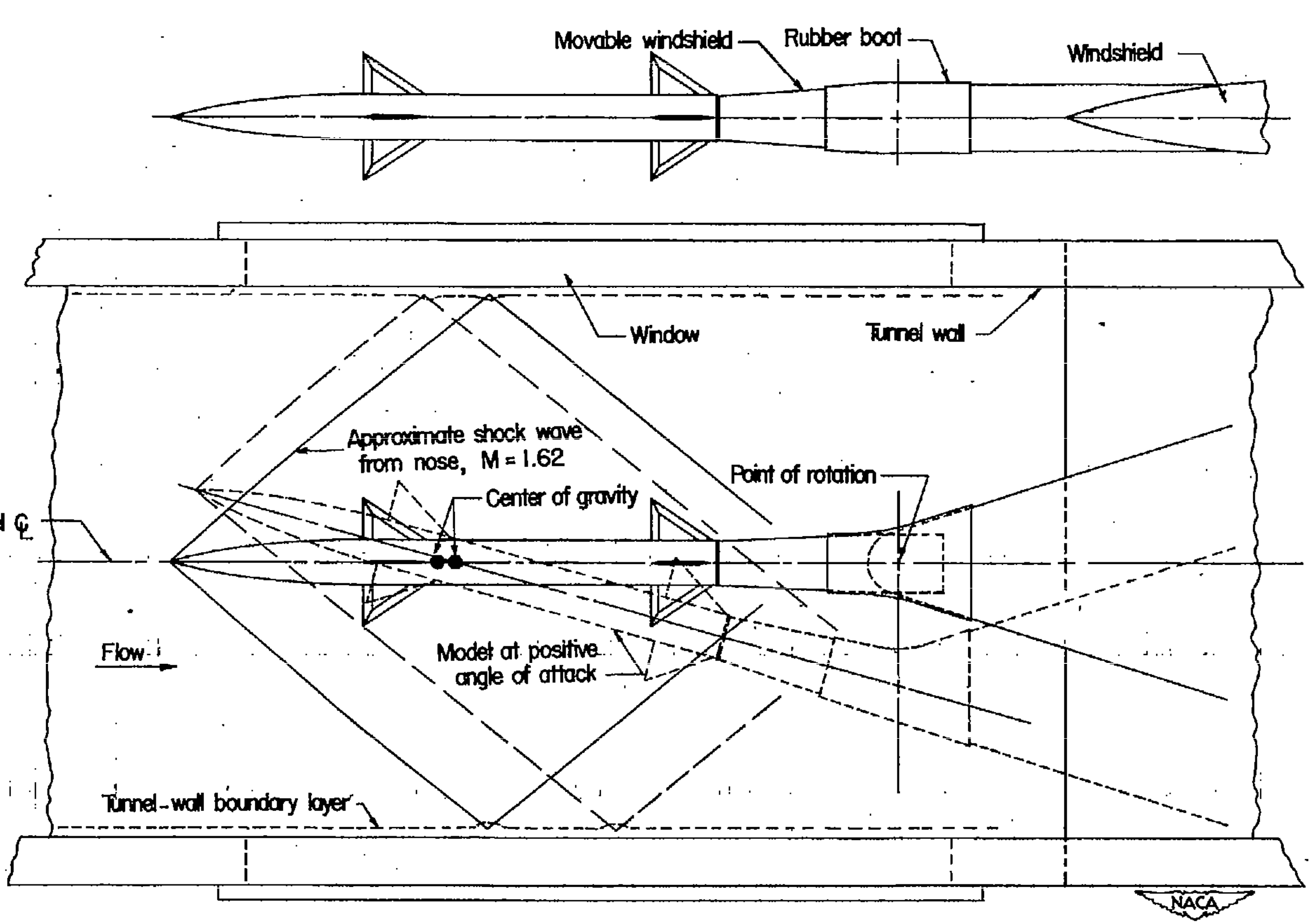

Figure 3.- Model installation in tunnel.

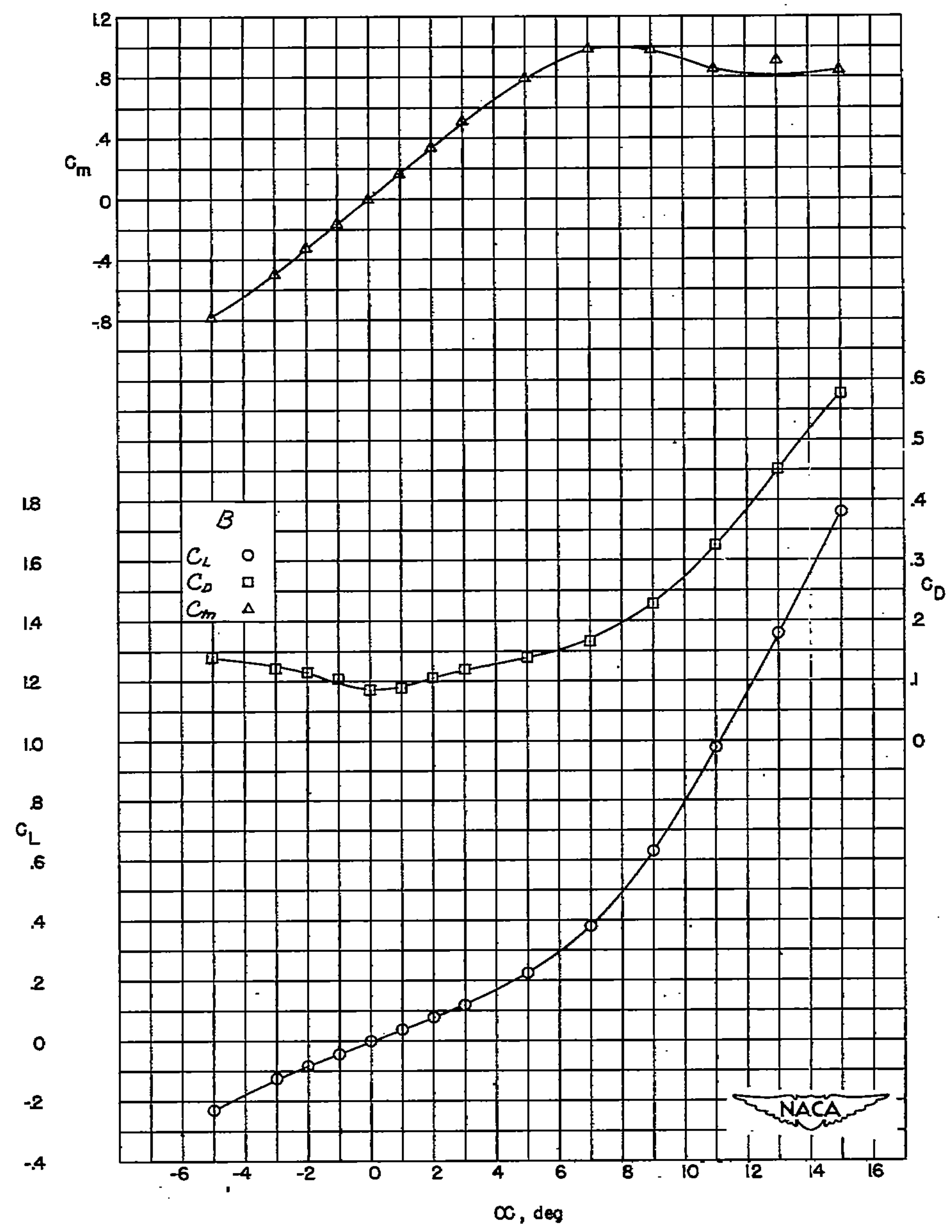

Figure 4.- Lift, drag, and pitching-moment characteristics of body alone.

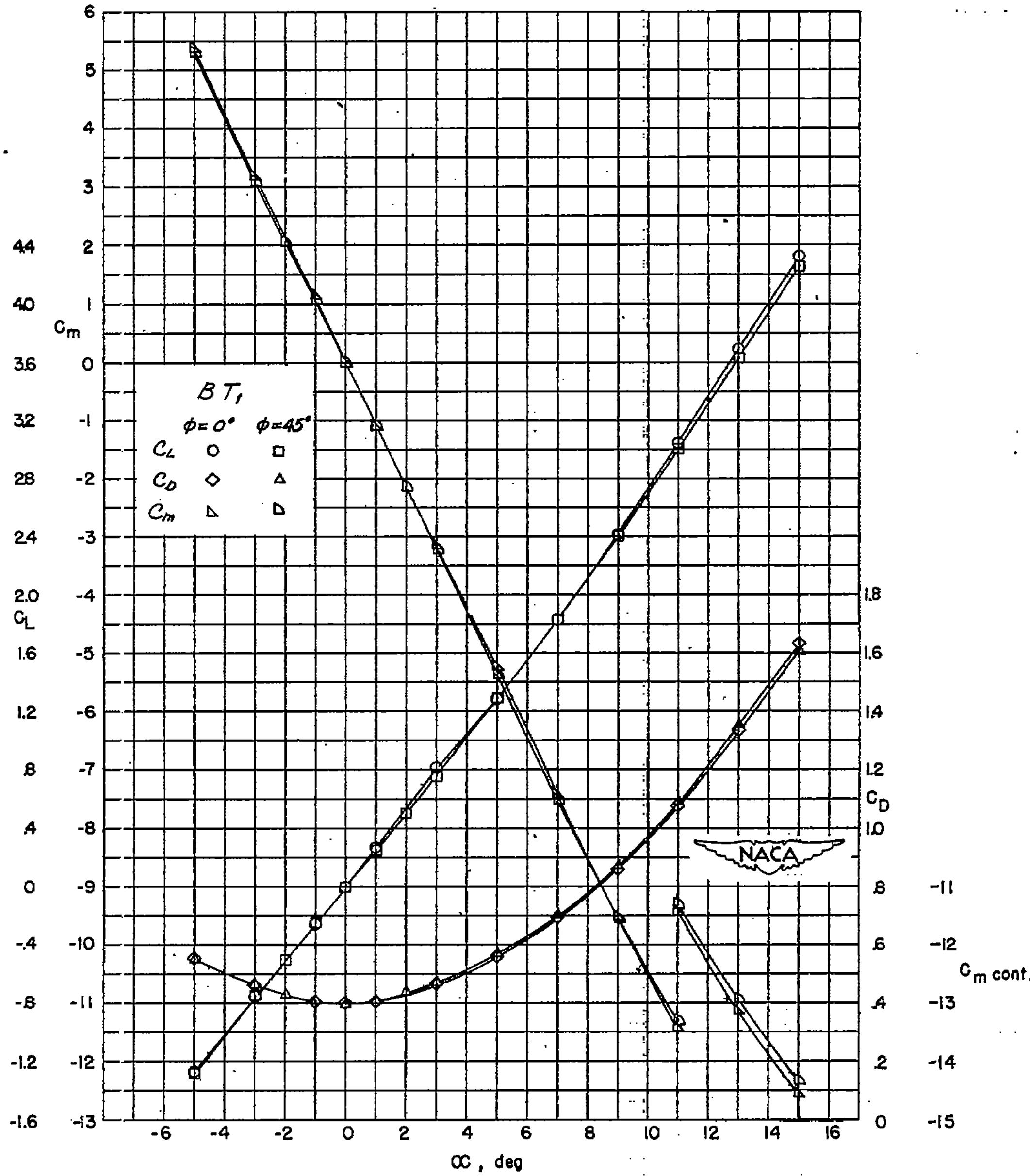

(a) BT_1.

Figure 5.- Lift, drag, and pitching-moment characteristics of model combinations of B and T.

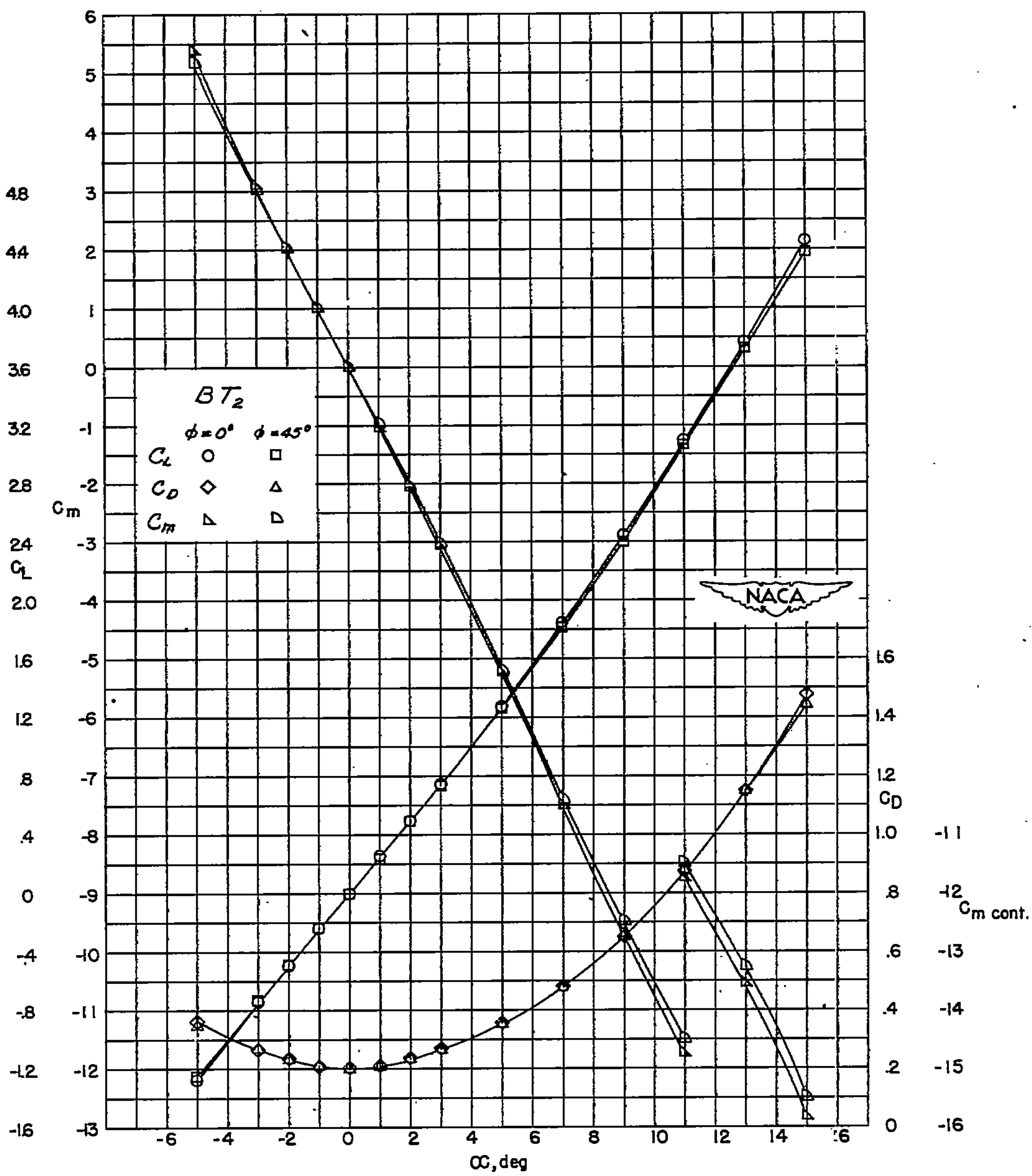

(b) BT_2.

Figure 5.- Continued.

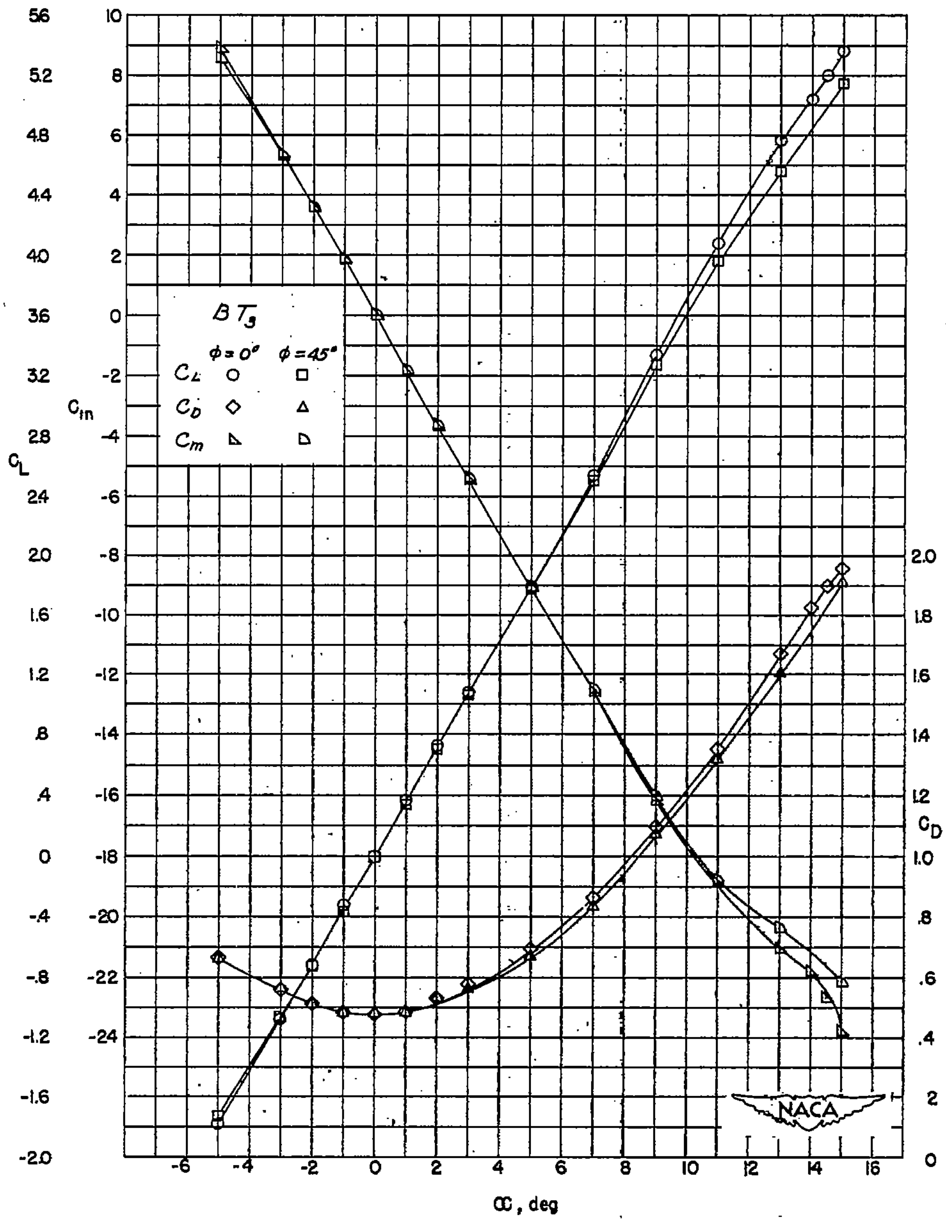

(c) BT_3.

Figure 5.- Continued.

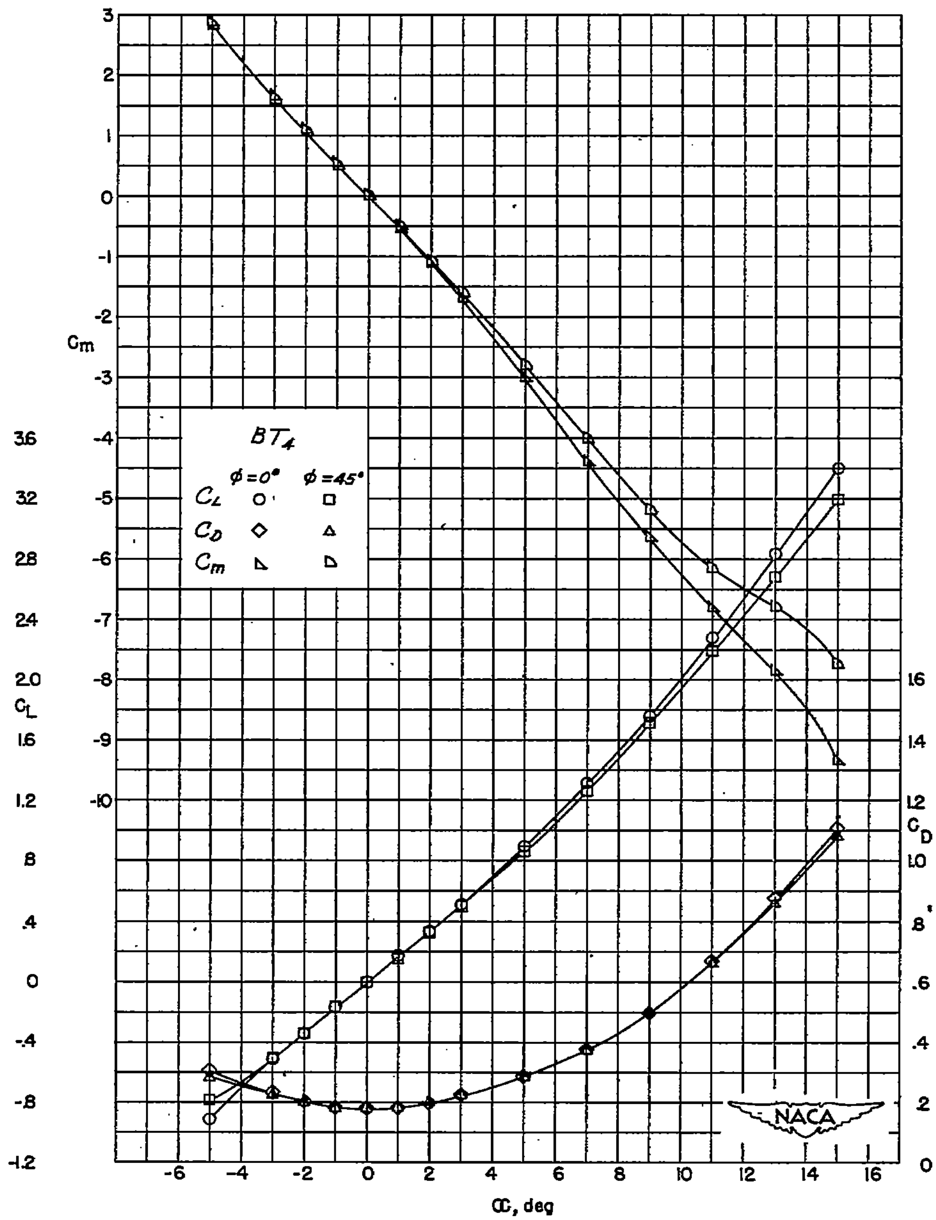

(d) BT_4.

Figure 5.- Continued.

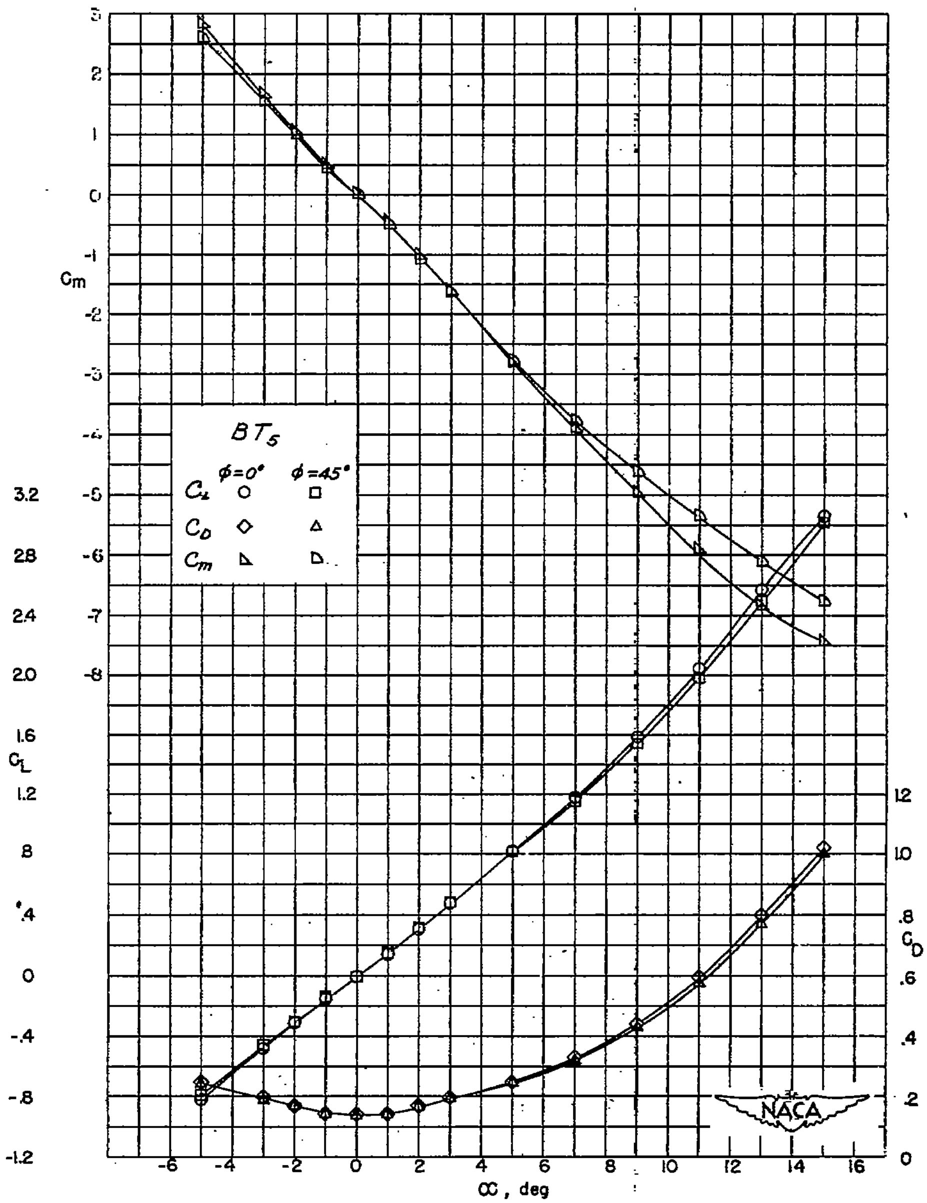

(e) BT_5.

Figure 5.- Continued.

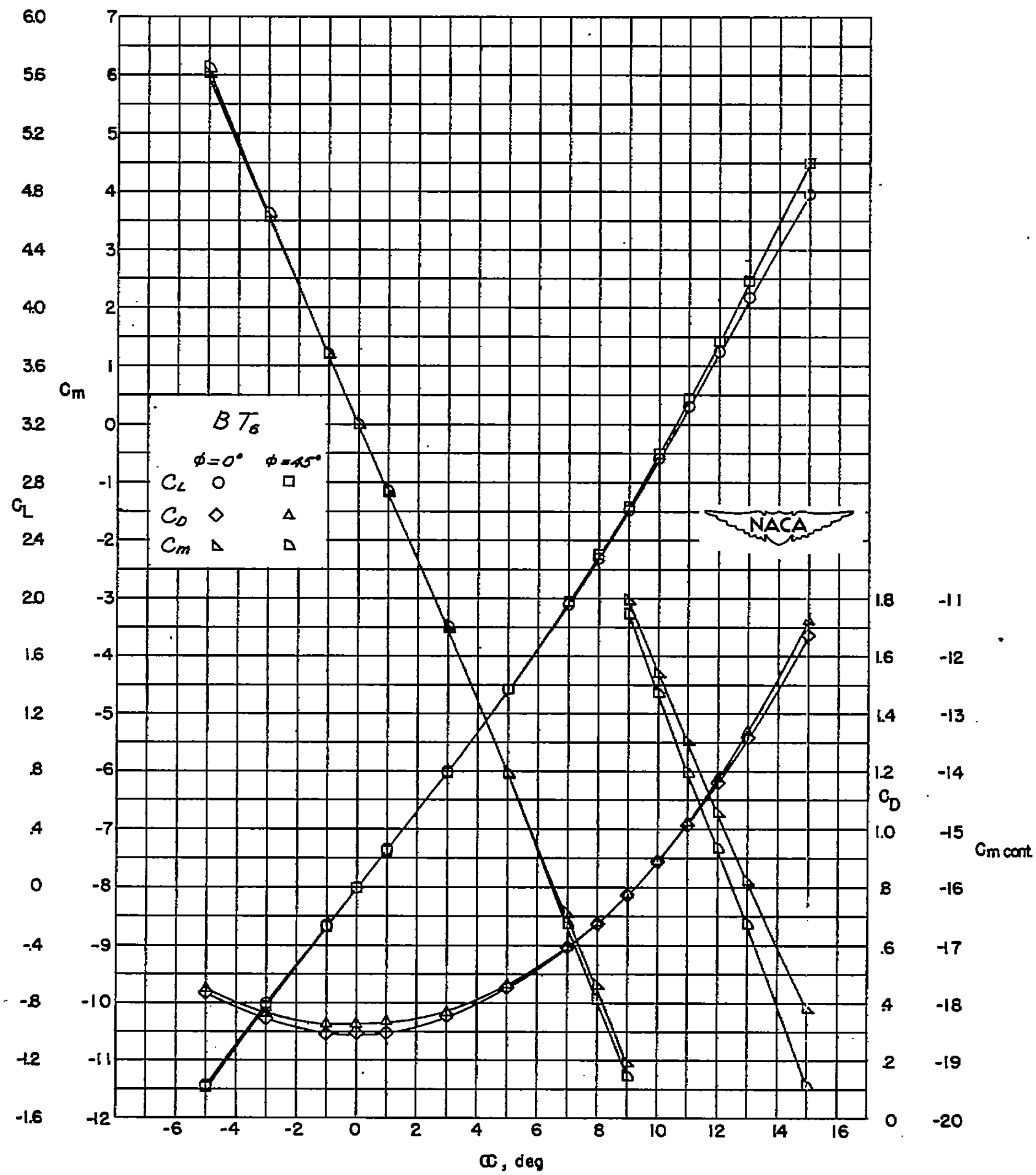

(f) BT_6.

Figure 5.- Concluded.

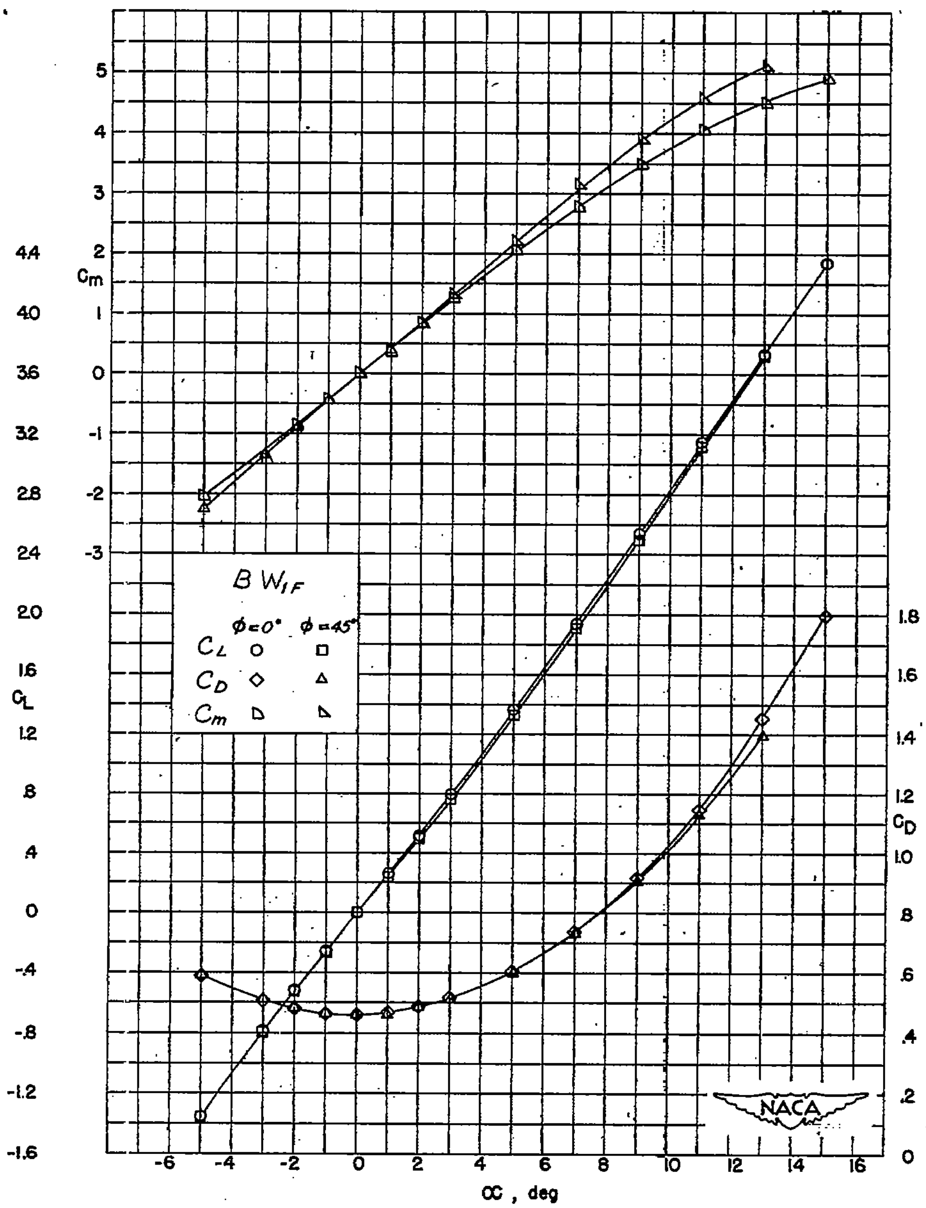

(a) BW_{1F}.

Figure 6.- Lift, drag, and pitching-moment characteristics of model combinations of B and W_1.

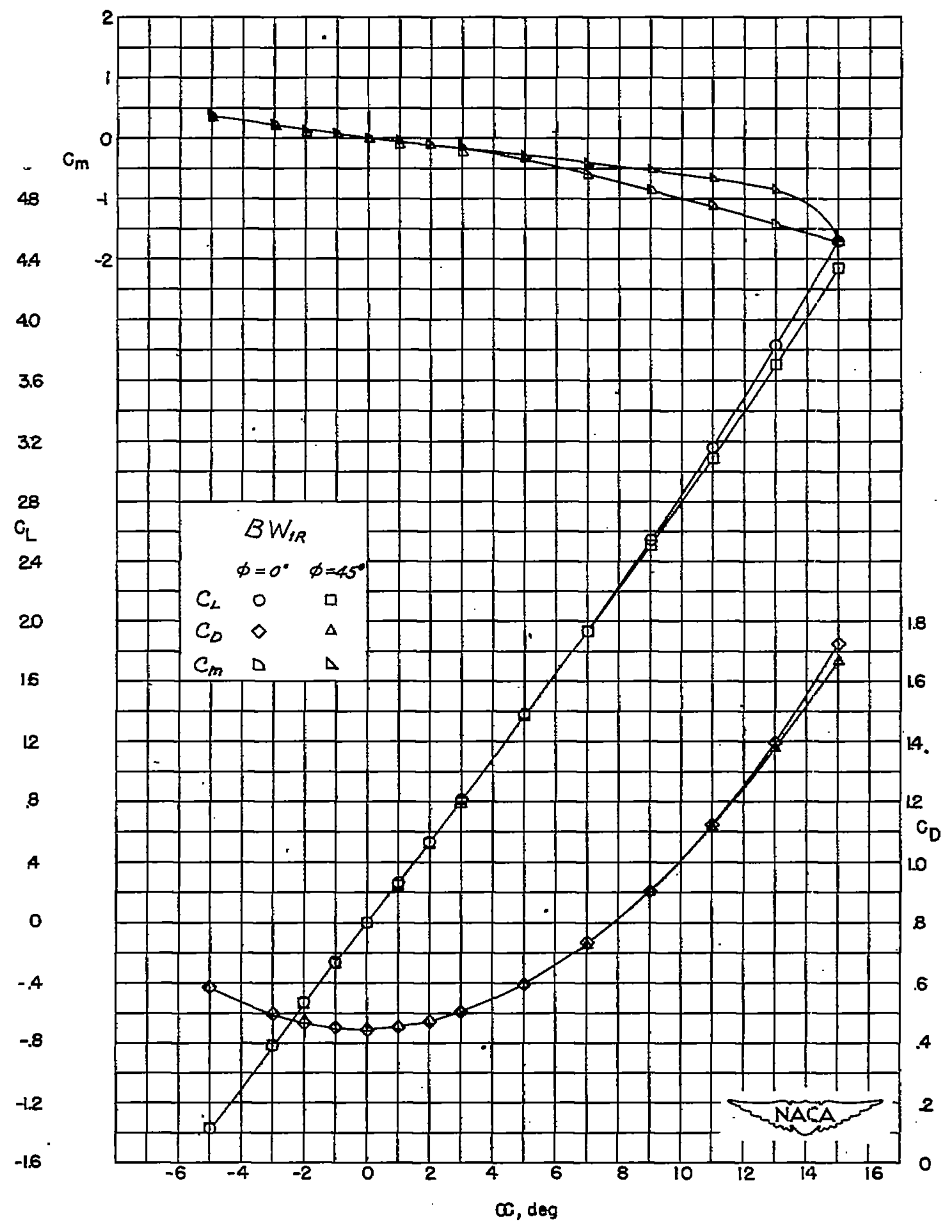

(b) BW_{1R}.

Figure 6.- Concluded.

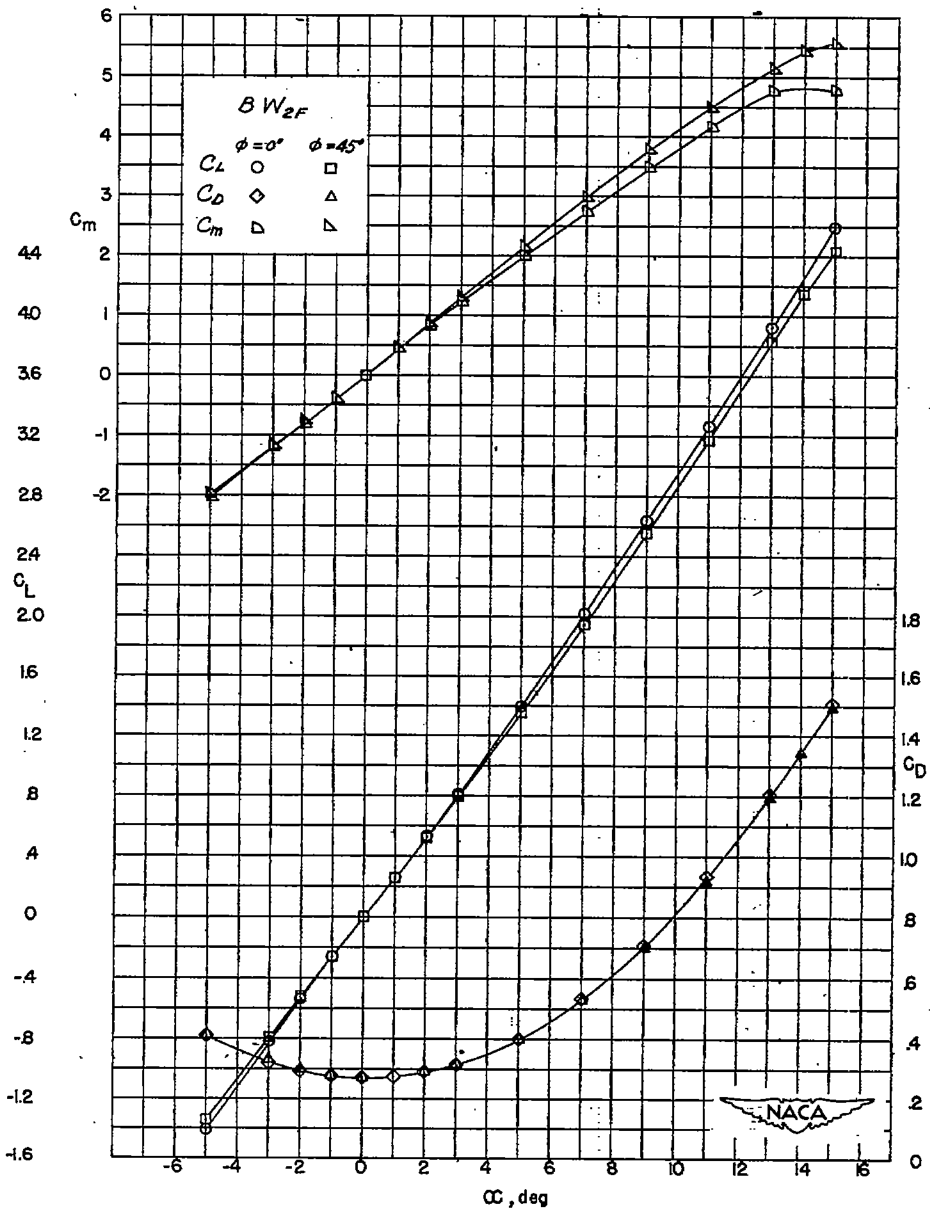

(a) BW_{2F}.

Figure 7.- Lift, drag, and pitching-moment characteristics of model combinations of B and W_2.

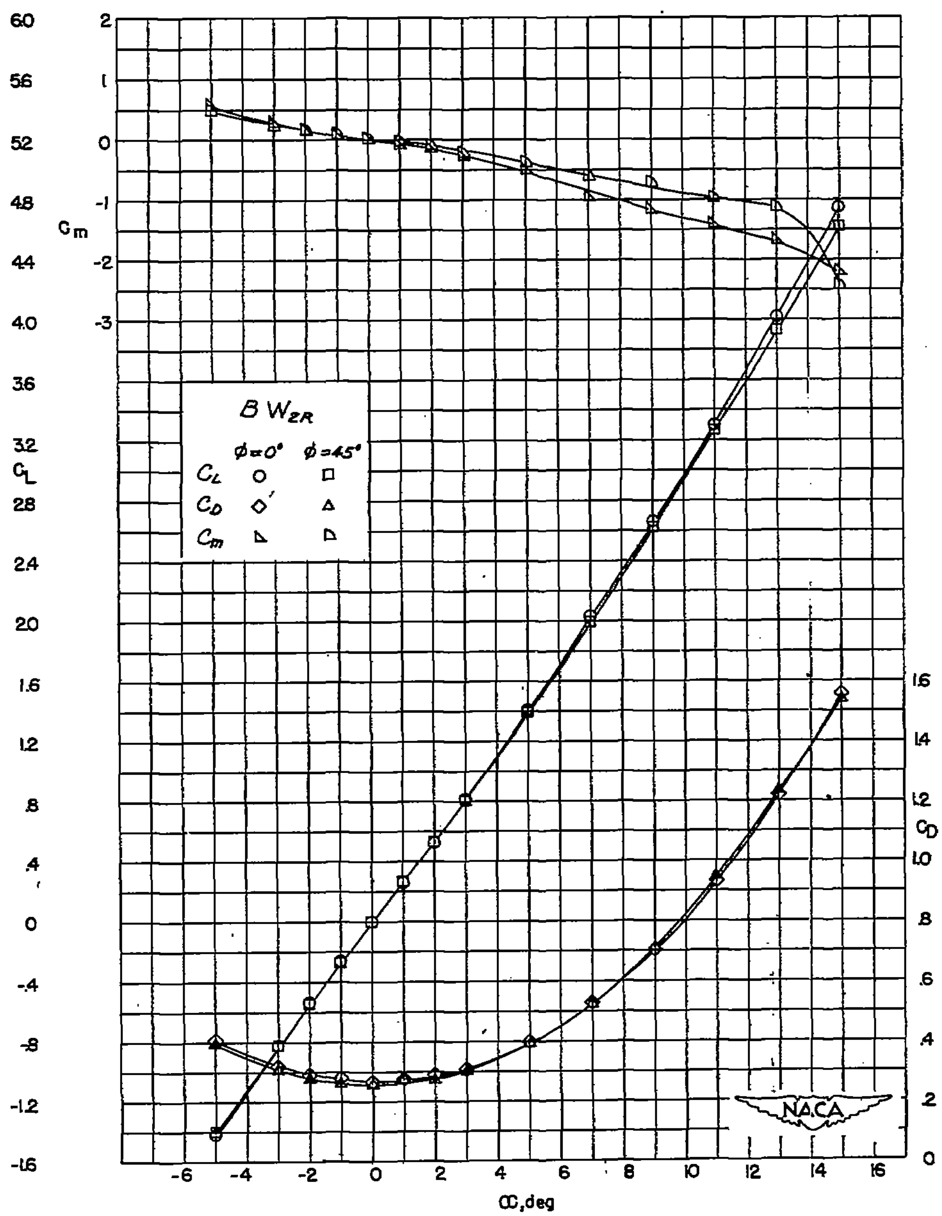

(b) BW_{2R}.

Figure 7.- Concluded.

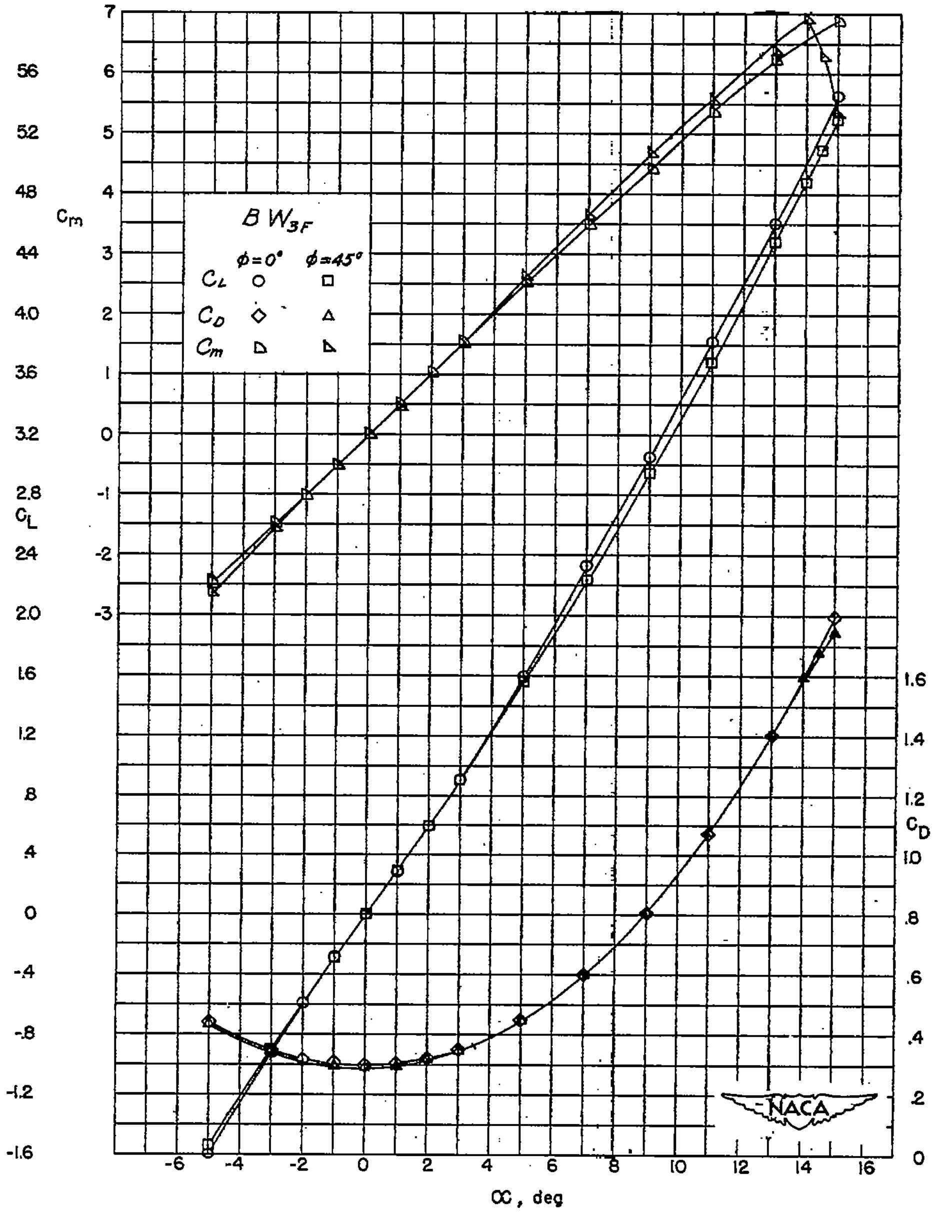

(a) BW_{3F}.

Figure 8.- Lift, drag, and pitching-moment characteristics of model combinations of B and W_3.

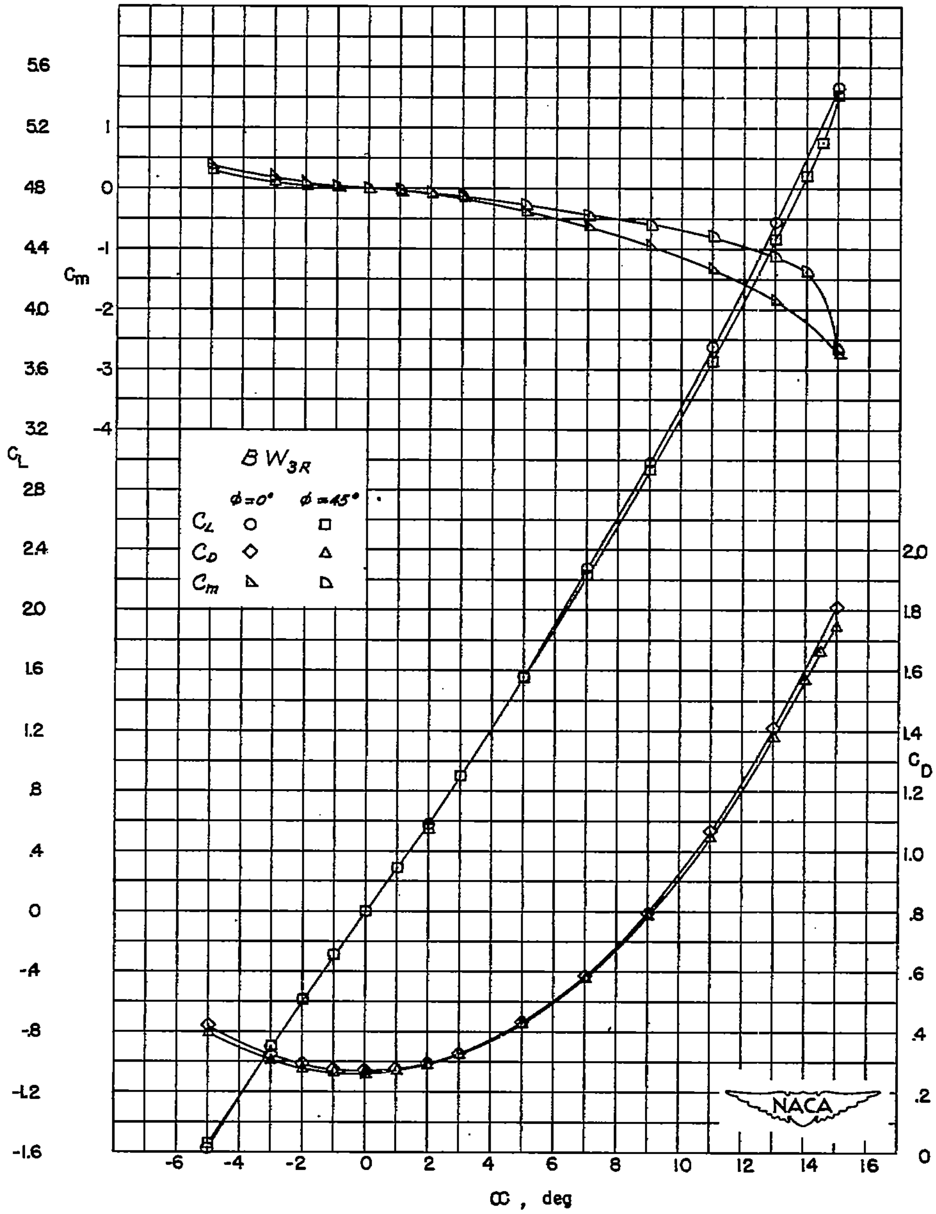

(b) BW_{3R}.

Figure 8.- Concluded.

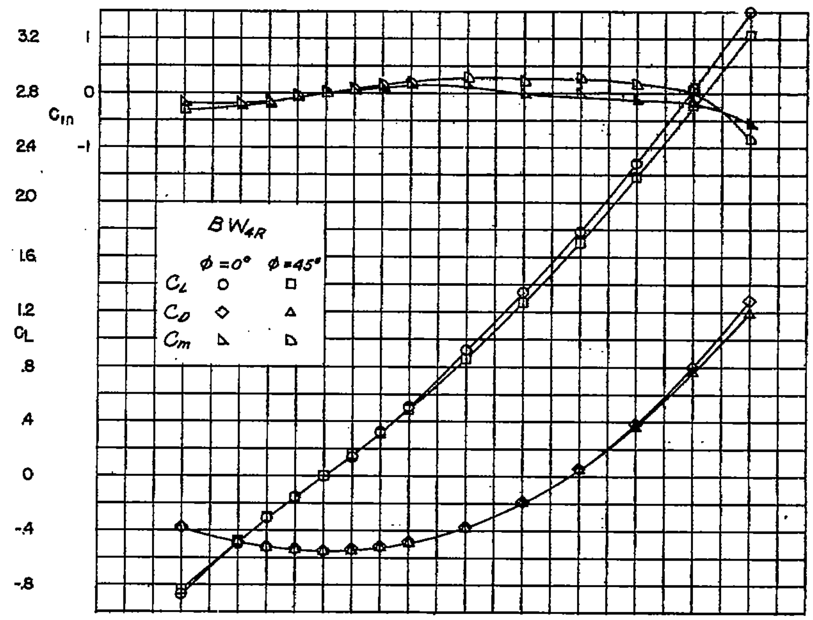

(a) BW_{4R}.

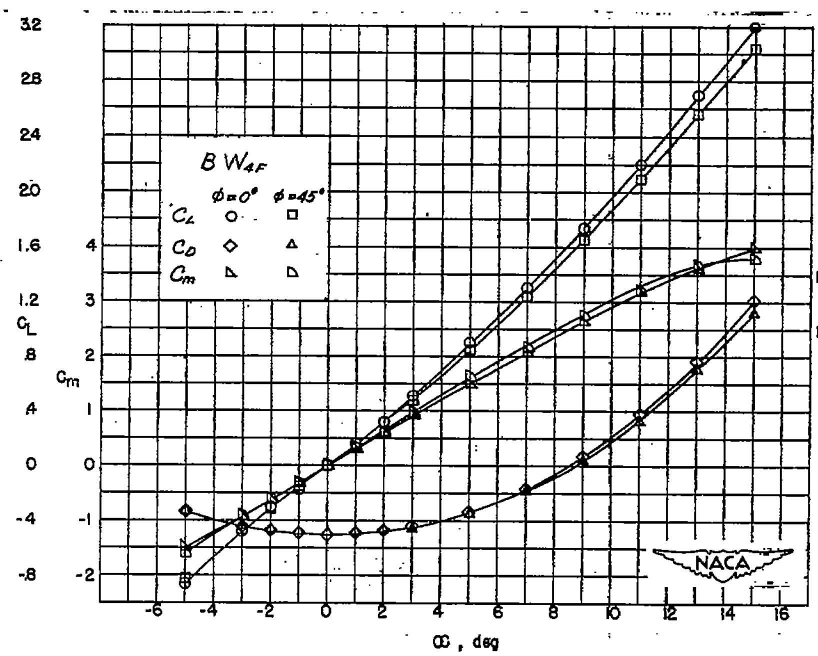

(b) BW_{4F}.

Figure 9.- Lift, drag, and pitching-moment characteristics of model combinations of B and W_4.

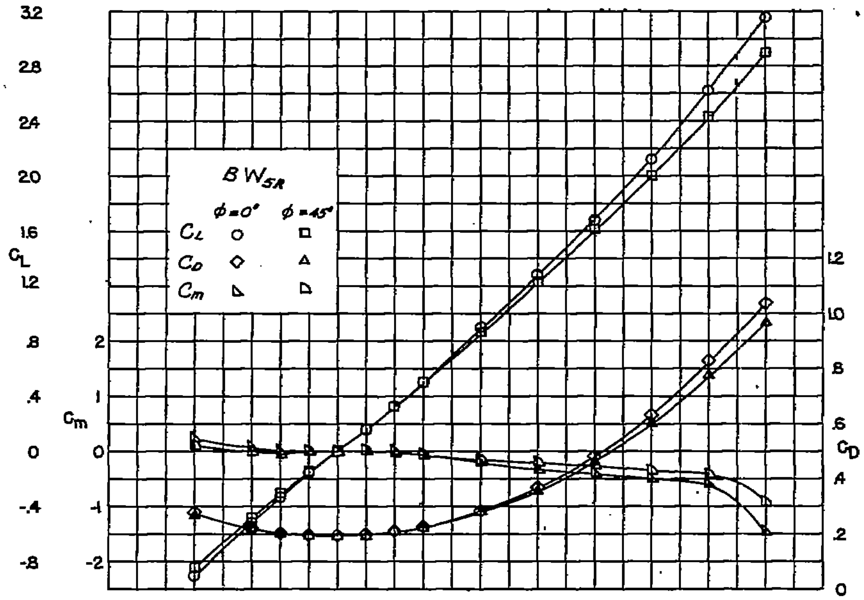

(a) BW_{5R}.

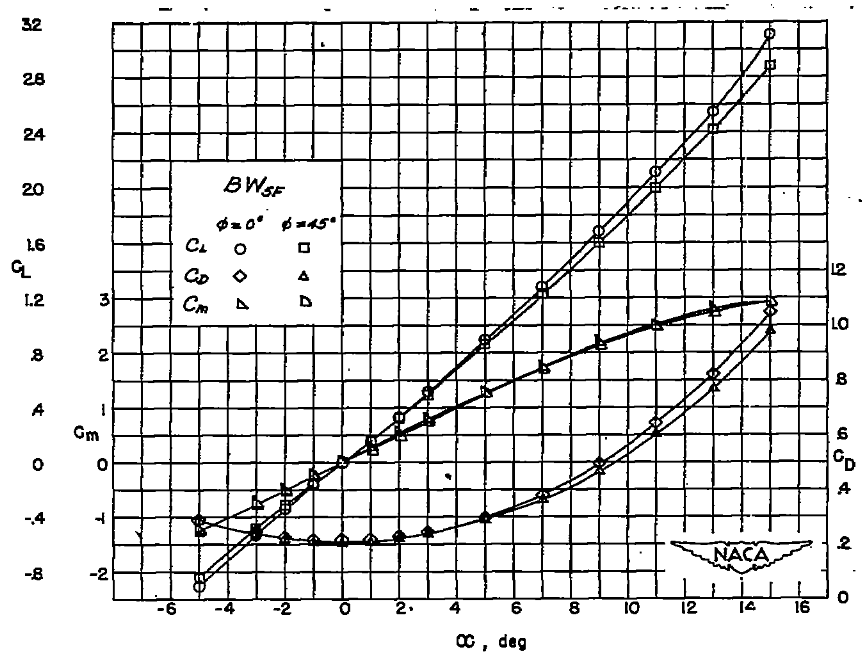

(b) BW_{5F}.

Figure 10.- Lift, drag, and pitching-moment characteristics of model combinations of B and W_5.

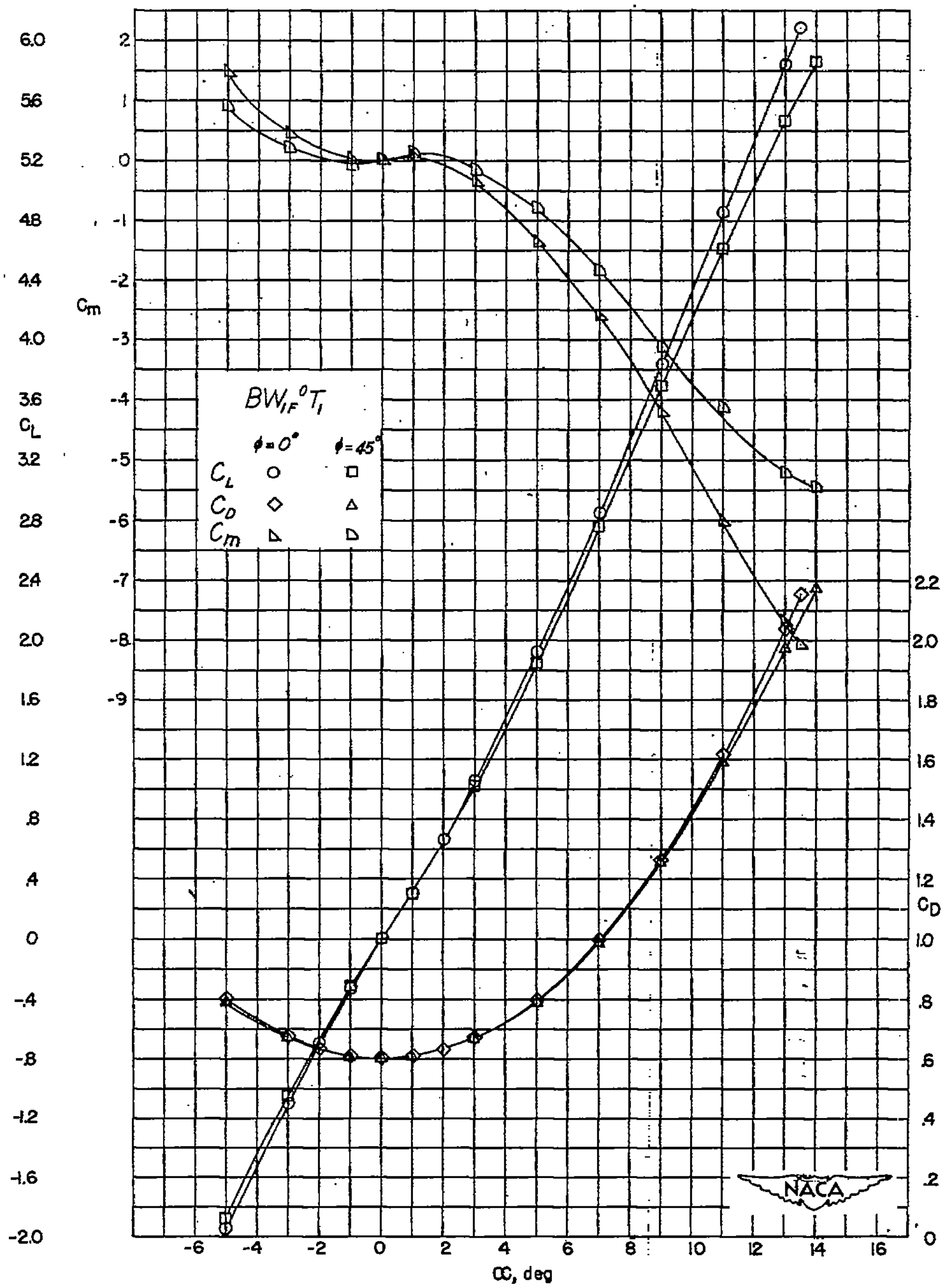

(a) $BW_{1F}{}^{0}T_{1}$.

Figure 11.- Lift, drag, and pitching-moment characteristics of model combinations of B, W_1, and T_1.

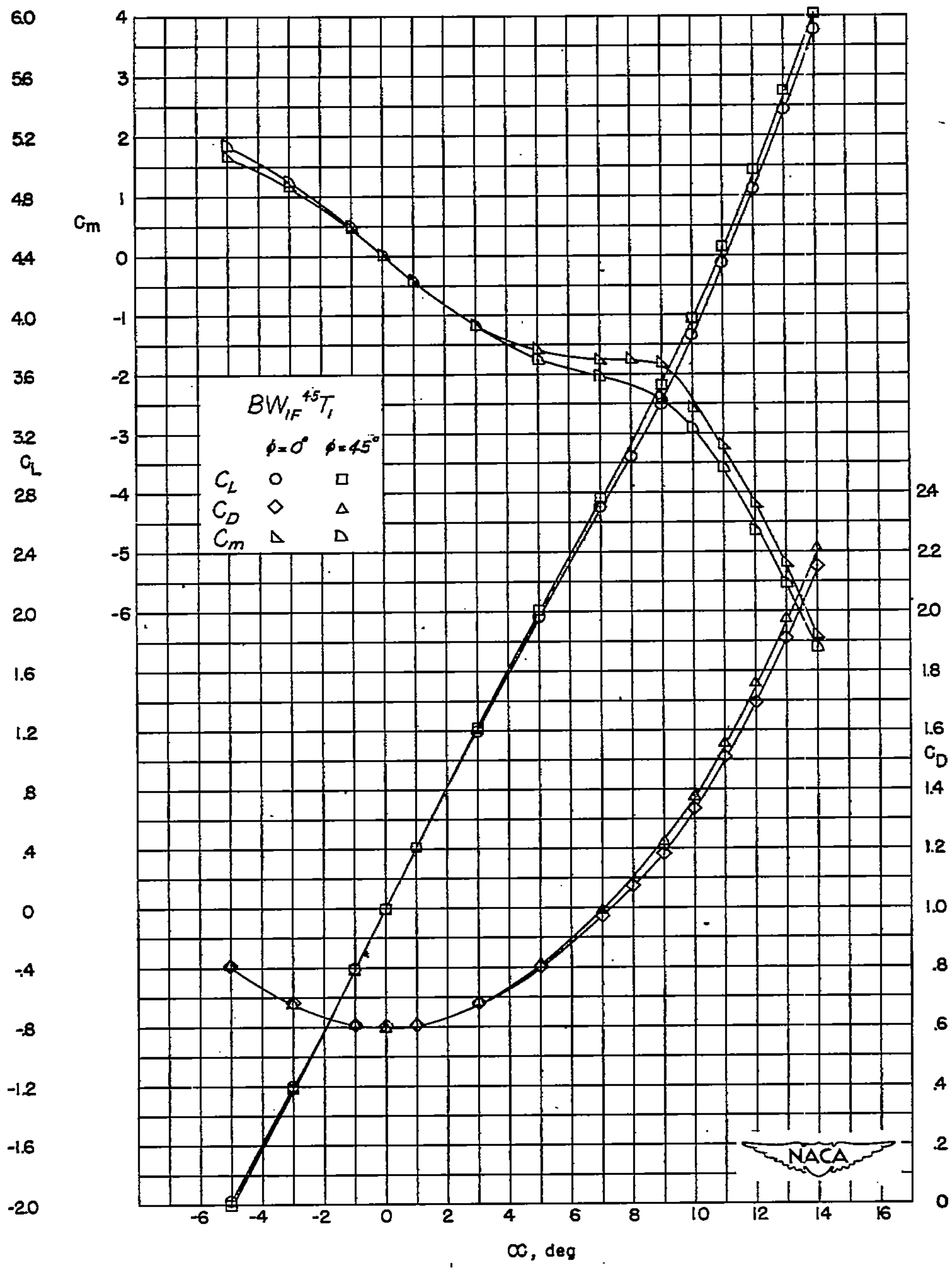

(b) $BW_{1F}^{45}T_1$.

Figure 11.- Continued.

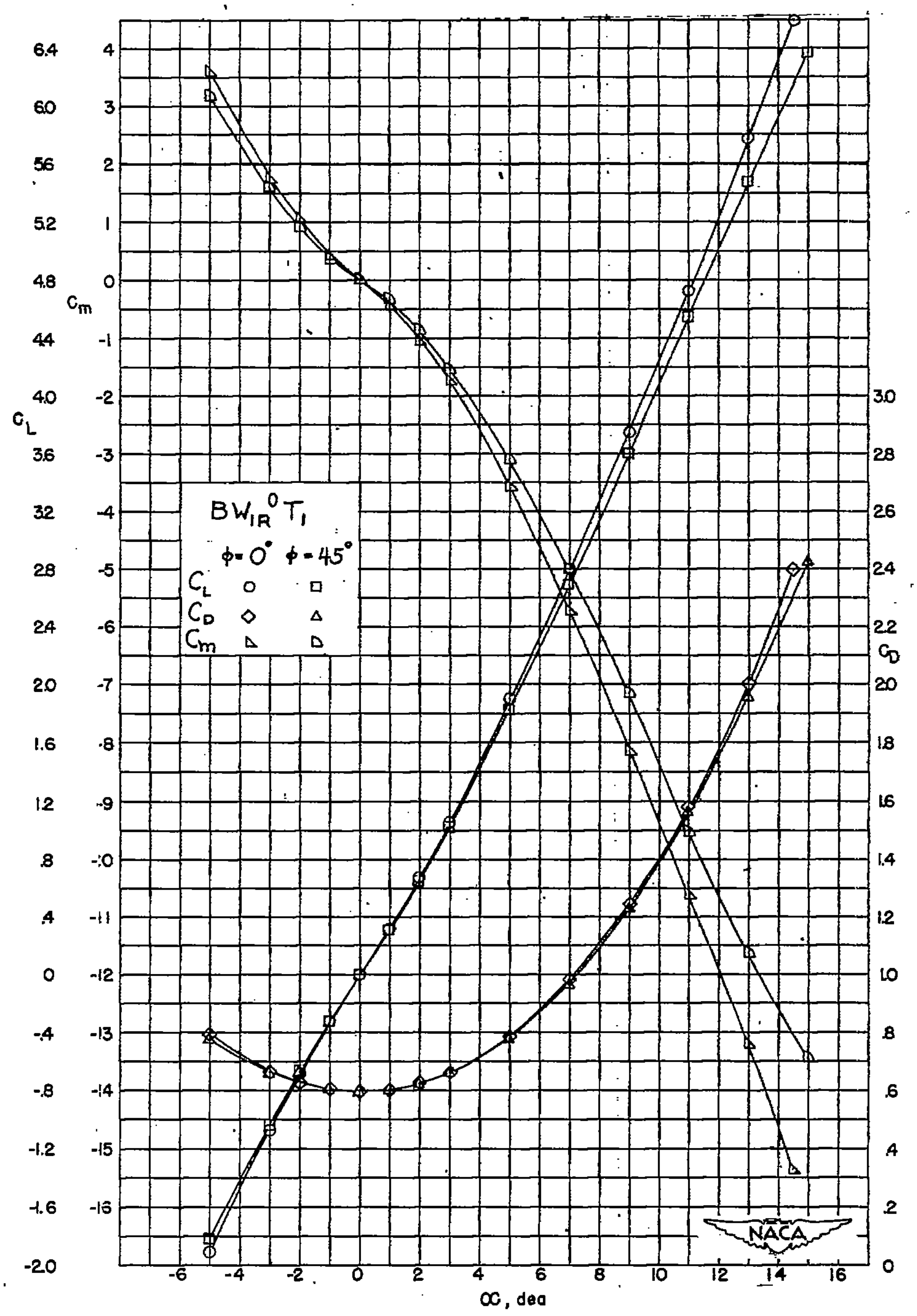

(c) $BW_{1R}{}^{0}T_{1}$.

Figure 11.- Continued.

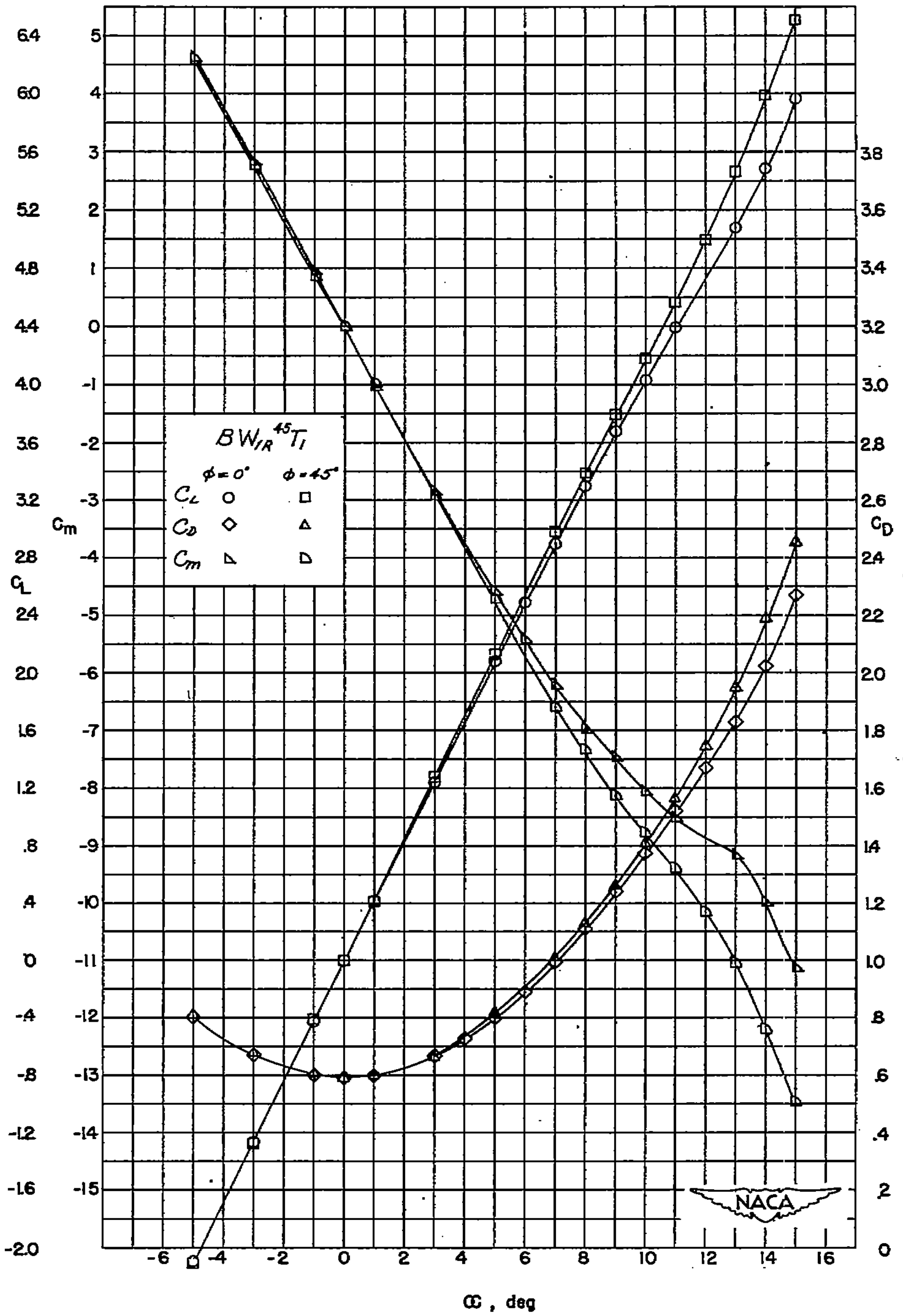

(d) $BW_{1R}^{45}T_1$.

Figure 11.- Concluded.

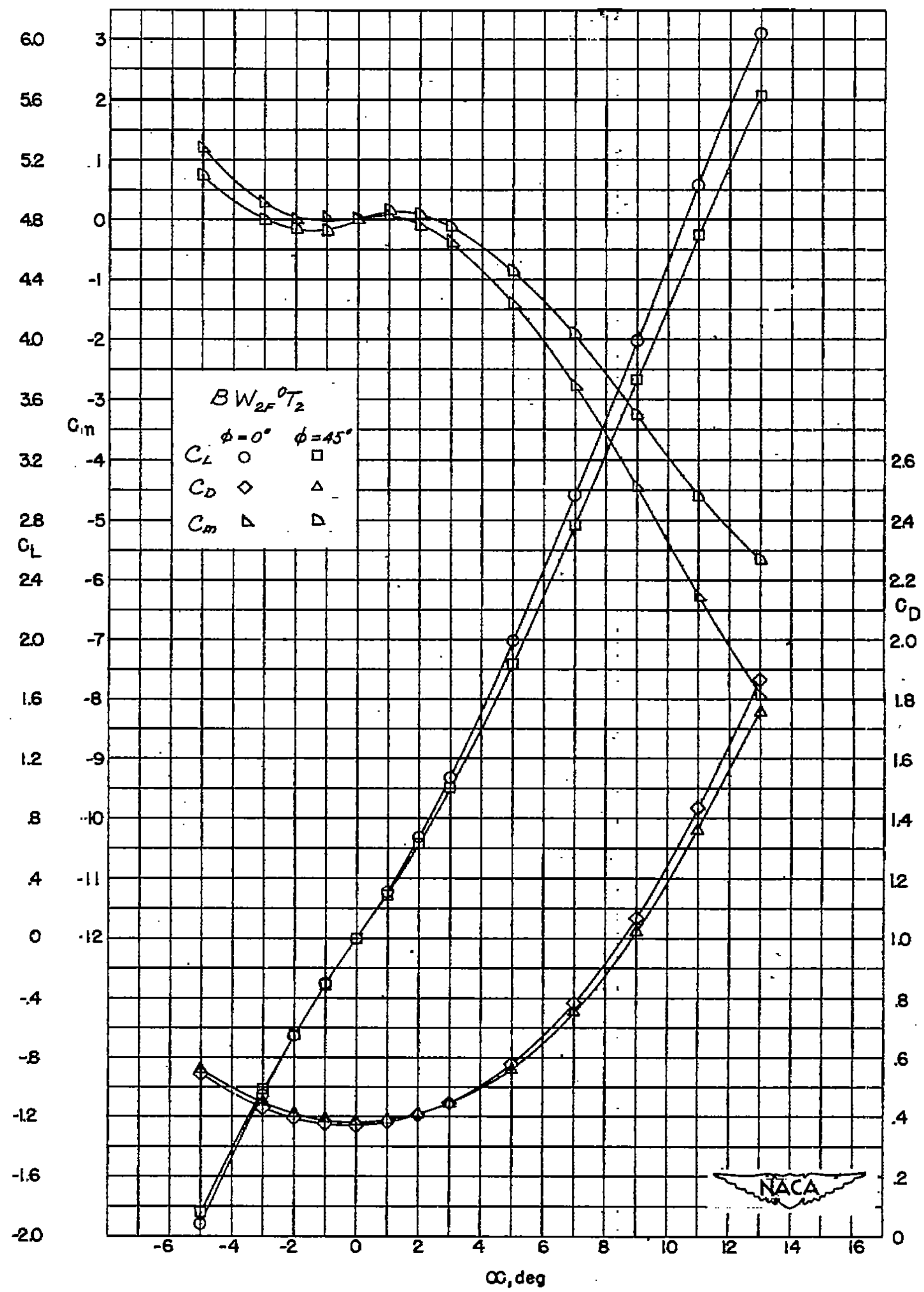

(a) $BW_{2F}{}^{0}T_2$.

Figure 12.- Lift, drag, and pitching-moment characteristics of model combinations of B, W_2, and T_2.

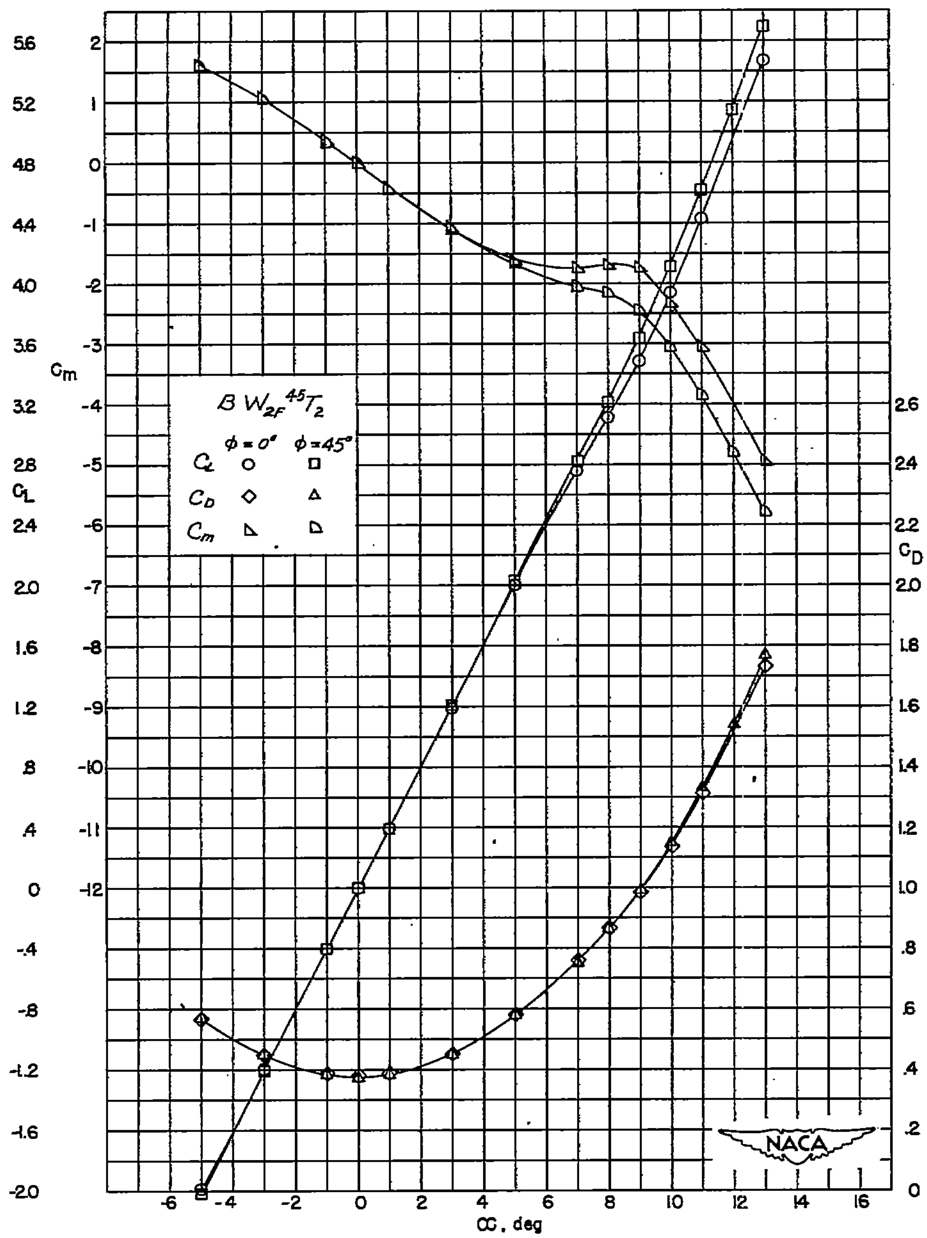

(b) $BW_{2F}{}^{45}T_2$.

Figure 12.- Continued.

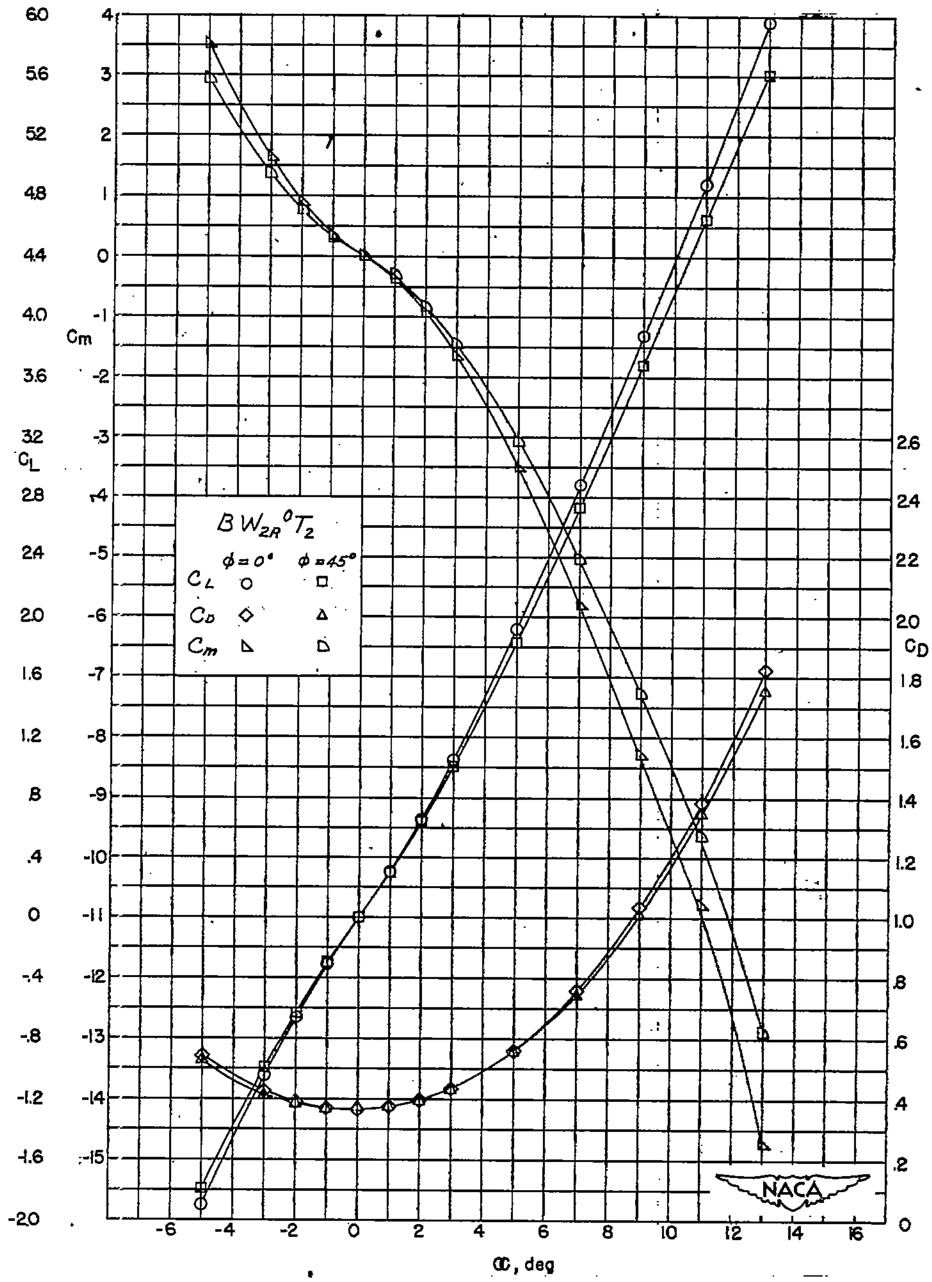

(c) $BW_{2R}{}^{0}T_2$.

Figure 12.- Continued.

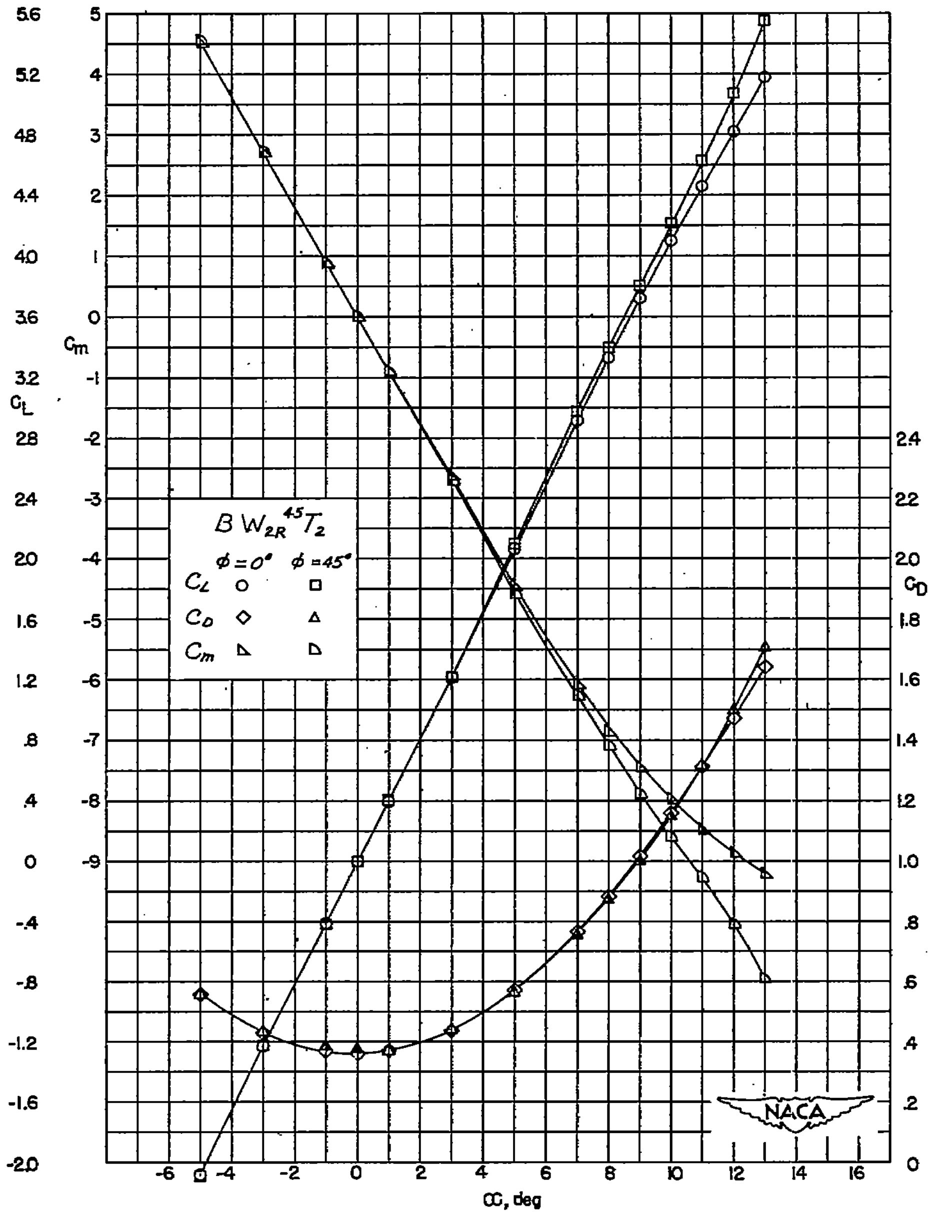

(d) $BW_{2R}{}^{45}T_2$.

Figure 12.- Concluded.

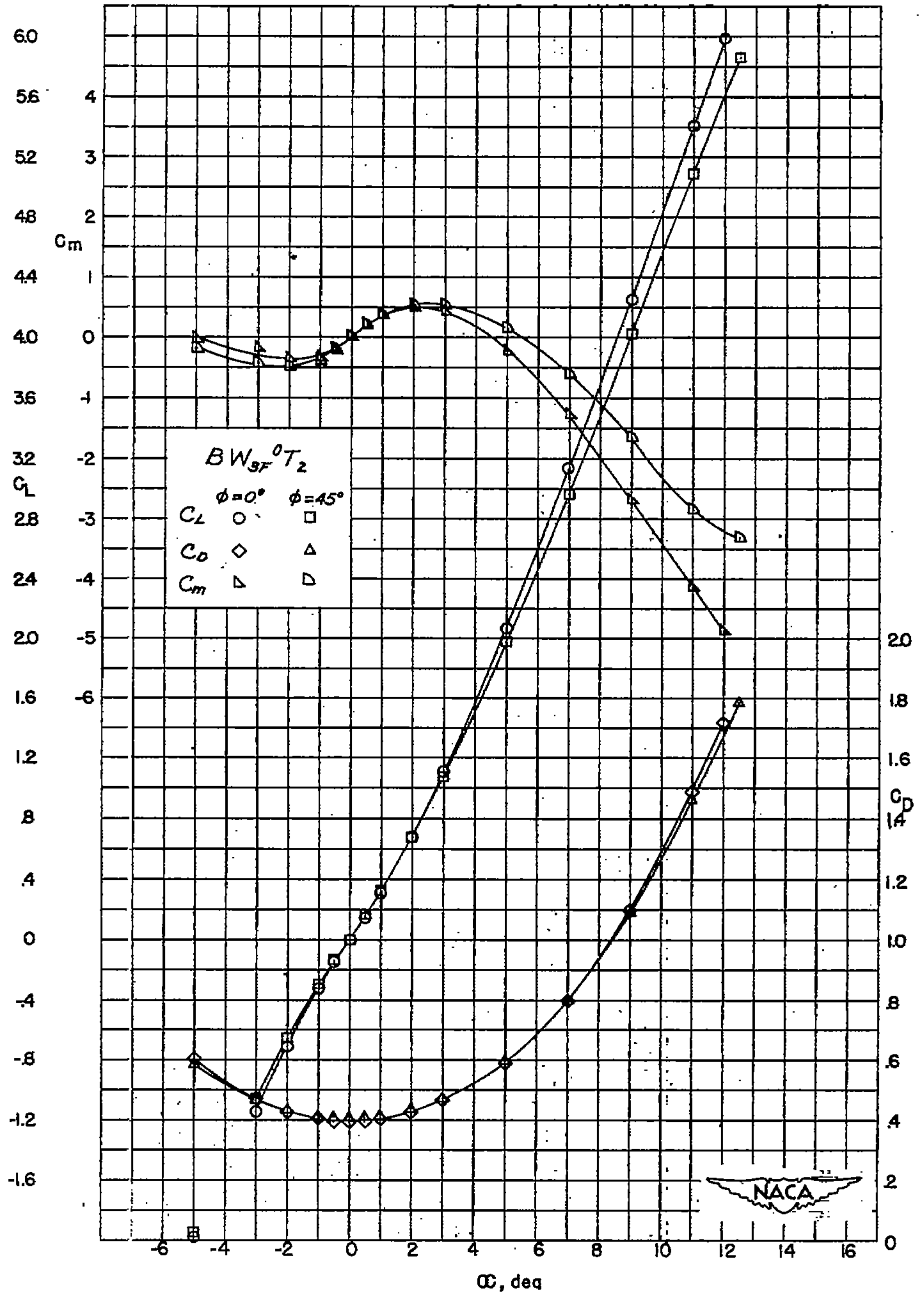

(a) $BW_{3F}{}^{0}T_2$.

Figure 13.- Lift, drag, and pitching-moment characteristics of model combinations of B, W_3, and T_2.

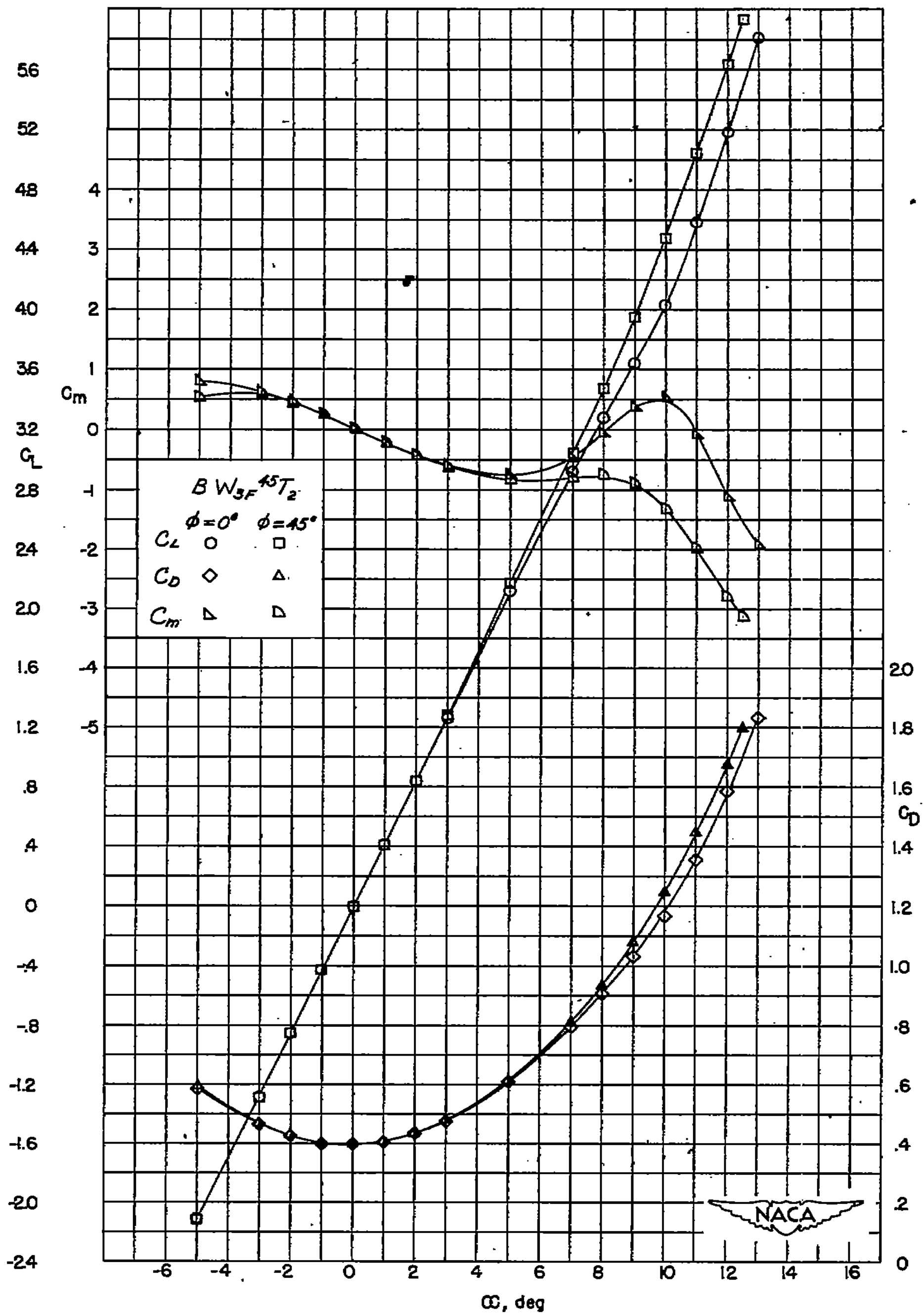

(b) $BW_{3F}^{45}T_2$.

Figure 13.- Continued.

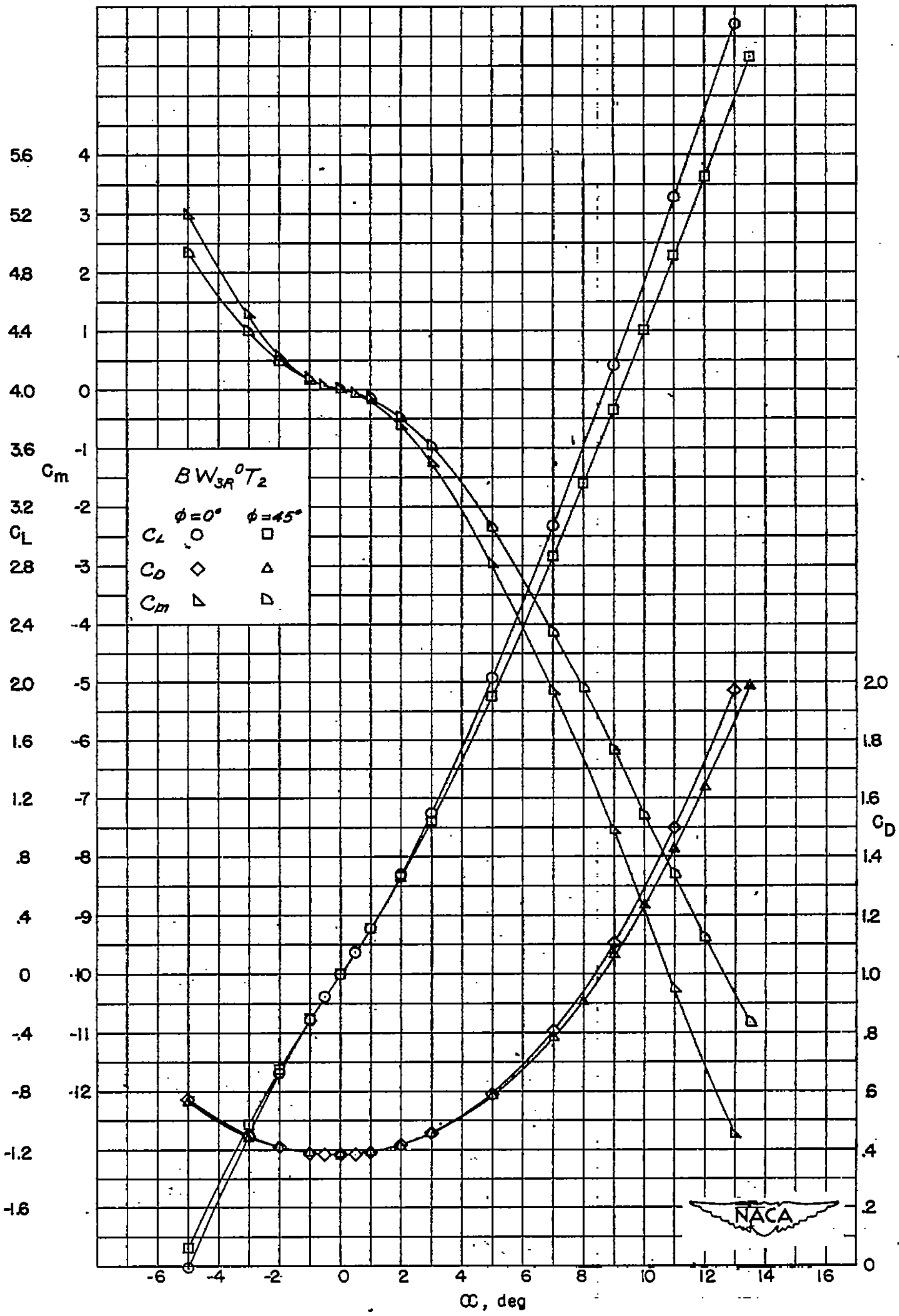

(c) $BW_{3R}{}^{0}T_2$.

Figure 13.- Continued.

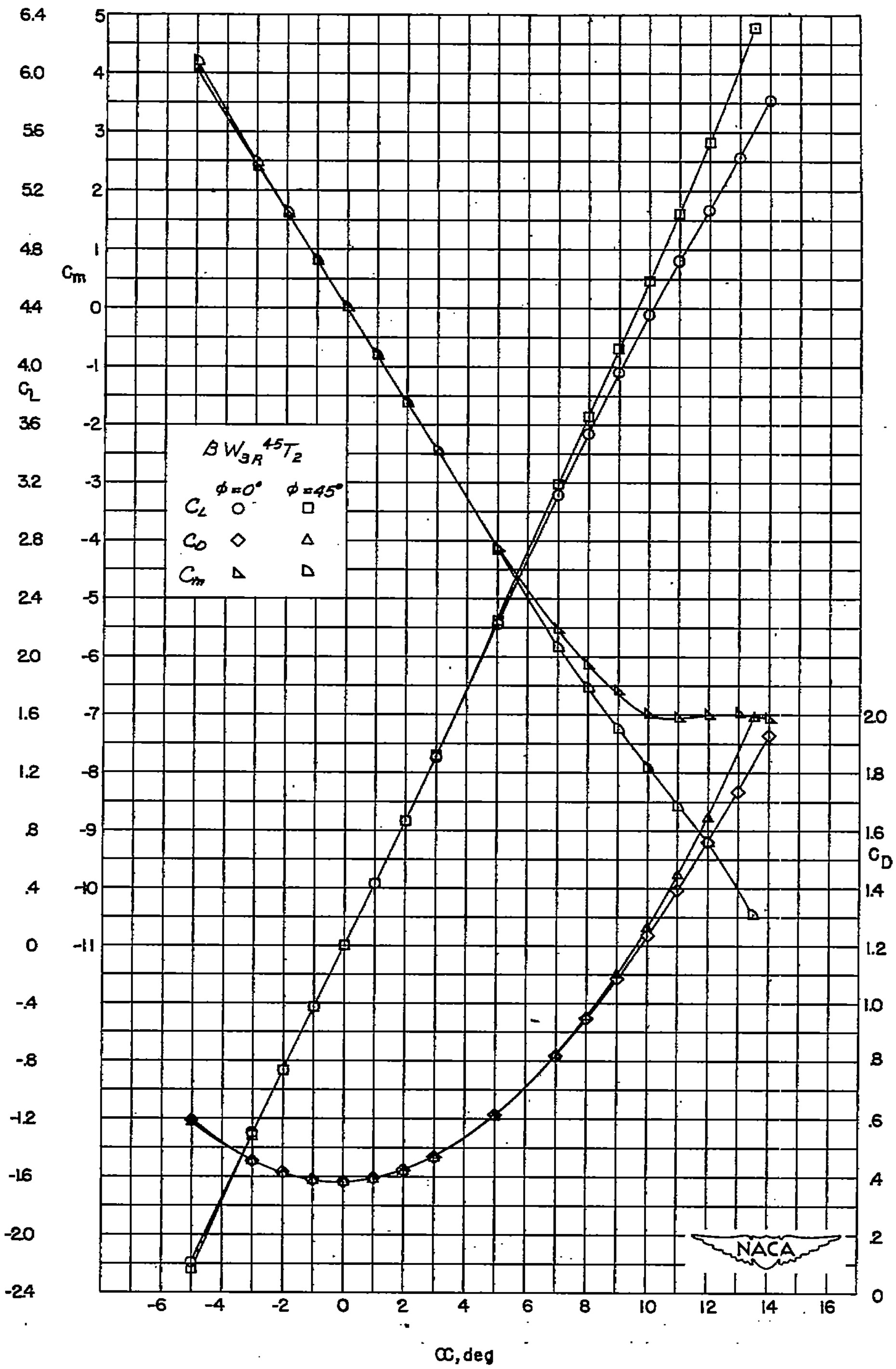

(d) $BW_{3R}{}^{45}T_2$.

Figure 13.- Concluded.

[redacted]

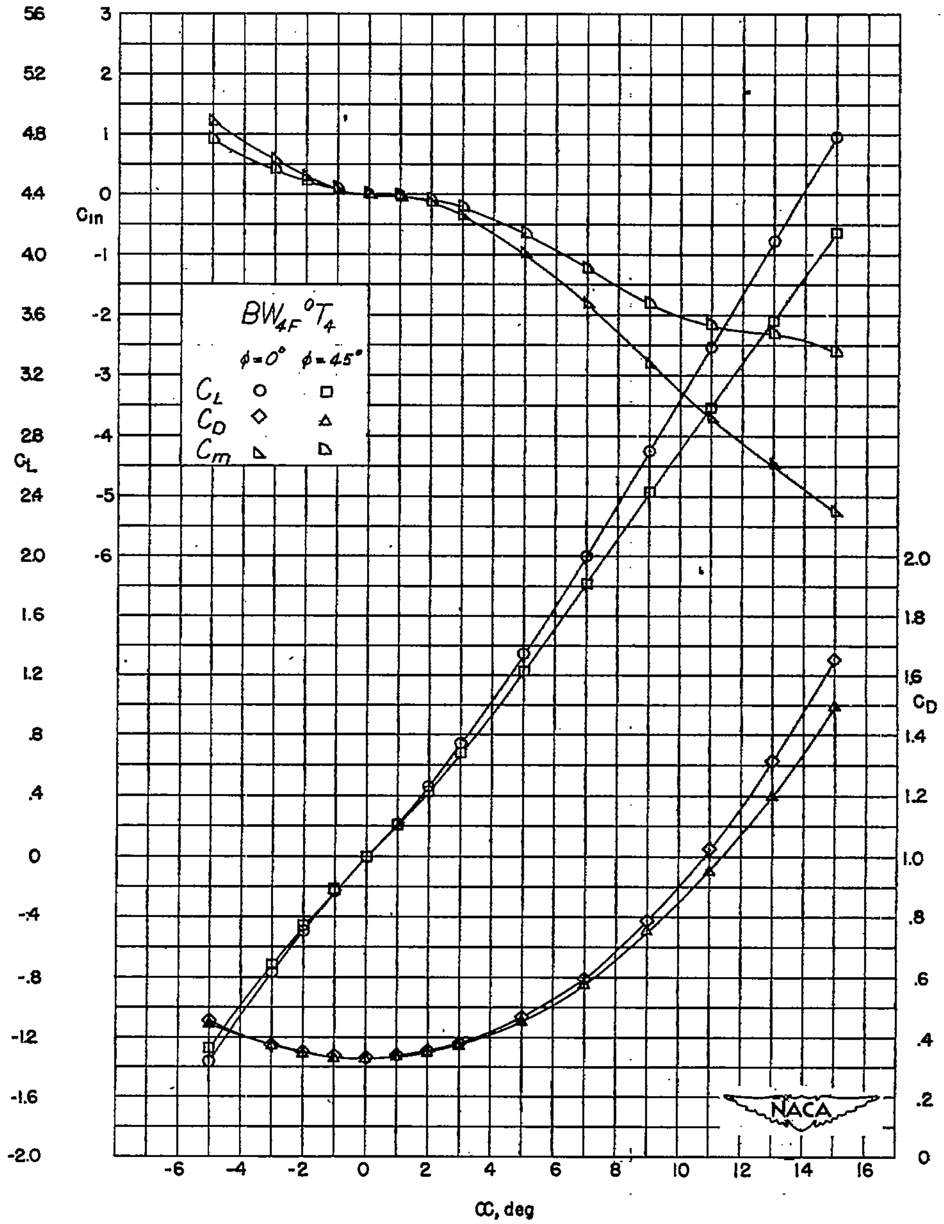

(a) $BW_{4F}{}^{0}T_4$.

Figure 14.- Lift, drag, and pitching-moment characteristics of model combinations of B, W_4, and T_4.

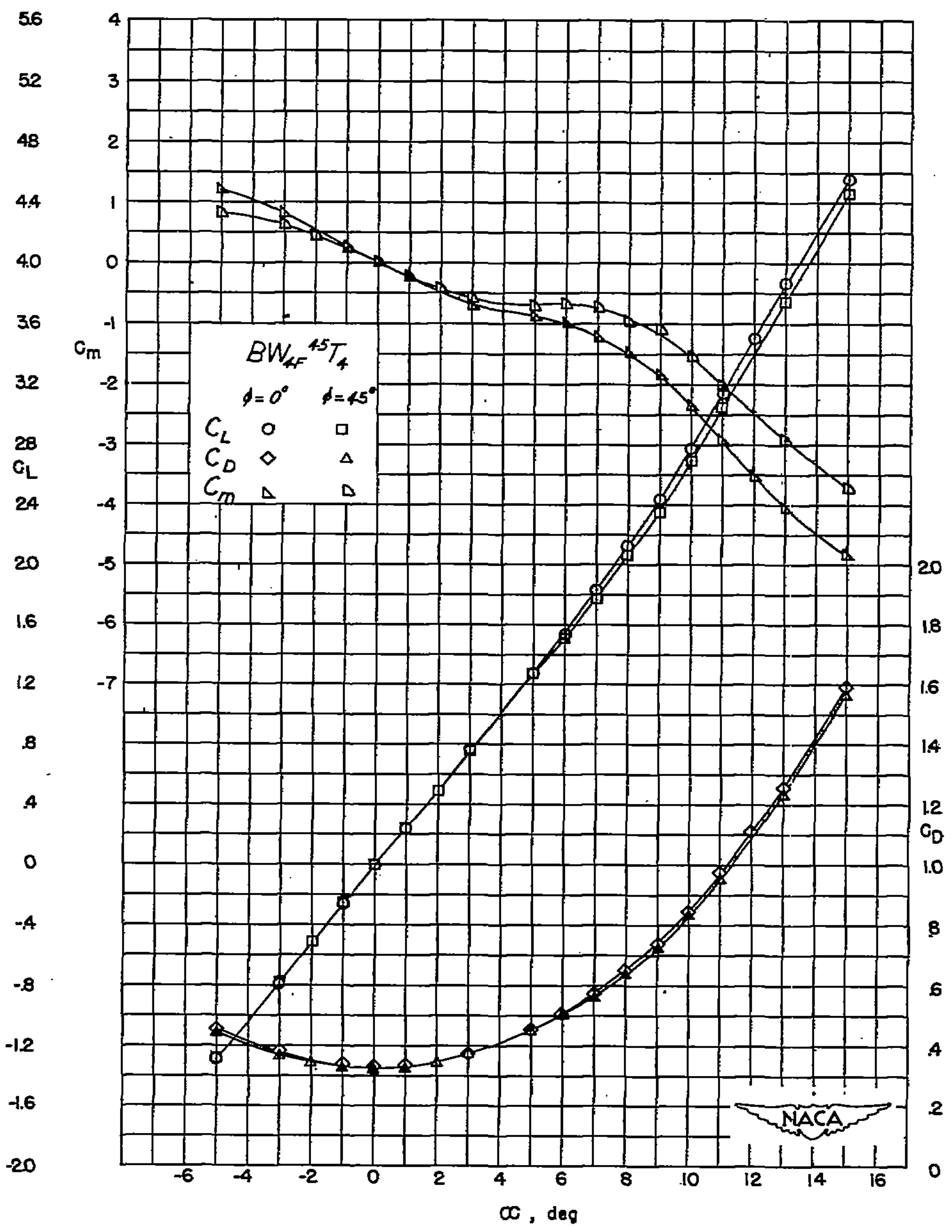

(b) $BW_{4F}{}^{45}T_4$.

Figure 14.- Continued.

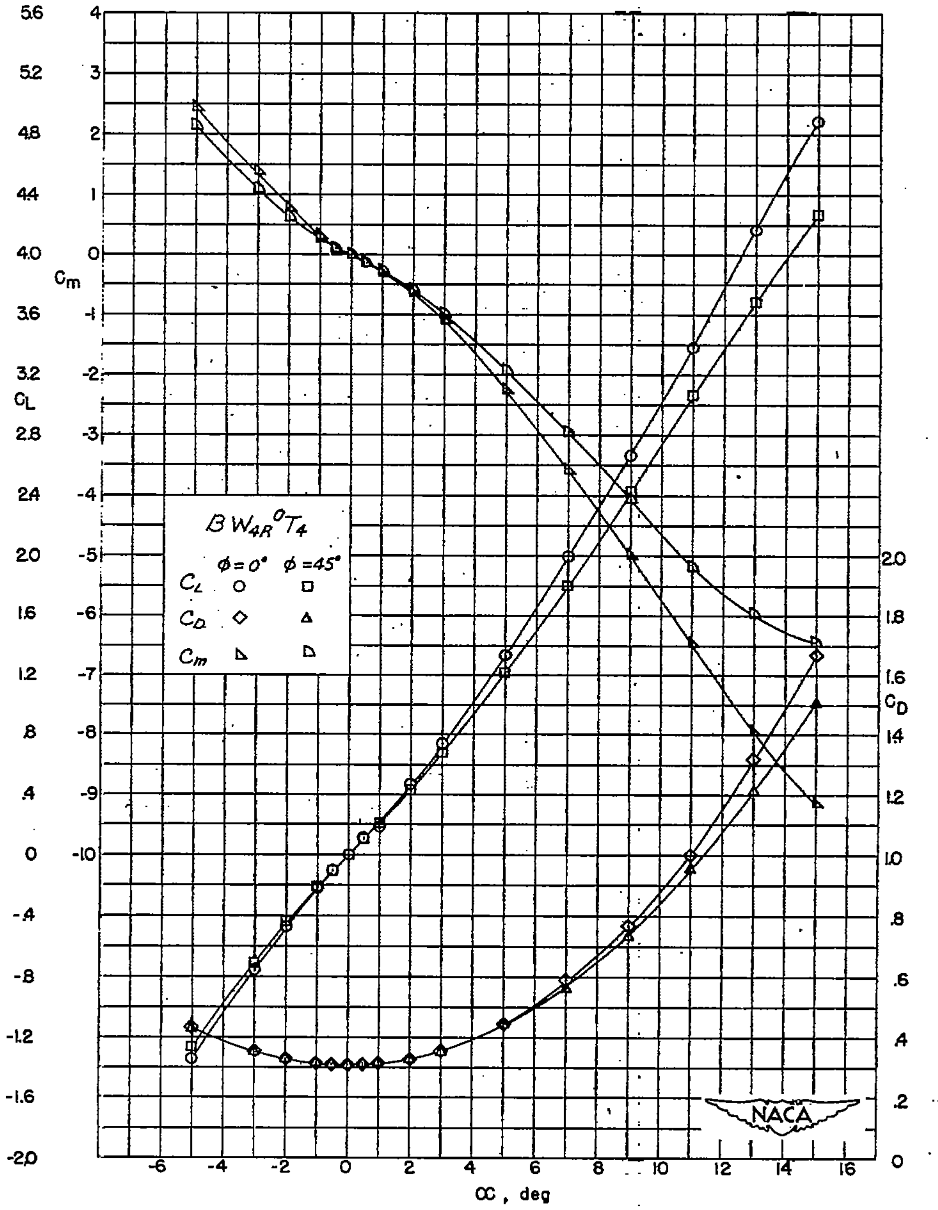

(c) $BW_{4R}{}^{O}T_4$

Figure 14.- Continued.

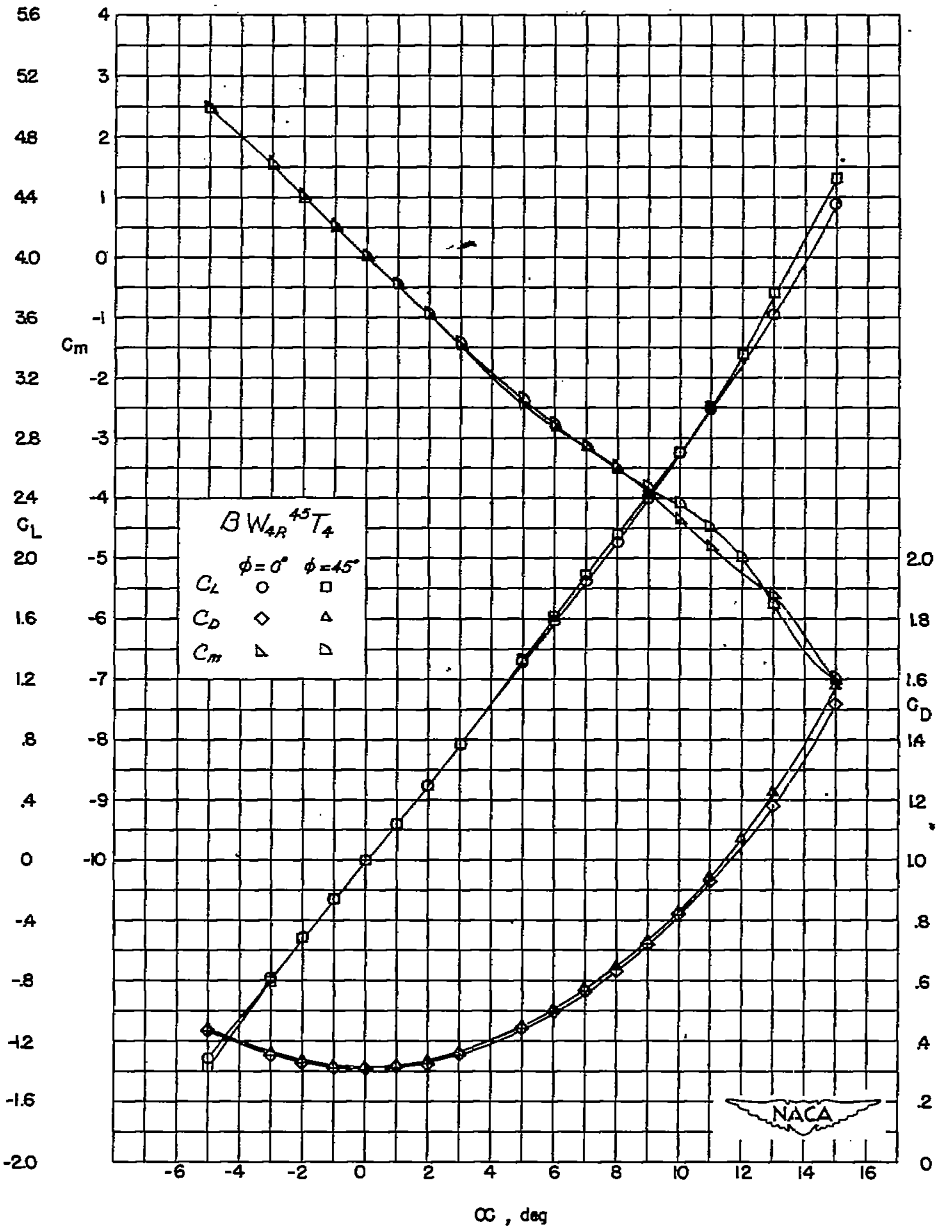

(d) $BW_{4R}{}^{45}T_4$.

Figure 14.- Concluded.

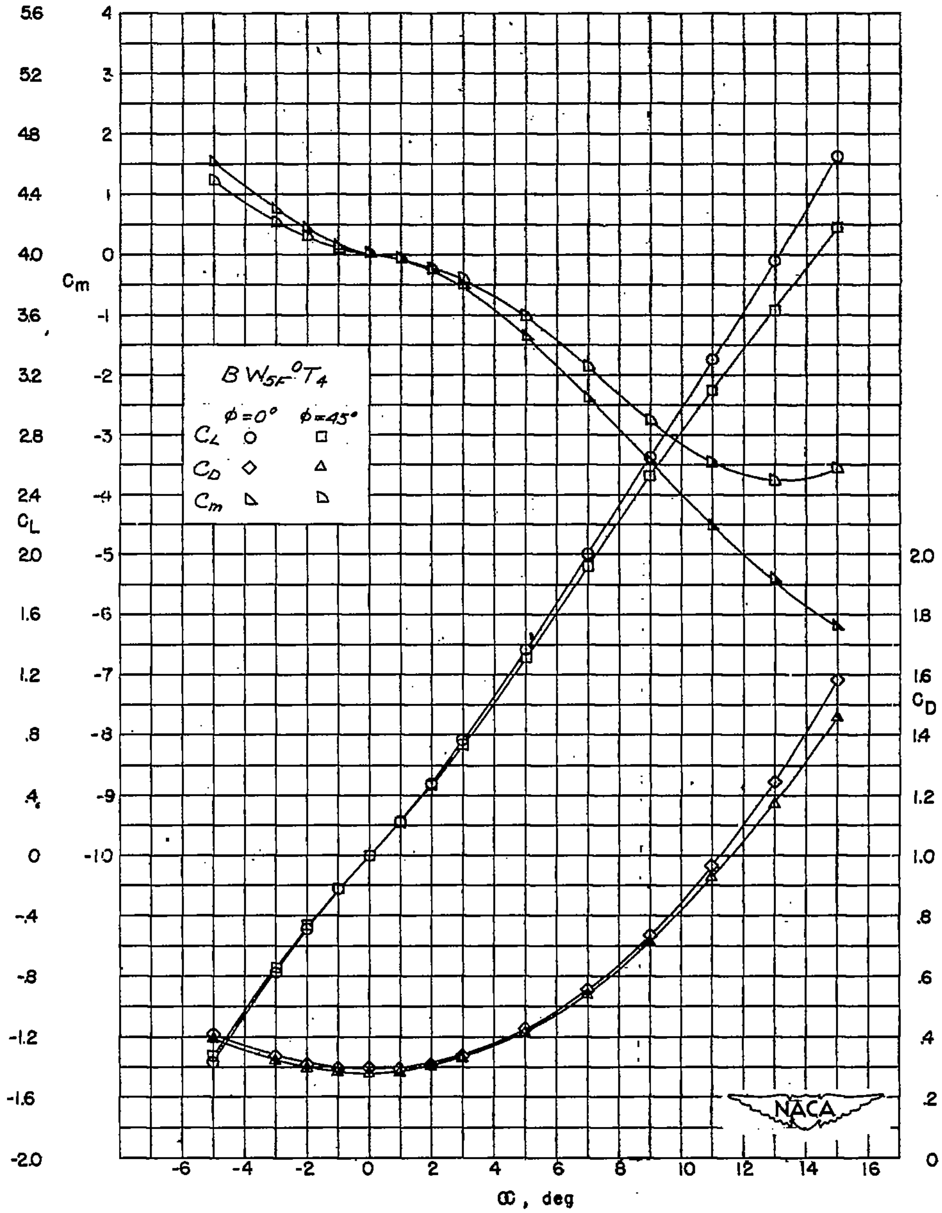

(a) $BW_{5F}{}^{0}T_4$.

Figure 15.- Lift, drag, and pitching-moment characteristics of model combinations of B, W_5, and T_4.

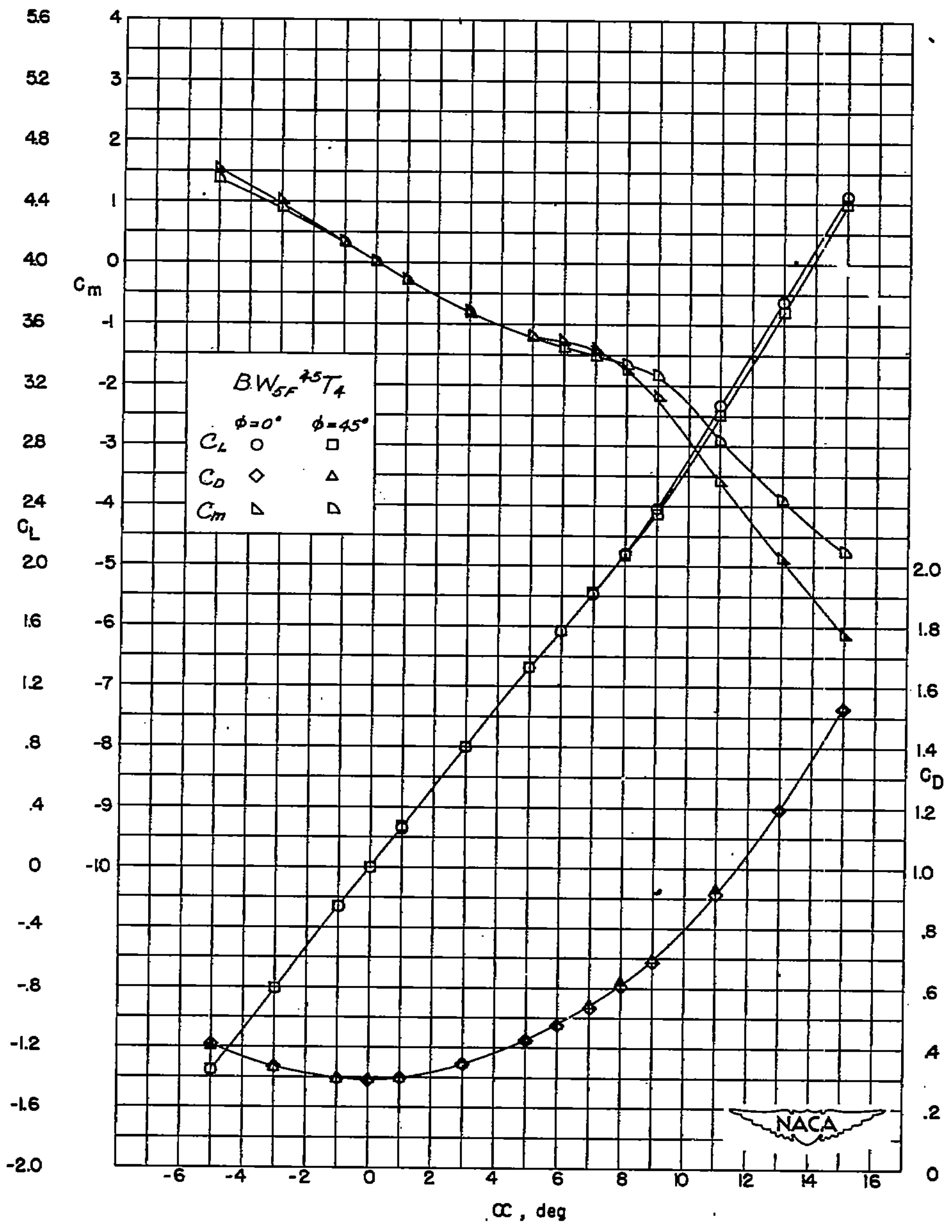

(b) $BW_{5F}{}^{45}T_4$.

Figure 15.- Continued.

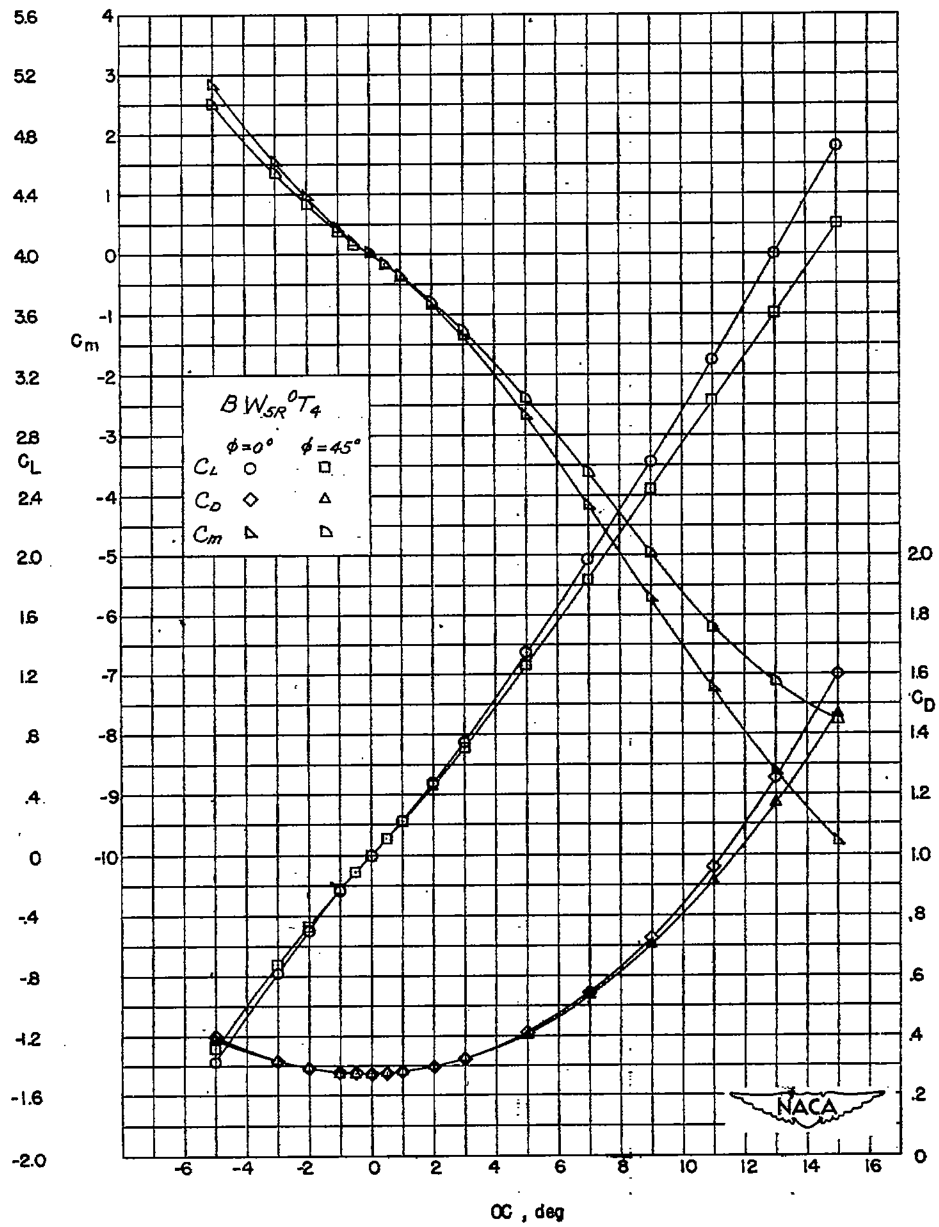

(c) $BW_{5F}{}^{0}T_4$.

Figure 15.- Continued.

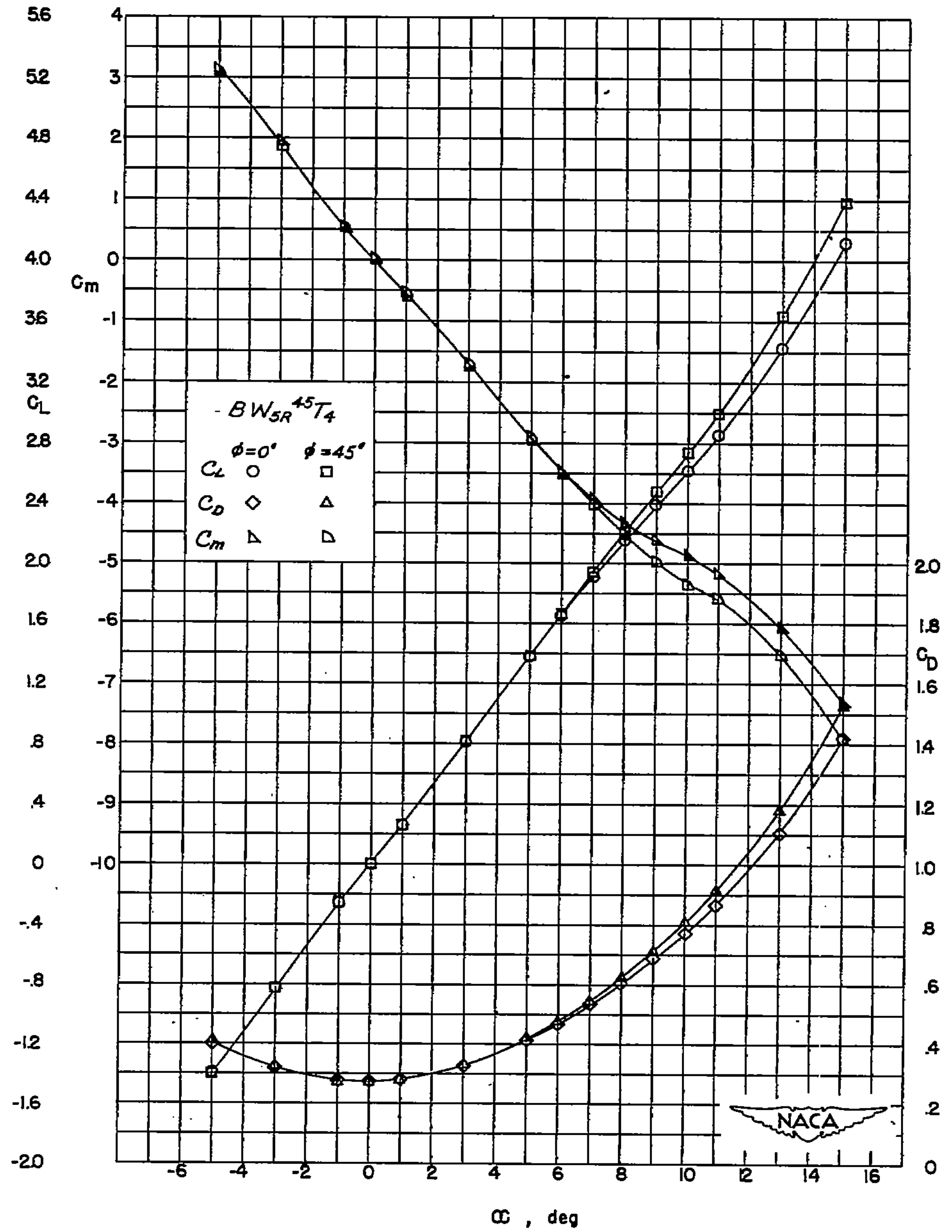

(d) $BW_{5F}{}^{45}T_4$.

Figure 15.- Concluded.

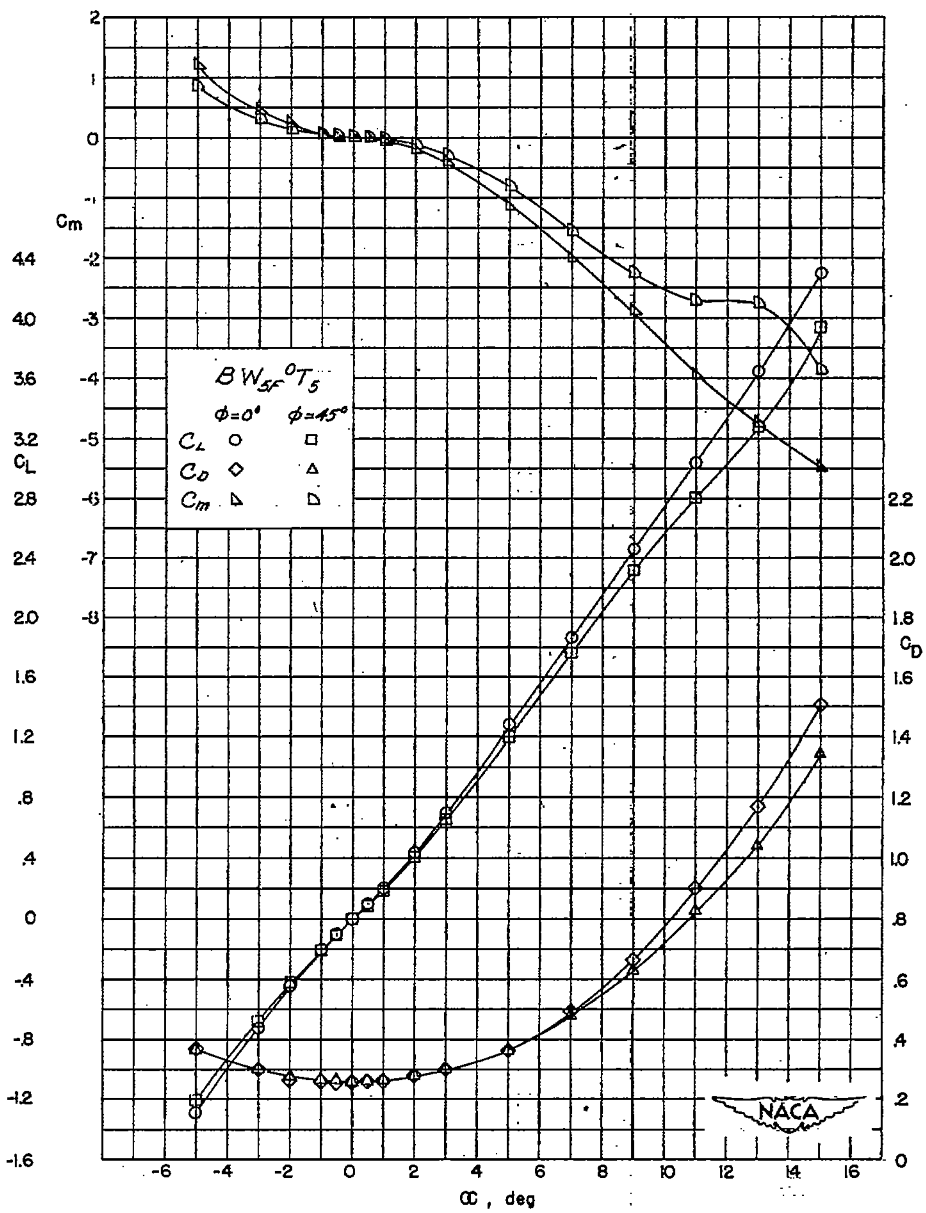

(a) $BW_{5F}{}^{0}T_5$.

Figure 16.- Lift, drag, and pitching-moment characteristics of model combinations of B, W_5, and T_5.

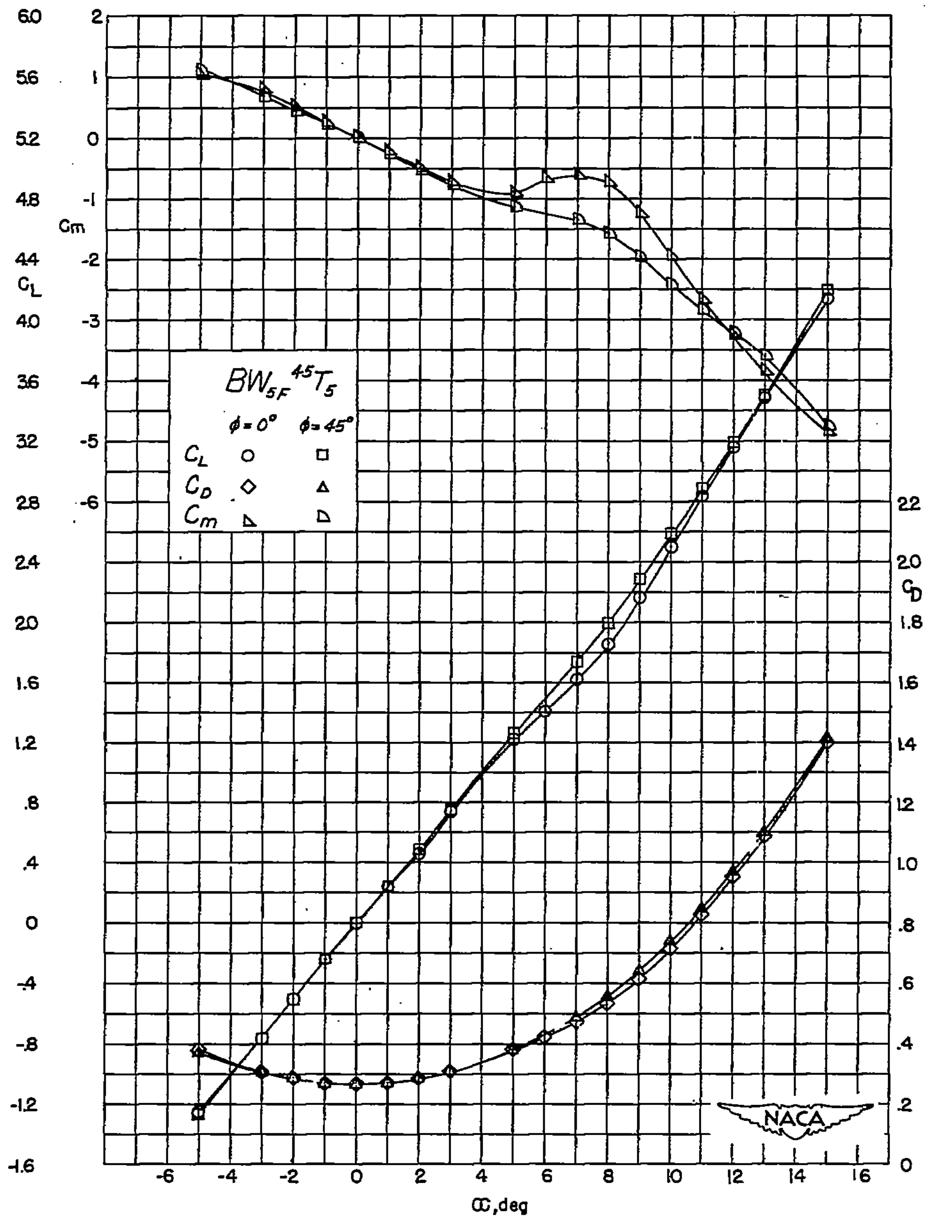

(b) $BW_{5F}{}^{45}T_5$.

Figure 16.- Continued.

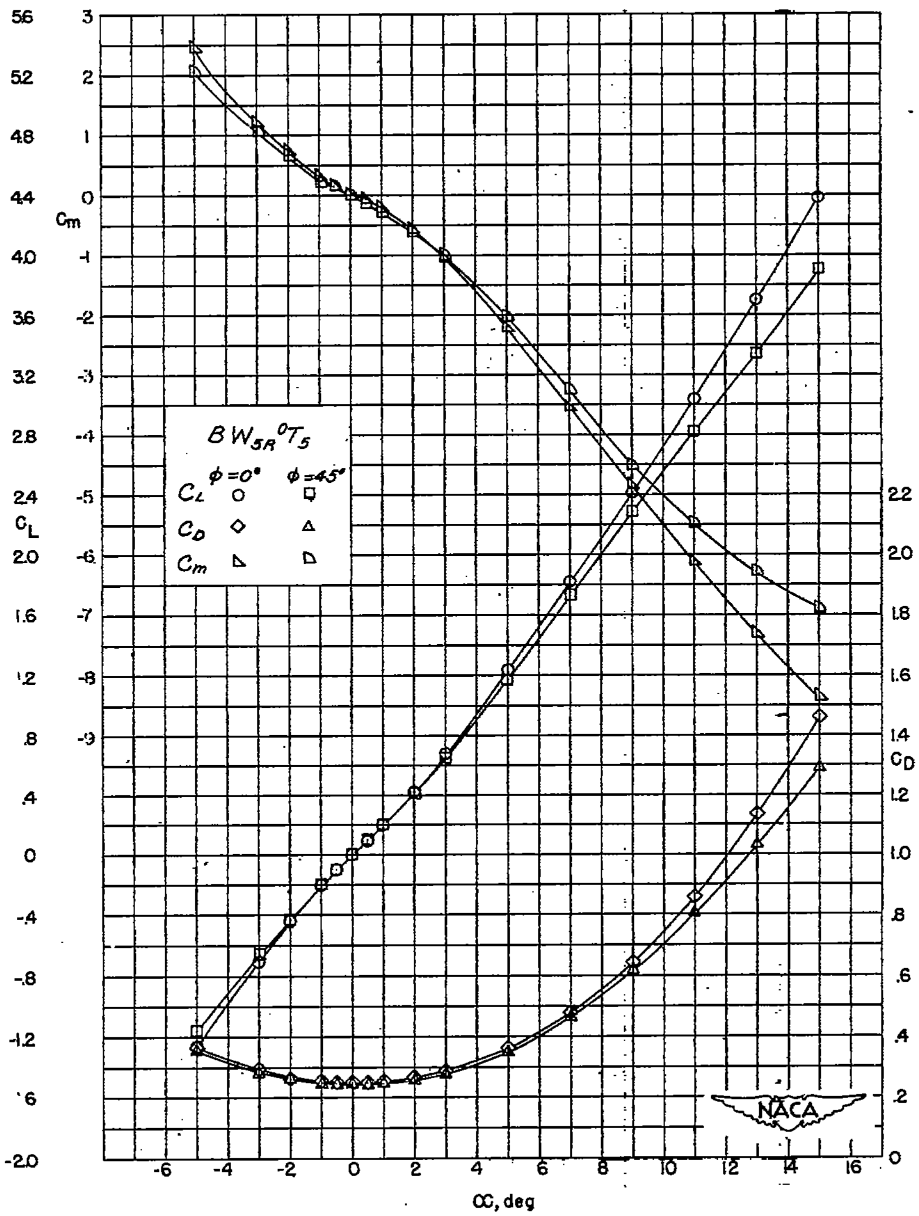

(c) $BW_{5R}{}^{0}T_5$.

Figure 16.- Continued.

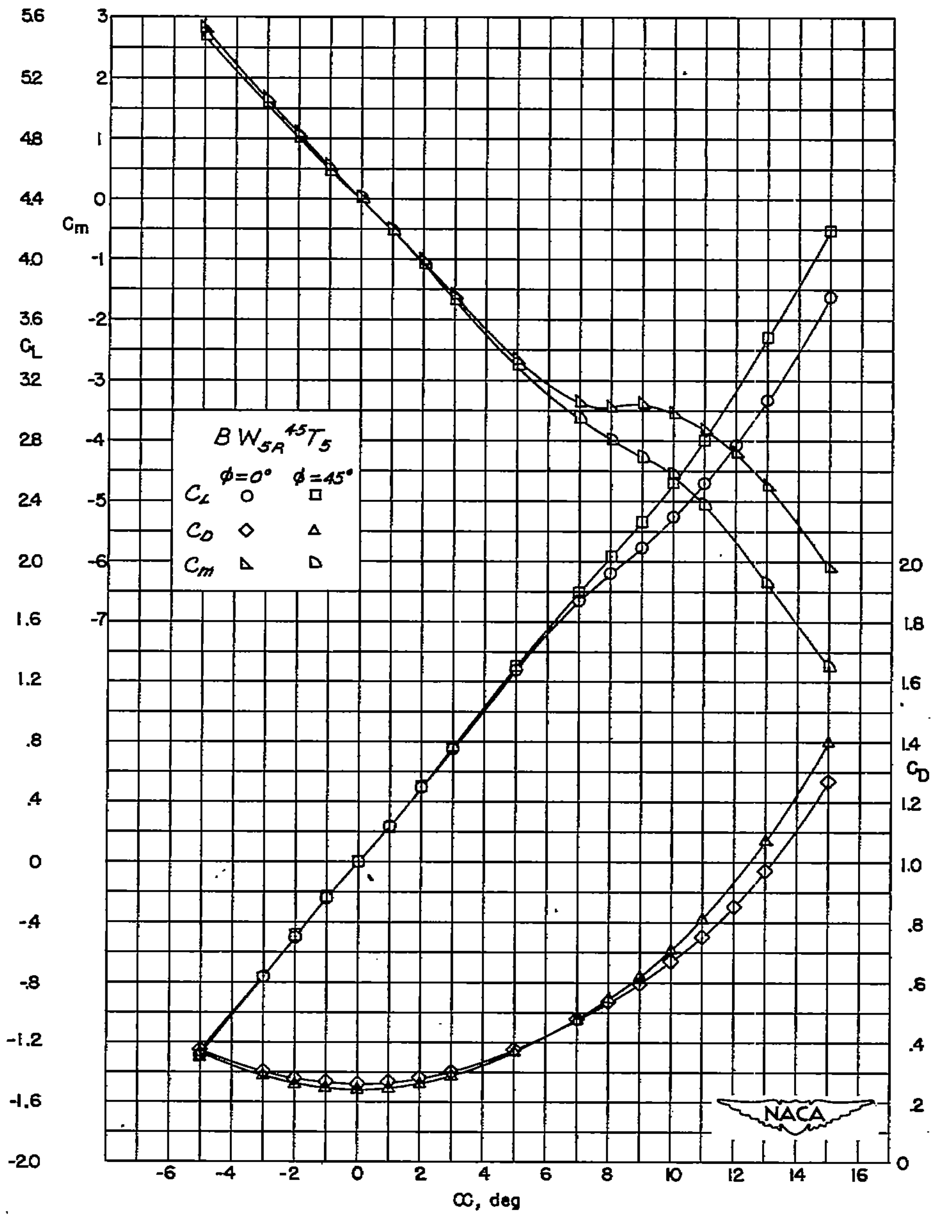

(d) $BW_{5R}{}^{45}T_5$.

Figure 16.- Concluded.

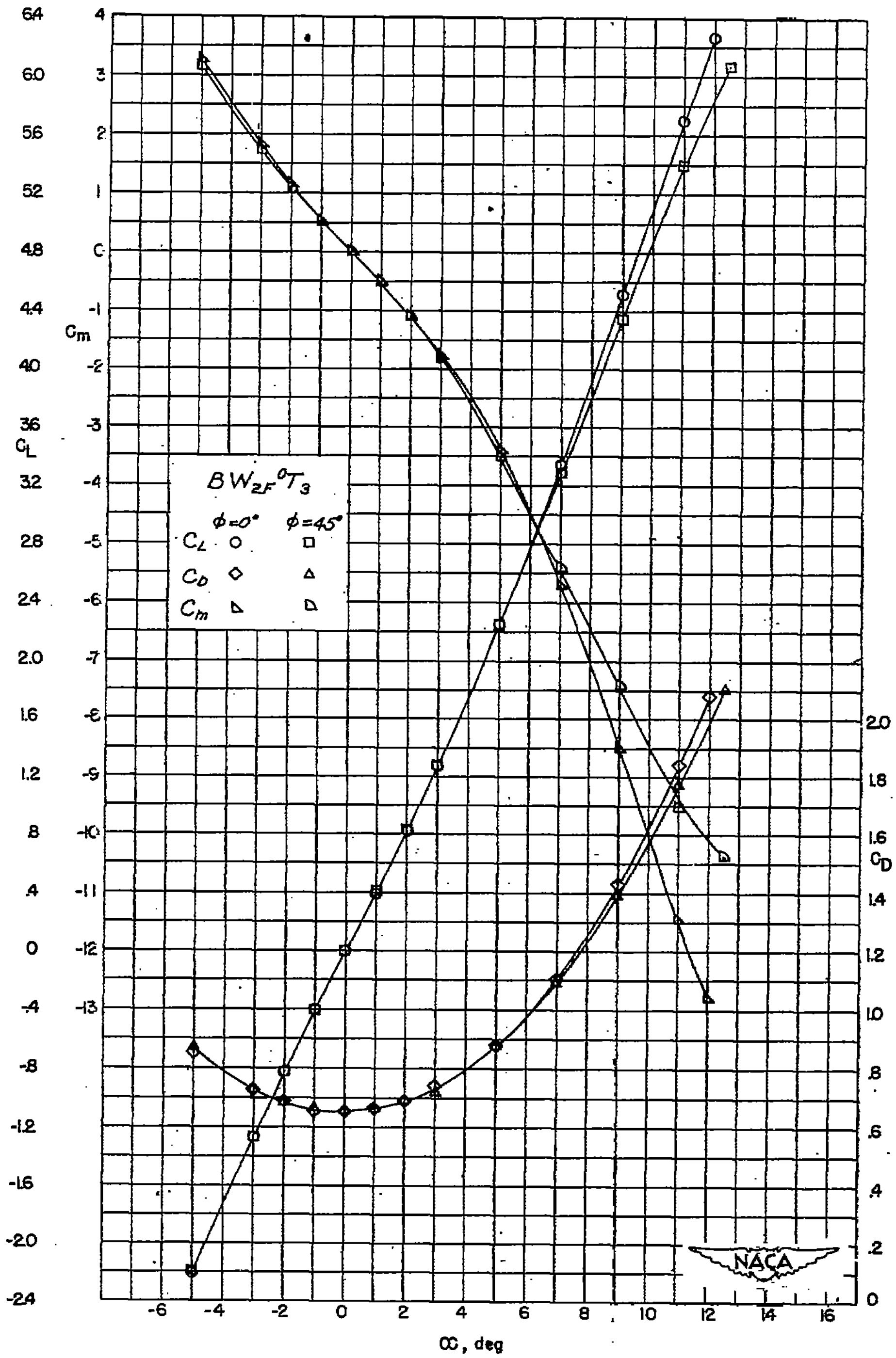

(a) $BW_{2F}{}^{0}T_3$.

Figure 17.- Lift, drag, and pitching-moment characteristics of model combinations of B, W_2, and T_3.

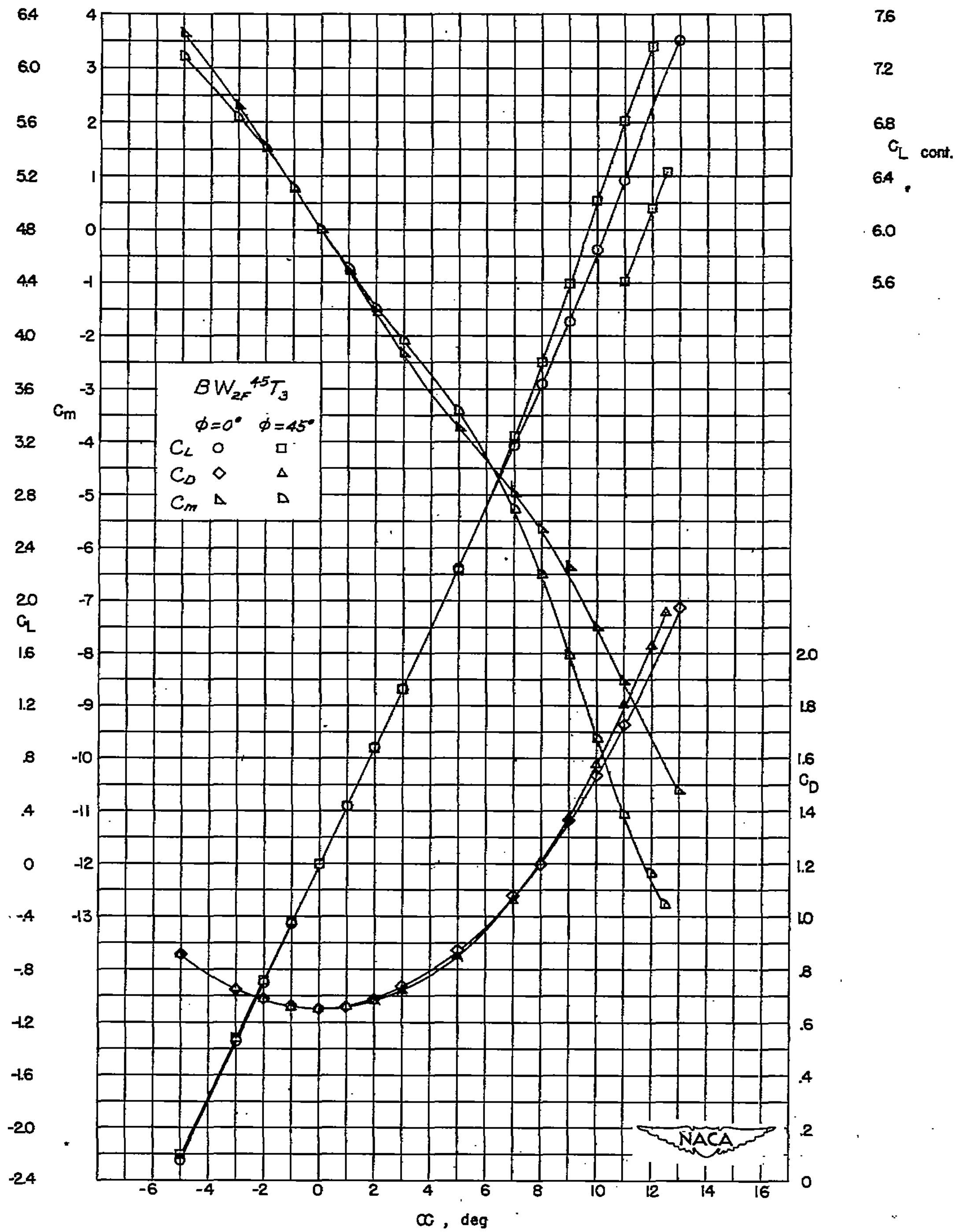

(b) $BW_{2F}^{45}T_3$.

Figure 17.- Continued.

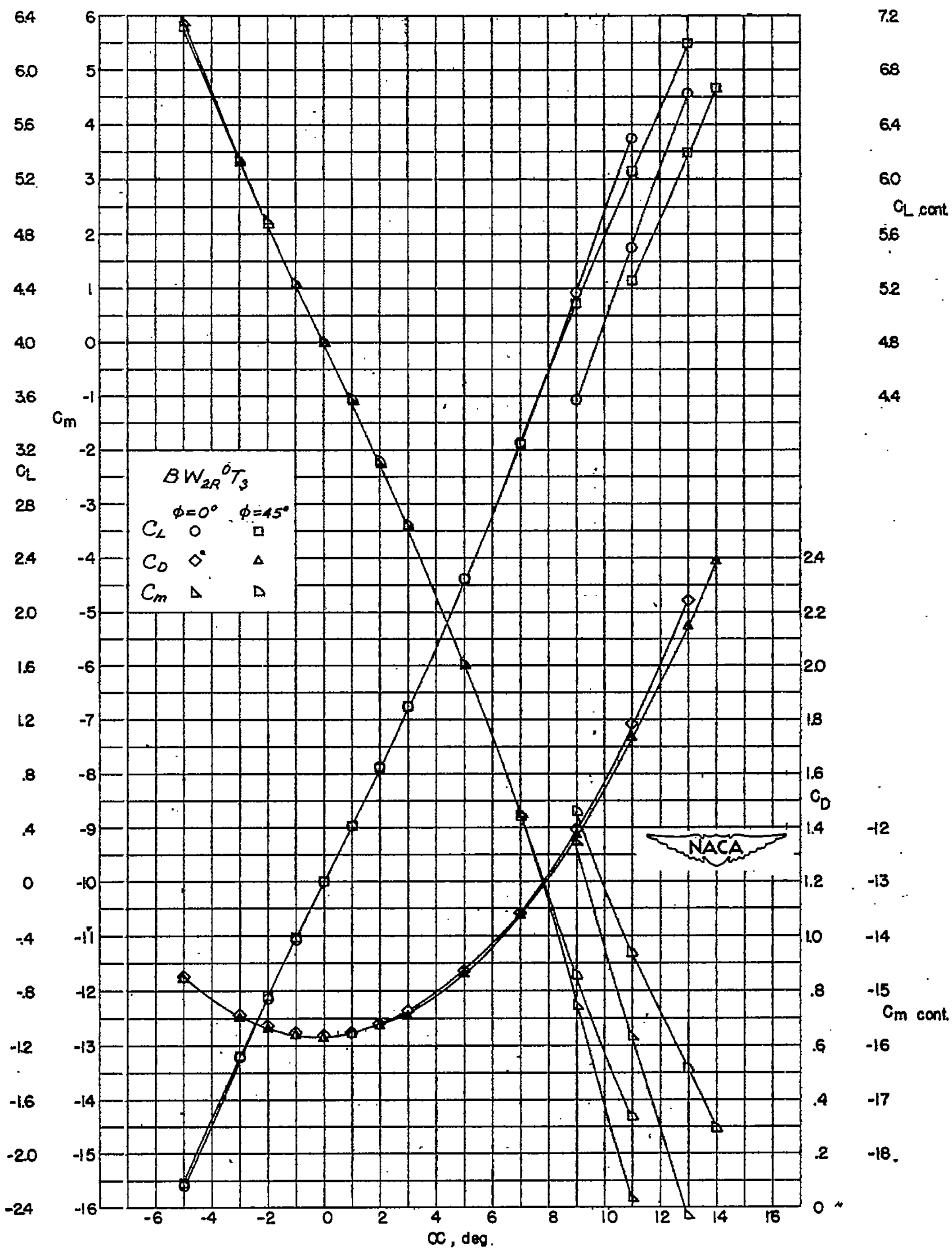

(c) $BW_{2R}{}^{0}T_3$.

Figure 17.- Continued.

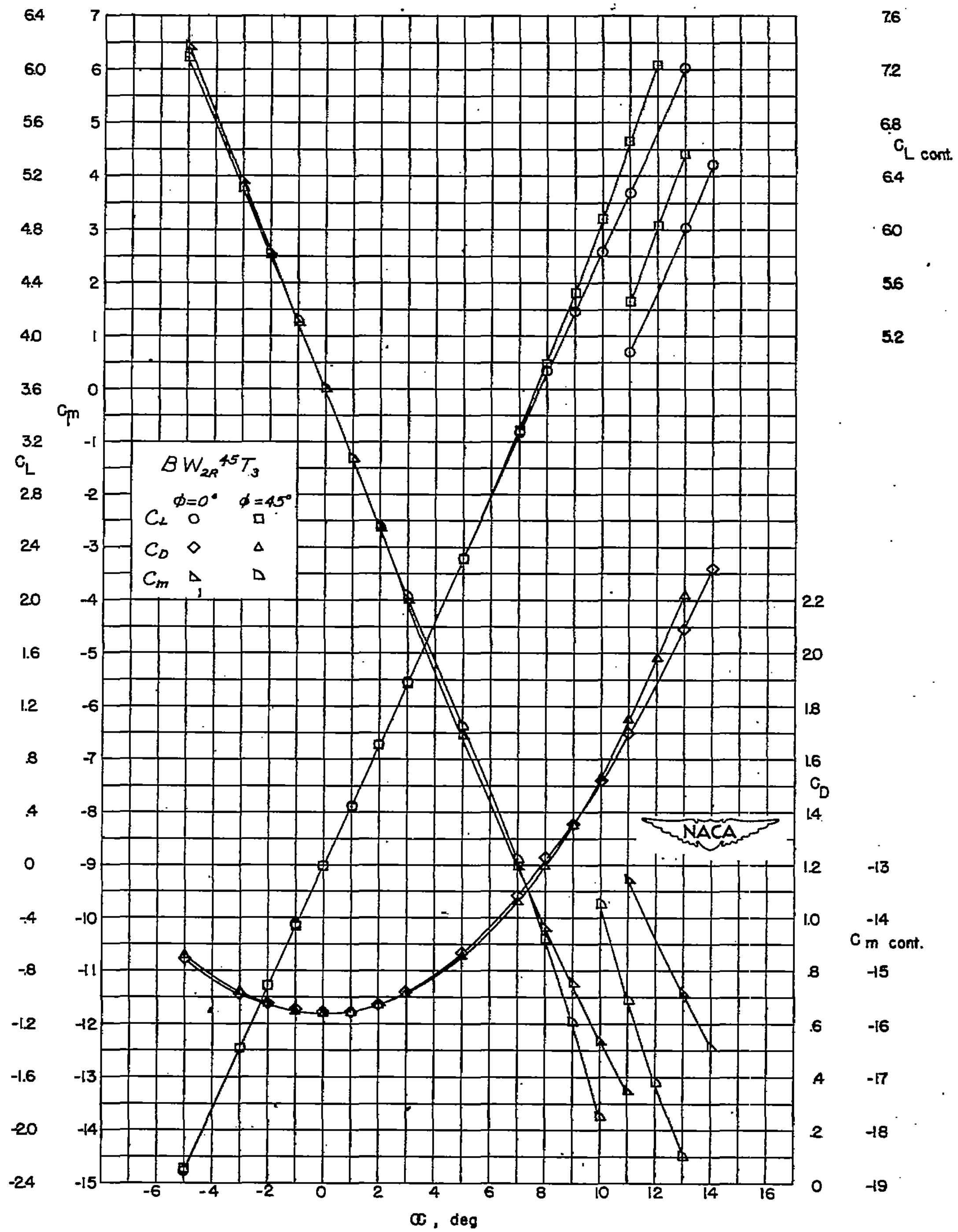

(d) $BW_{2R}{}^{45}T_3$.

Figure 17.- Concluded.

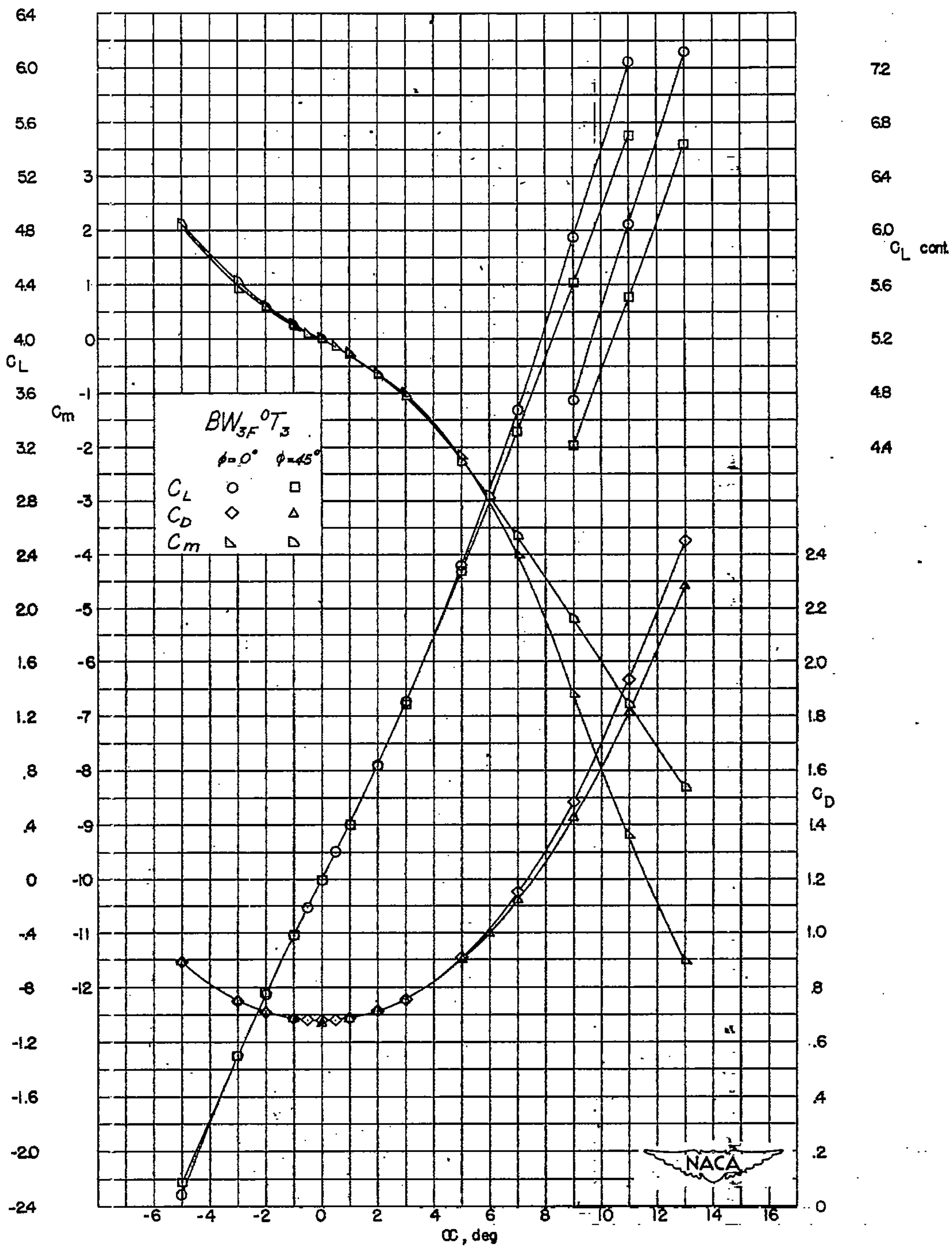

(a) $BW_{3F}{}^{0}T_3$.

Figure 18.- Lift, drag, and pitching-moment characteristics of model combinations of B, W_3, and T_3.

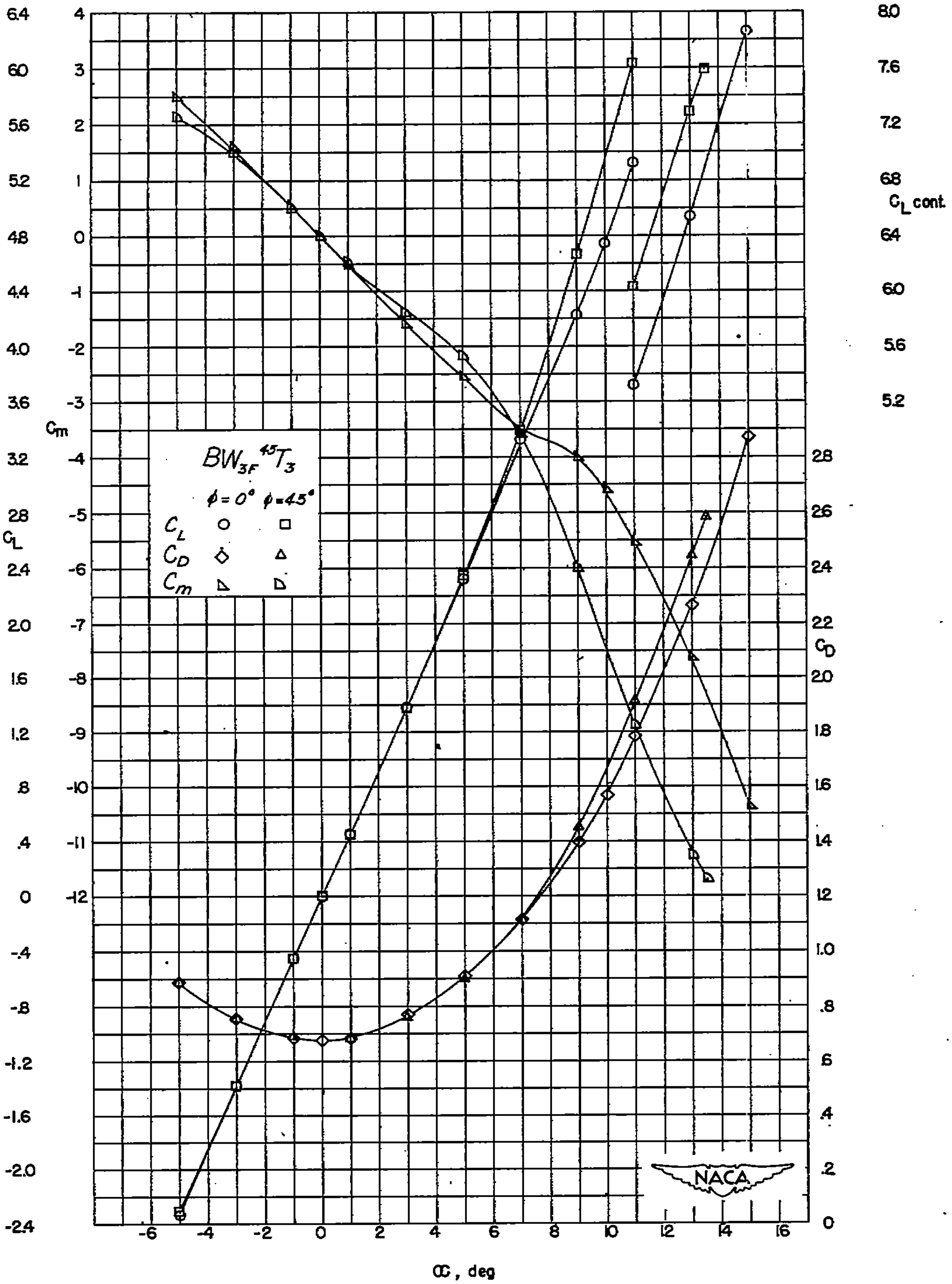

(b) $BW_{3F}{}^{45}T_3$.

Figure 18.- Continued.

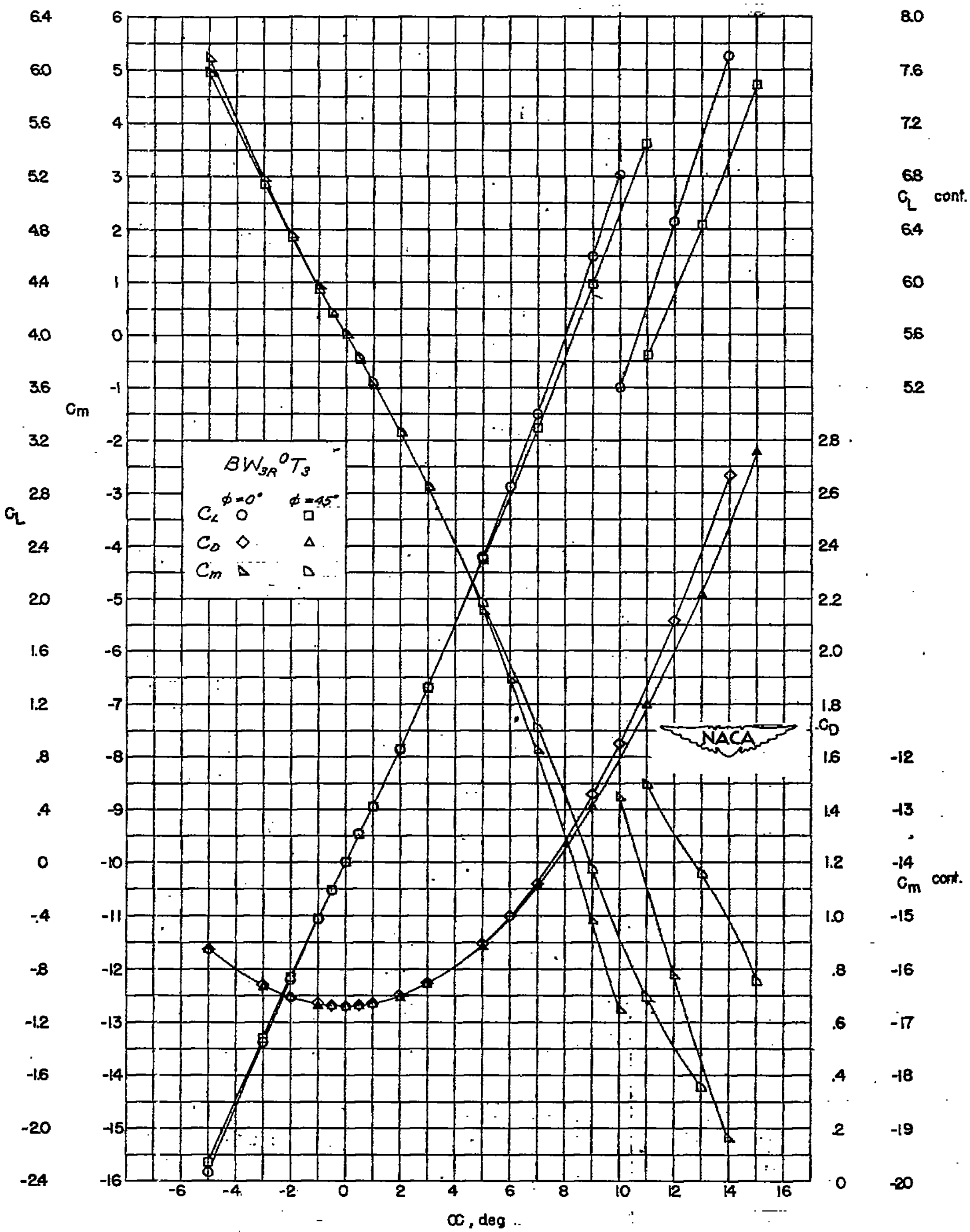

(c) $BW_{3R}{}^{0}T_3$.

Figure 18.- Continued.

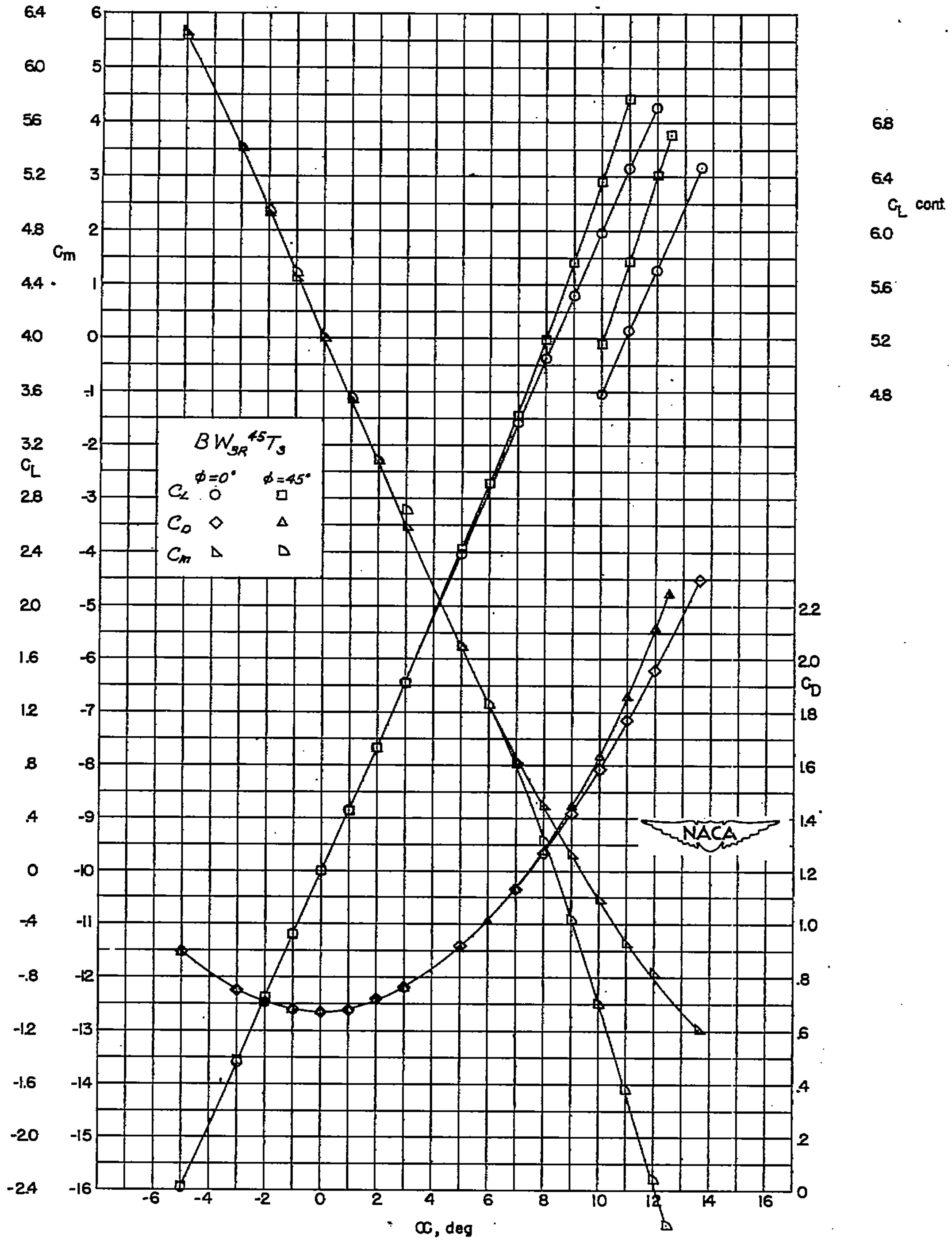

(d) $BW_{3R}{}^{45}T_3$.

Figure 18.- Concluded.

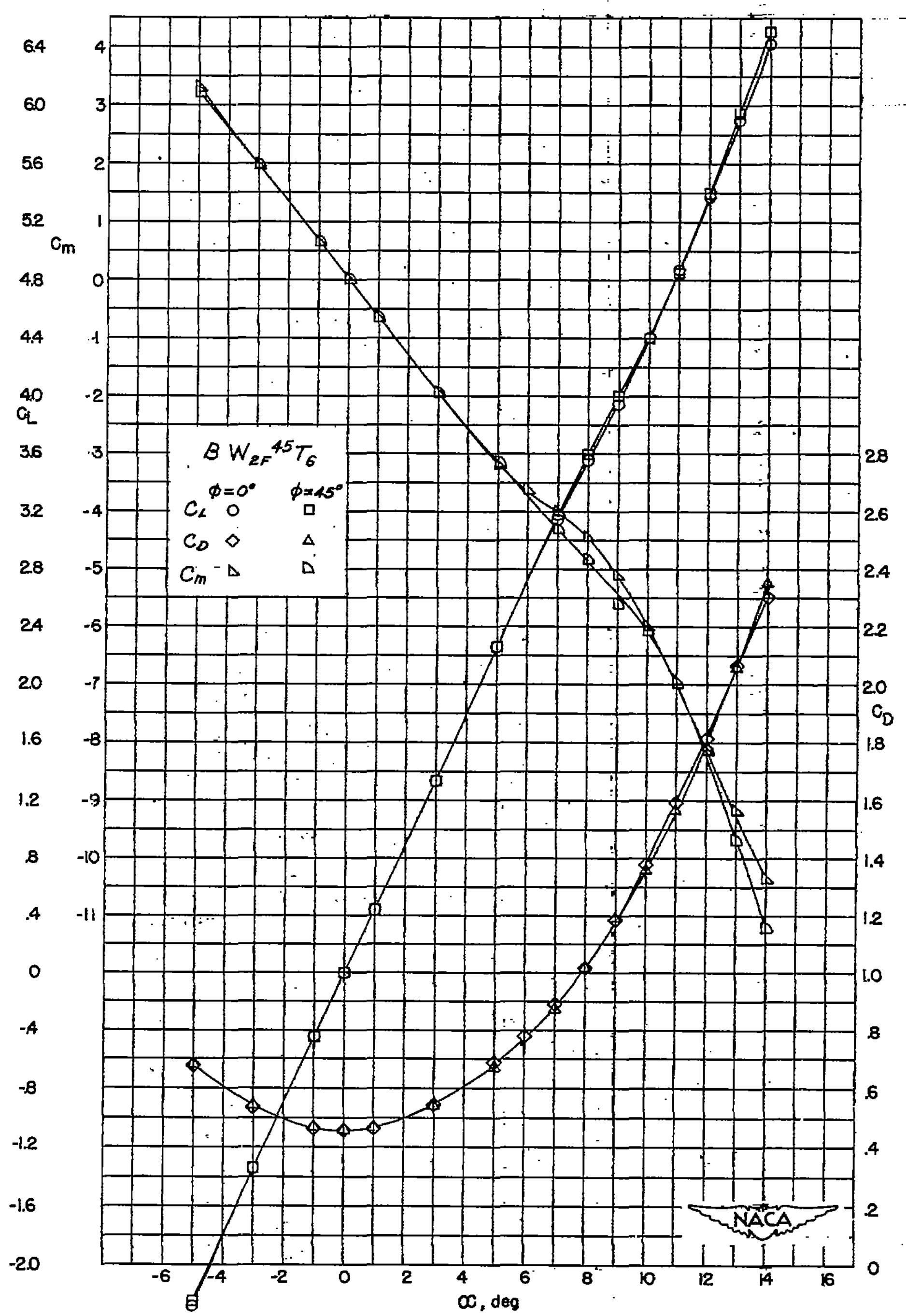

(a) $BW_{2F}{}^{45}T_6$.

Figure 19.- Lift, drag, and pitching-moment characteristics of model combinations of B, W_2, and T_6.

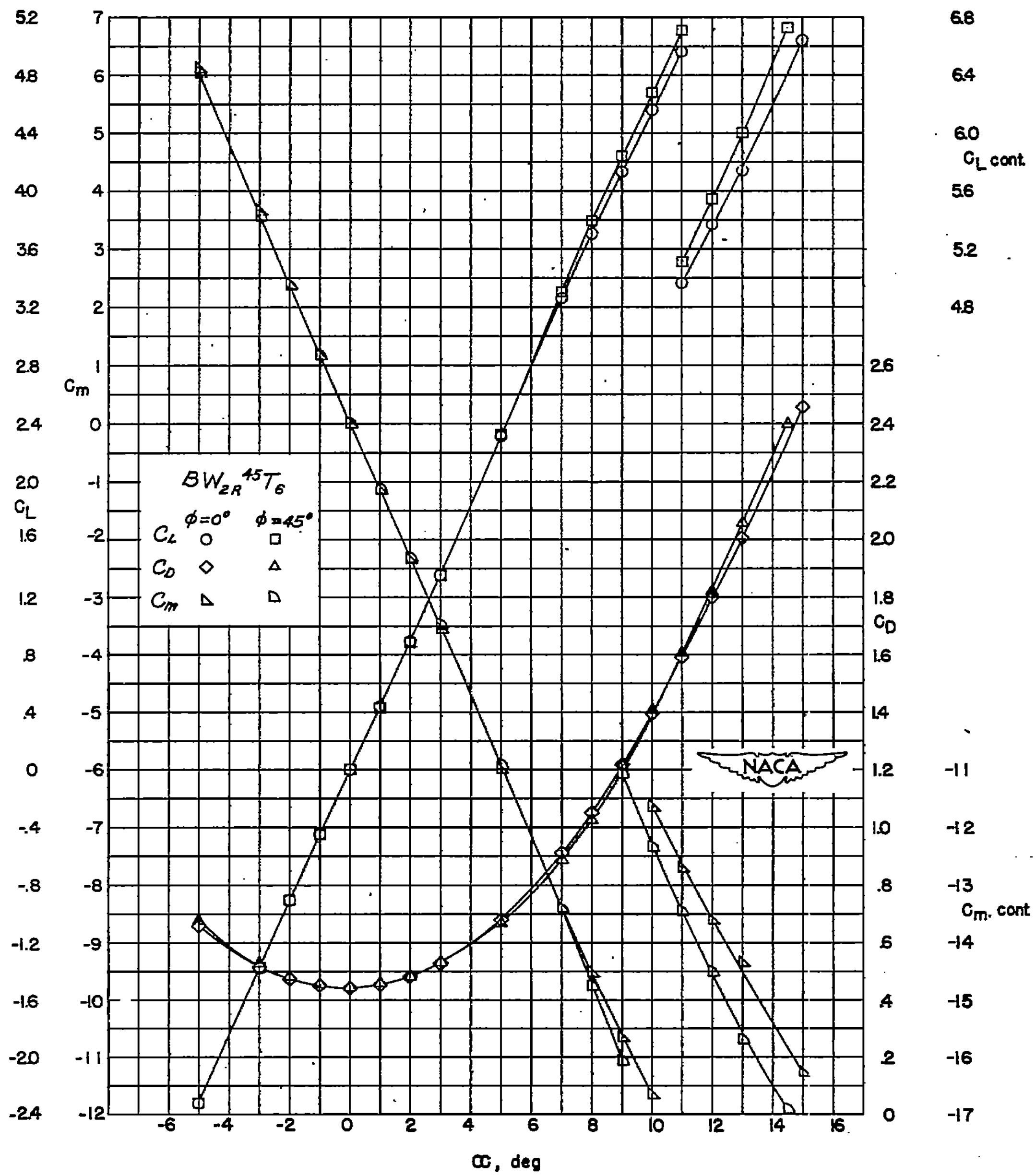

(b) $BW_{2R}{}^{45}T_6$.

Figure 19.- Concluded.

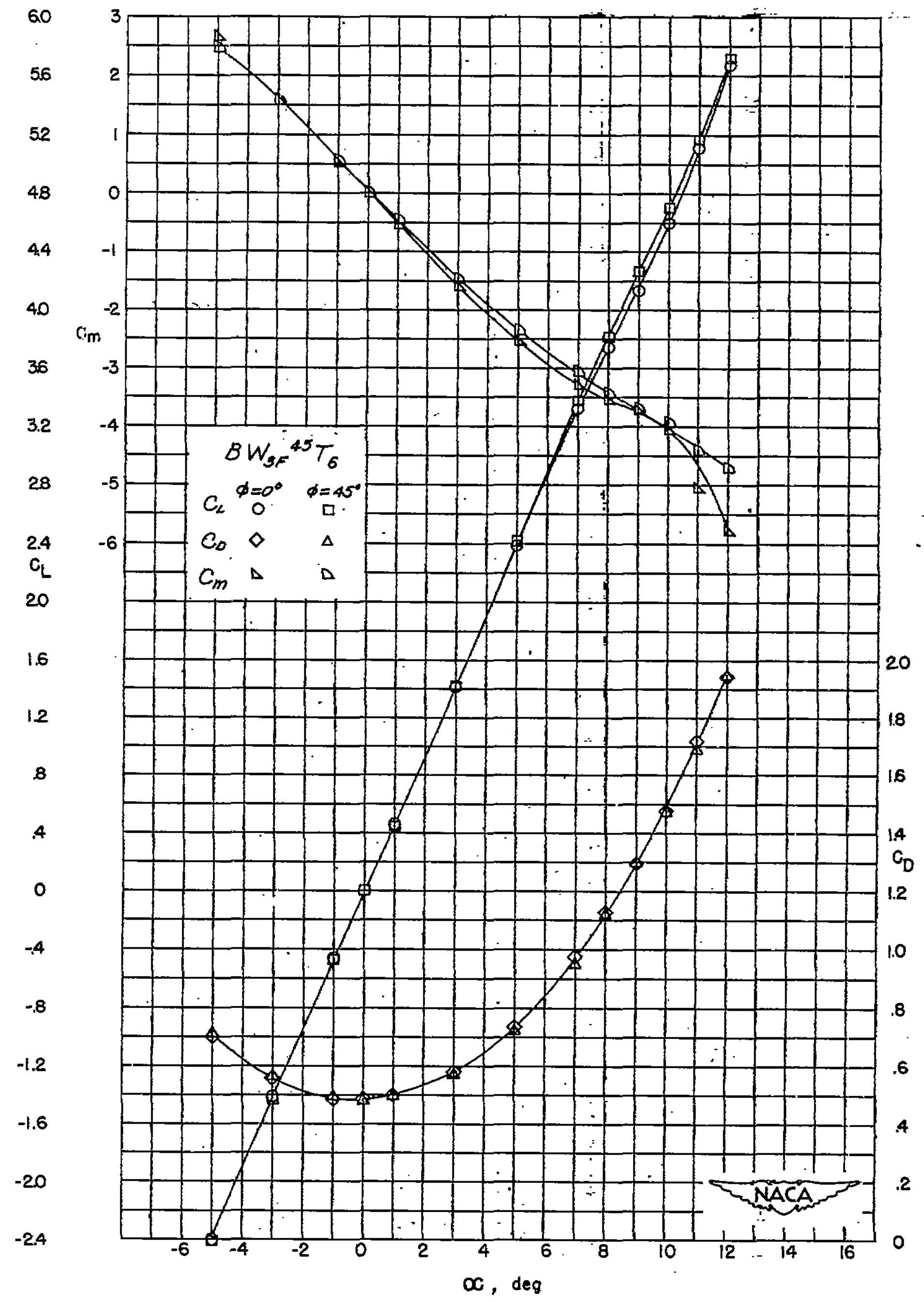

(a) $BW_{3F}{}^{45}T_6$.

Figure 20.- Lift, drag, and pitching-moment characteristics of model combinations of B, W_3, and T_6.

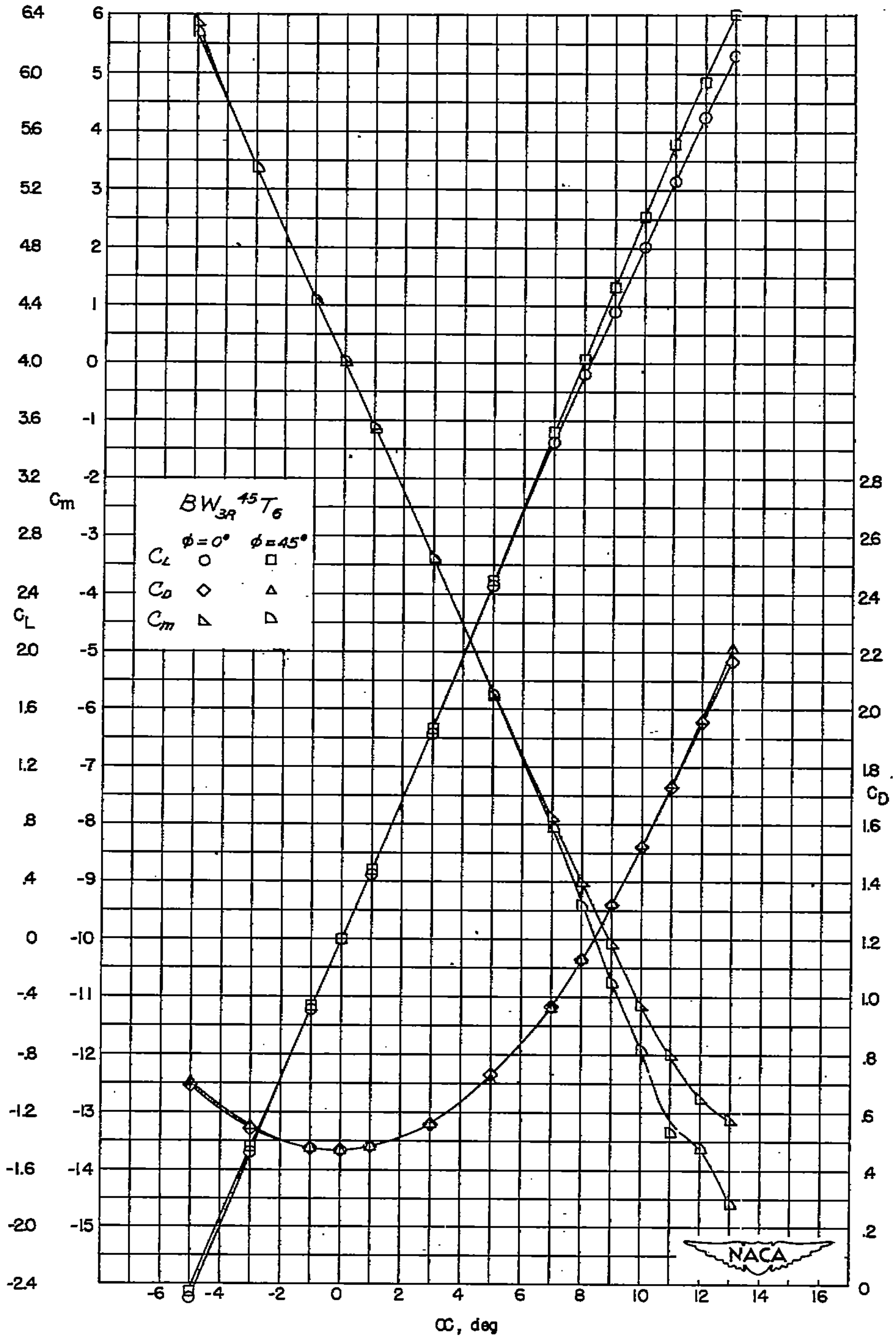

(b) $BW_{3R}{}^{45}T_6$.

Figure 20.- Concluded.

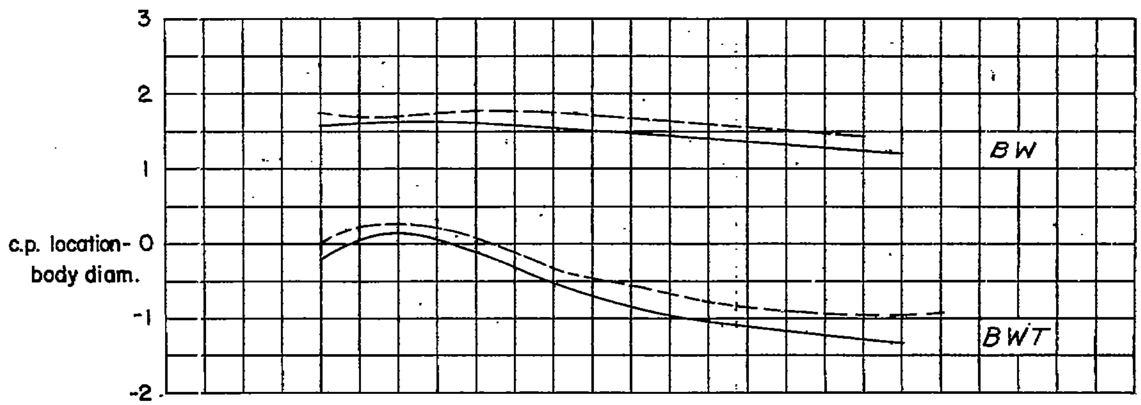

(1) Center-of-pressure variation for $BW_{1F}{}^{O}T_1$ and BW_{1F}.

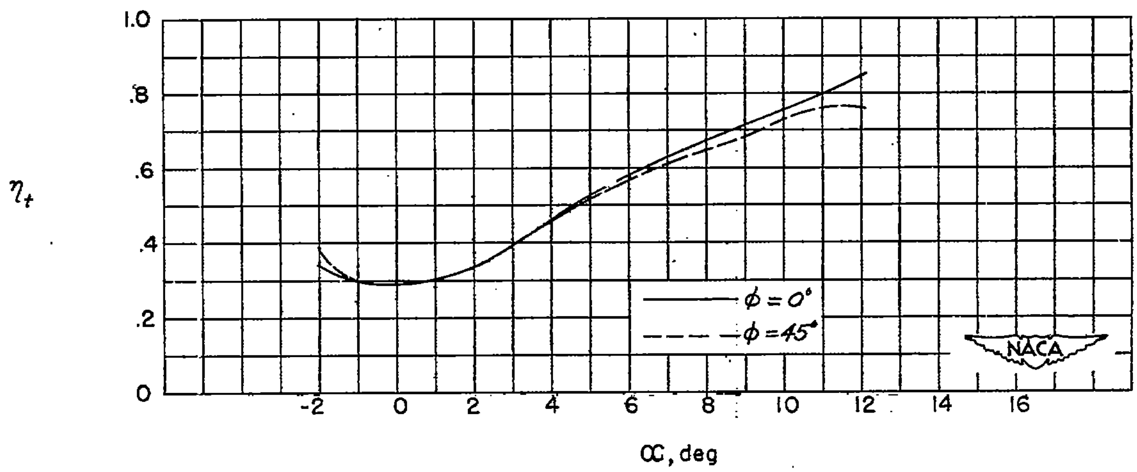

(2) Tail-lift efficiency factor variation for $BW_{1F}{}^{O}T_1$.

(a) $BW_{1F}{}^{O}T_1$.

Figure 21.- Center-of-pressure characteristics and body-wing-tail interference factors for configurations having W_1 and T_1.

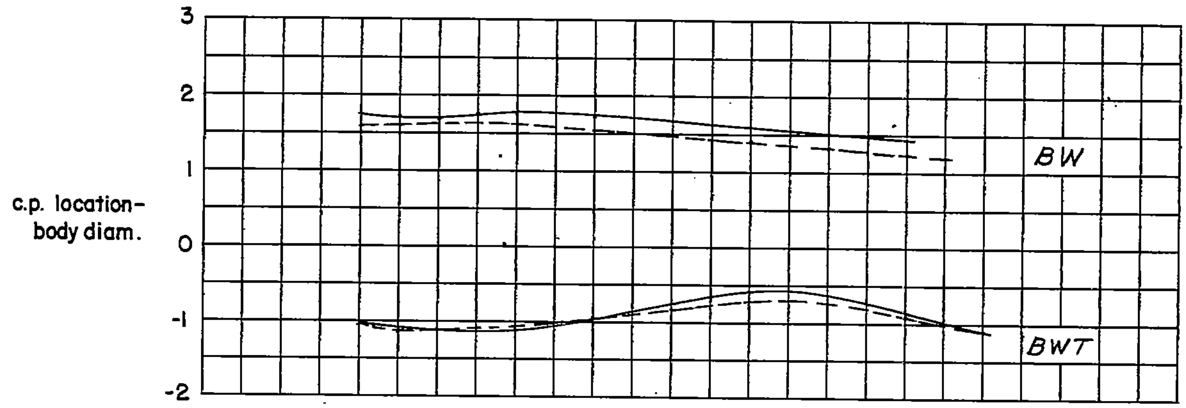

(1) Center-of-pressure variation for $BW_{1F}{}^{45}T_1$ and BW_{1F}.

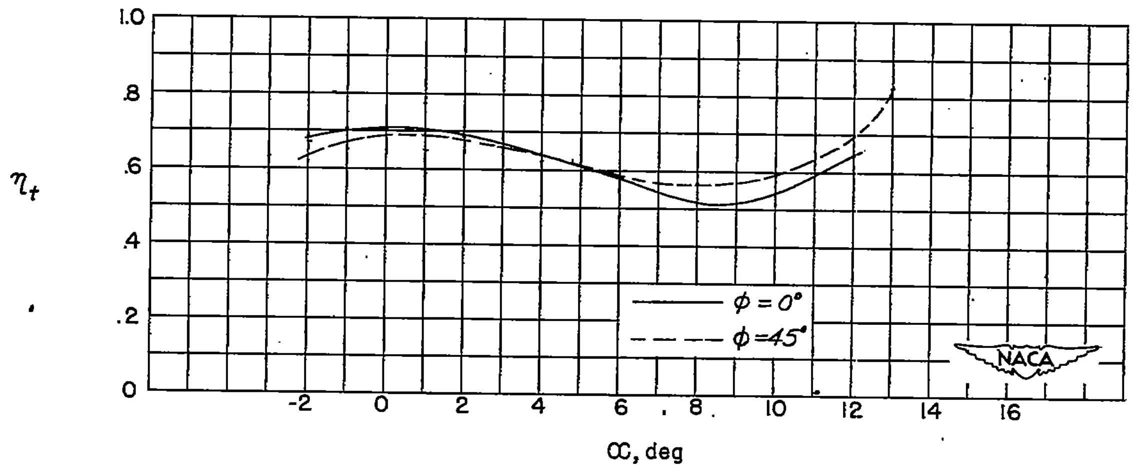

(2) Tail-lift efficiency factor variation for $BW_{1F}{}^{45}T_1$.

(b) $BW_{1F}{}^{45}T_1$.

Figure 21.- Continued.

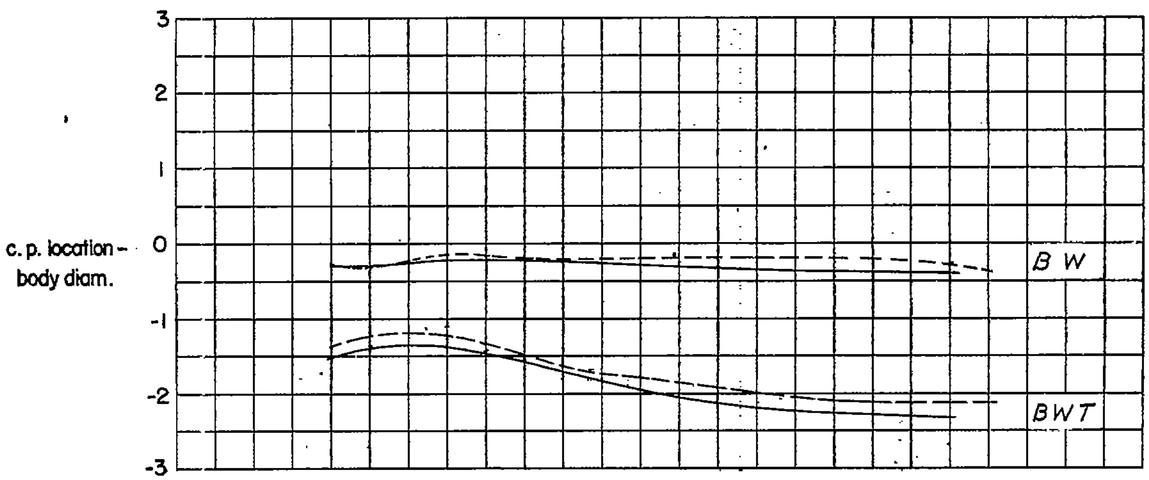

(1) Center-of-pressure variation for $BW_{1R}{}^{O}T_1$ and BW_{1R}.

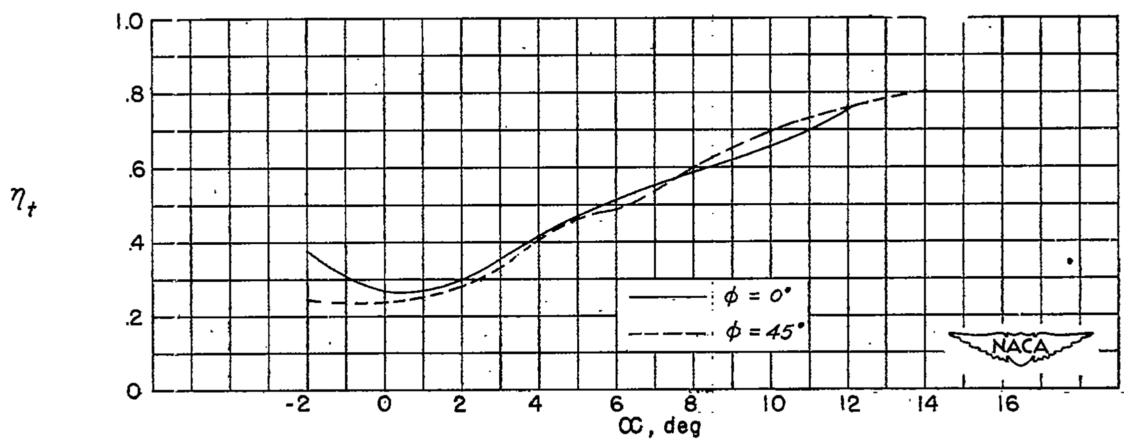

(2) Tail-lift efficiency factor variation for $BW_{1R}{}^{O}T_1$.

(c) $BW_{1R}{}^{O}T_1$.

Figure 21.- Continued.

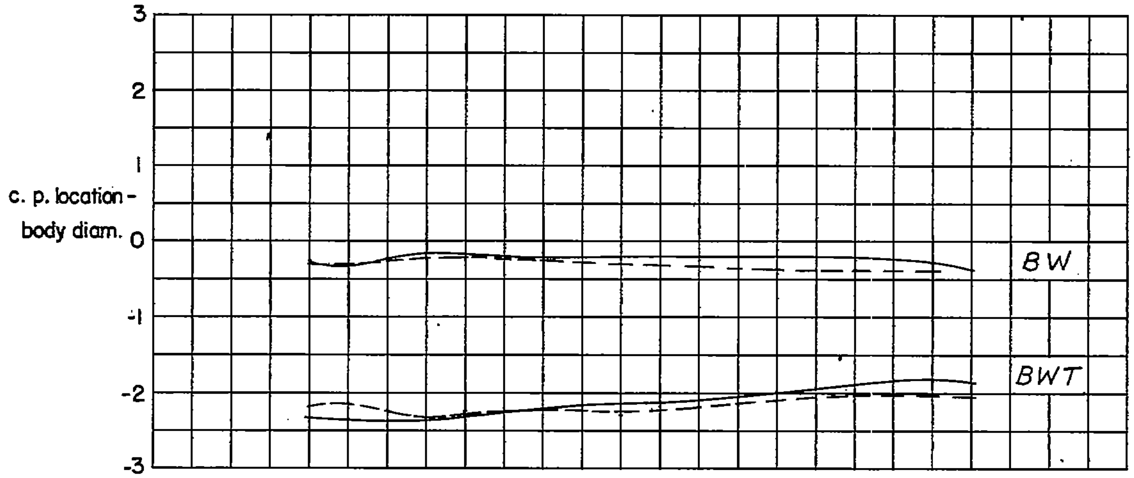

(1) Center-of-pressure variation for $BW_{1R}{}^{45}T_1$ and BW_{1R}.

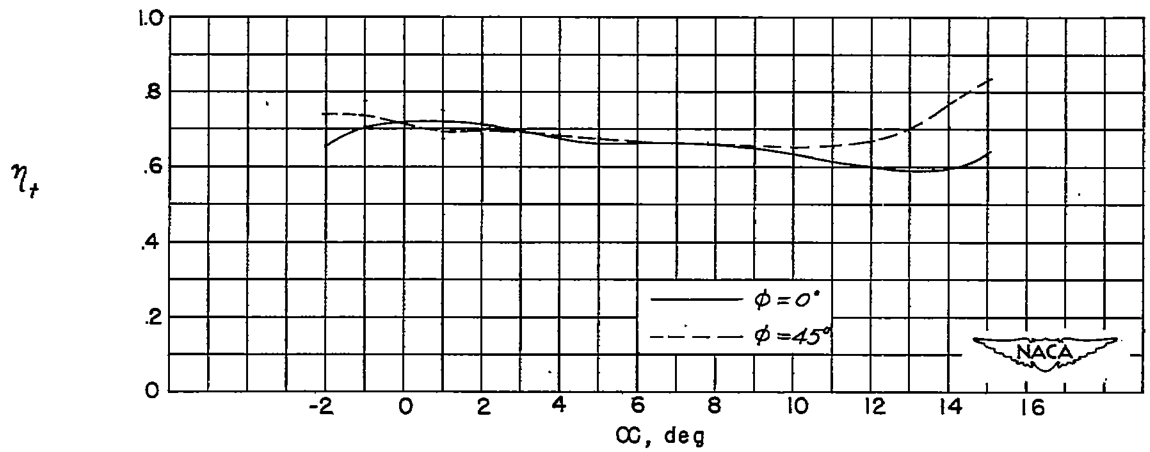

(2) Tail-lift efficiency factor variation for $BW_{1R}{}^{45}T_1$.

(d) $BW_{1R}{}^{45}T_1$.

Figure 21.- Concluded.

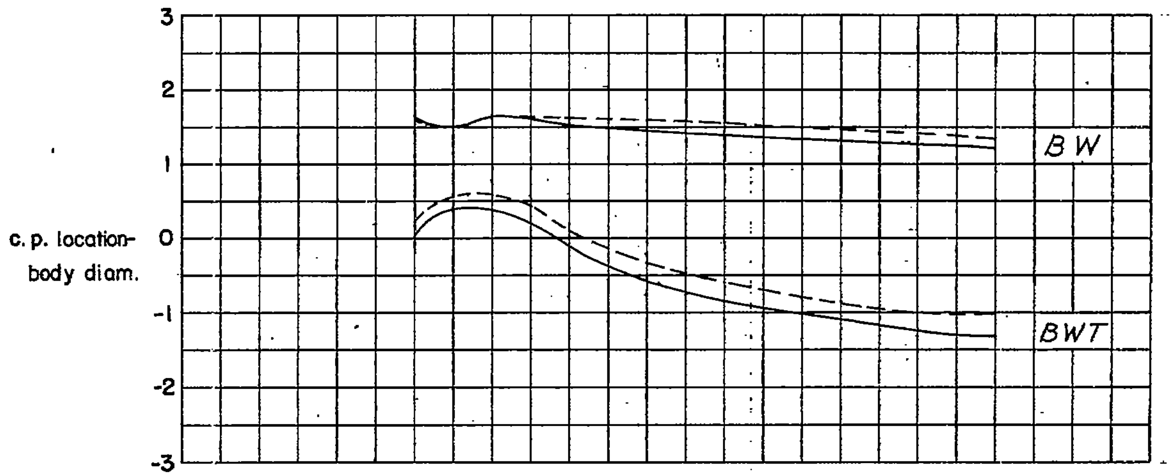

(1) Center-of-pressure variation for $BW_{2F}{}^{0}T_2$ and BW_{2F}.

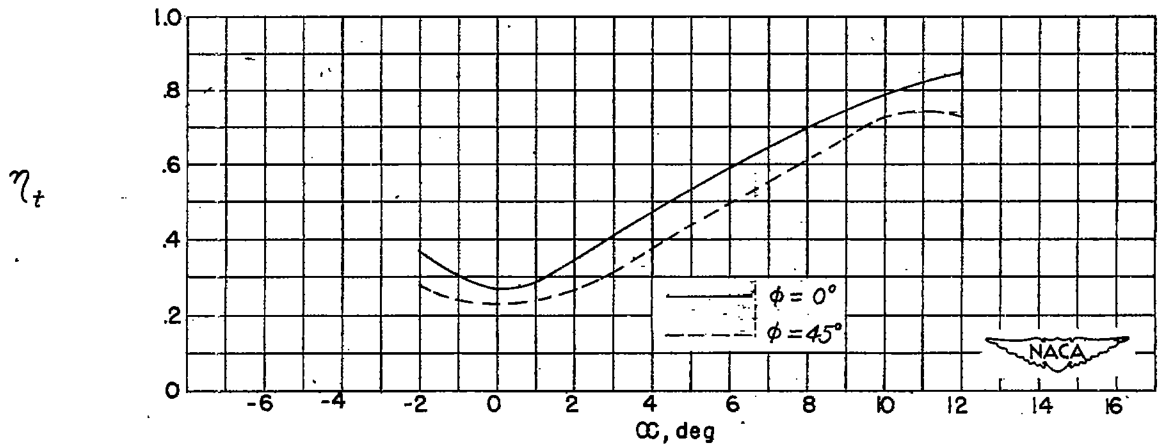

(2) Tail-lift efficiency factor variation for $BW_{2F}{}^{0}T_2$.

(a) $BW_{2F}{}^{0}T_2$.

Figure 22.- Center-of-pressure characteristics and body-wing-tail interference factors for configurations having W_2 and T_2.

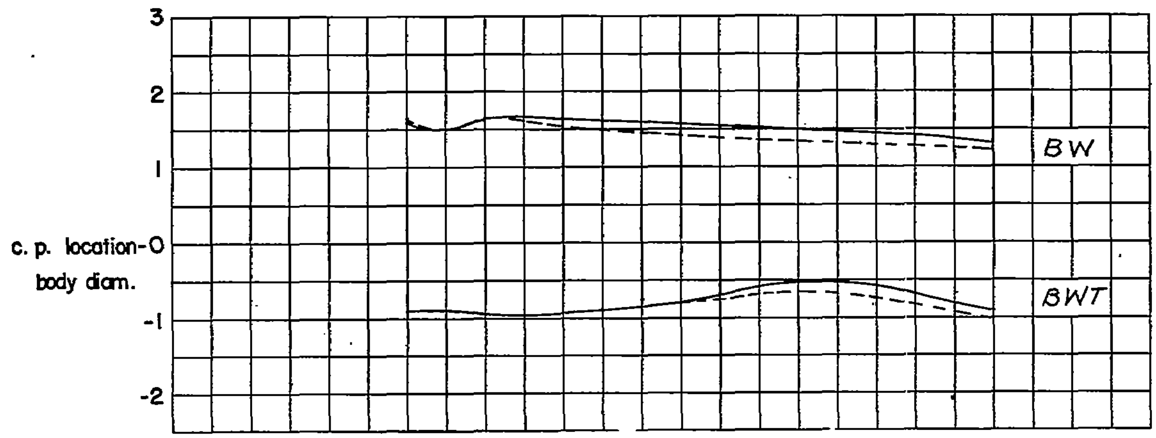

(1) Center-of-pressure variation for $BW_{2F}^{45}T_2$ and BW_{2F}.

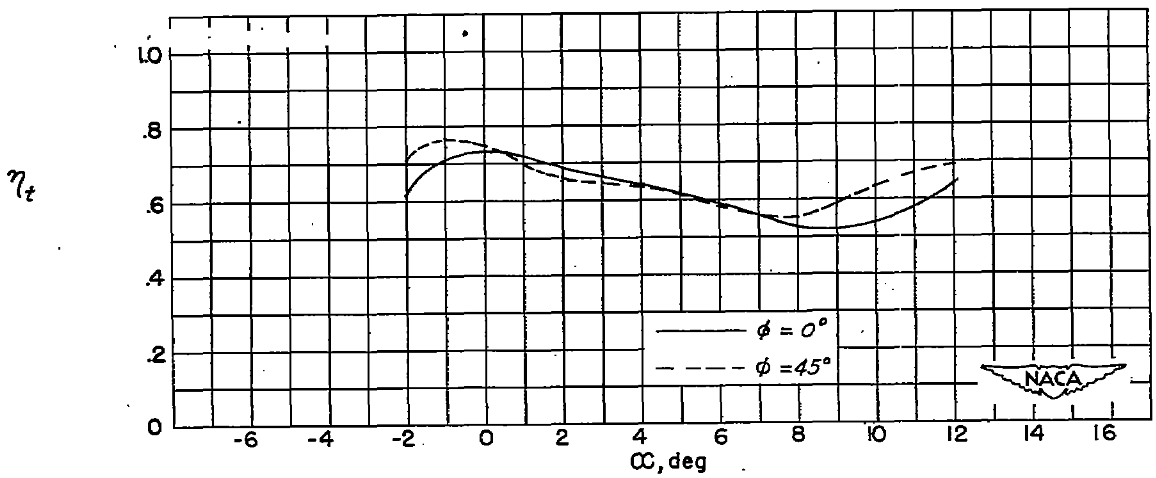

(2) Tail-lift efficiency factor variation for $BW_{2F}^{45}T_2$.

(b) $BW_{2F}^{45}T_2$.

Figure 22.- Continued.

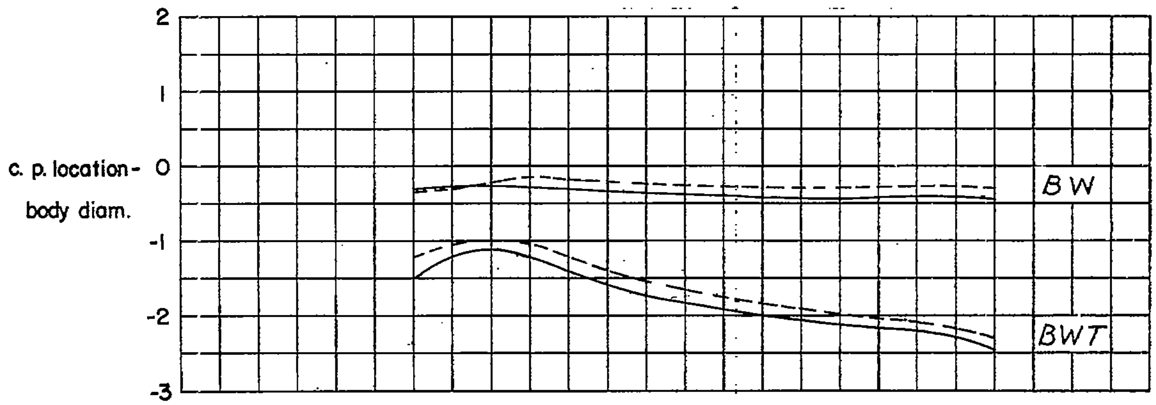

(1) Center-of-pressure variation for $BW_{2R}{}^{0}T_2$ and BW_{2R}.

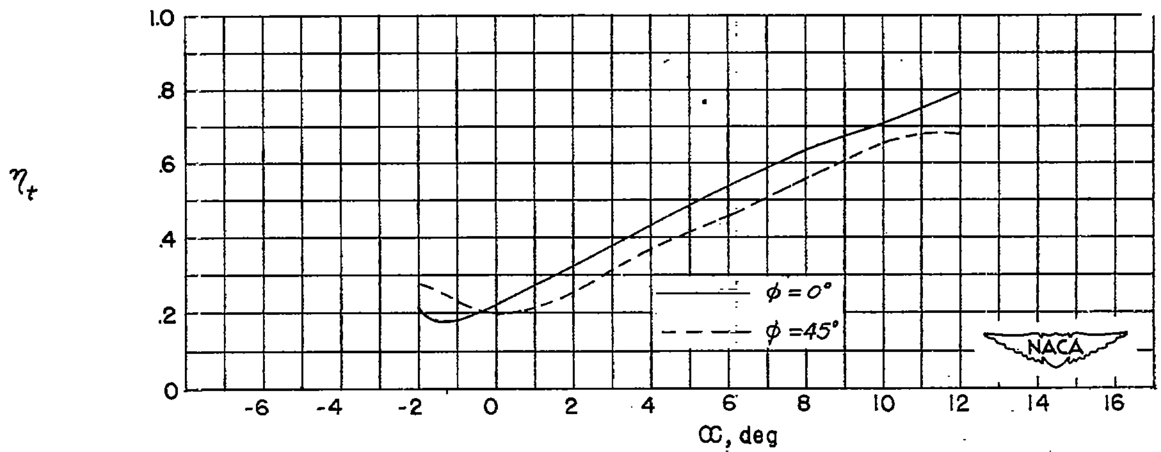

(2) Tail-lift efficiency factor variation for $BW_{2R}{}^{0}T_2$.

(c) $BW_{2R}{}^{0}T_2$.

Figure 22.- Continued.

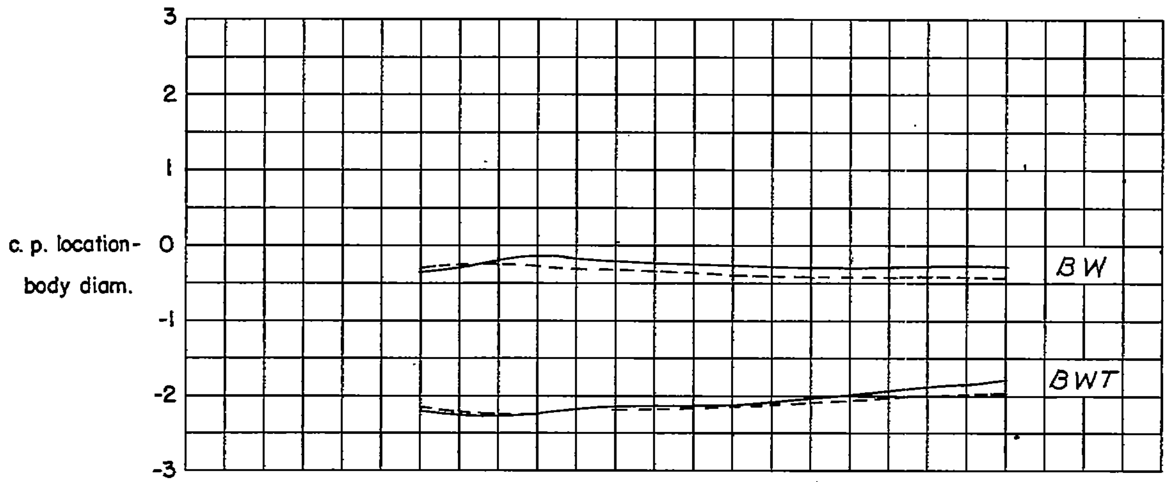

(1) Center-of-pressure variation for $BW_{2R}{}^{45}T_2$ and BW_{2R}.

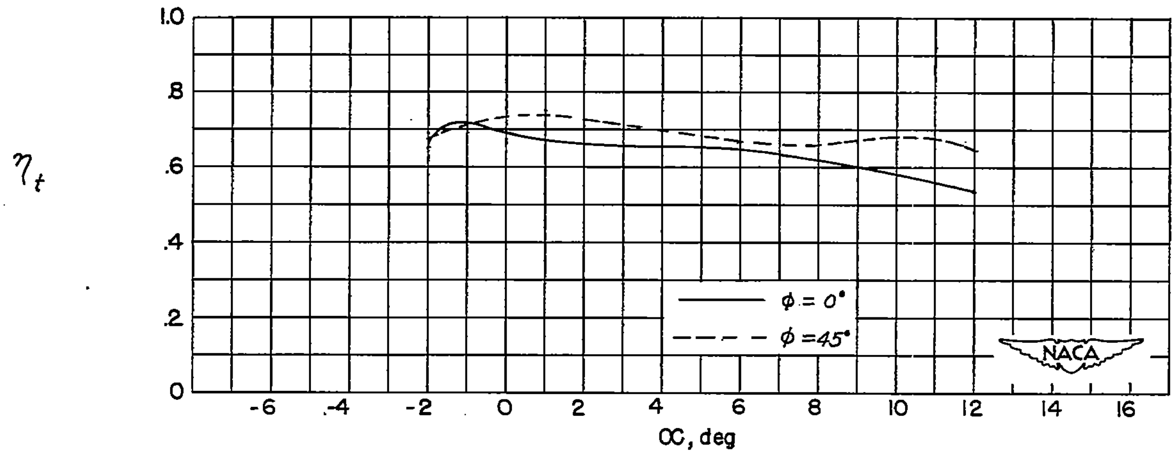

(2) Tail-lift efficiency factor variation for $BW_{2R}{}^{45}T_2$.

(d) $BW_{2R}{}^{45}T_2$.

Figure 22.- Concluded.

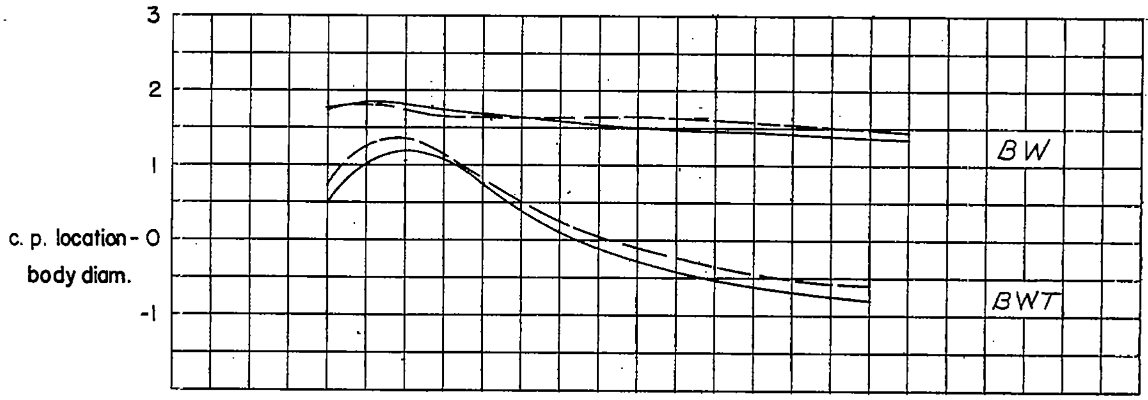

(1) Center-of-pressure variation for $BW_{3F}{}^{0}T_2$ and BW_{3F}.

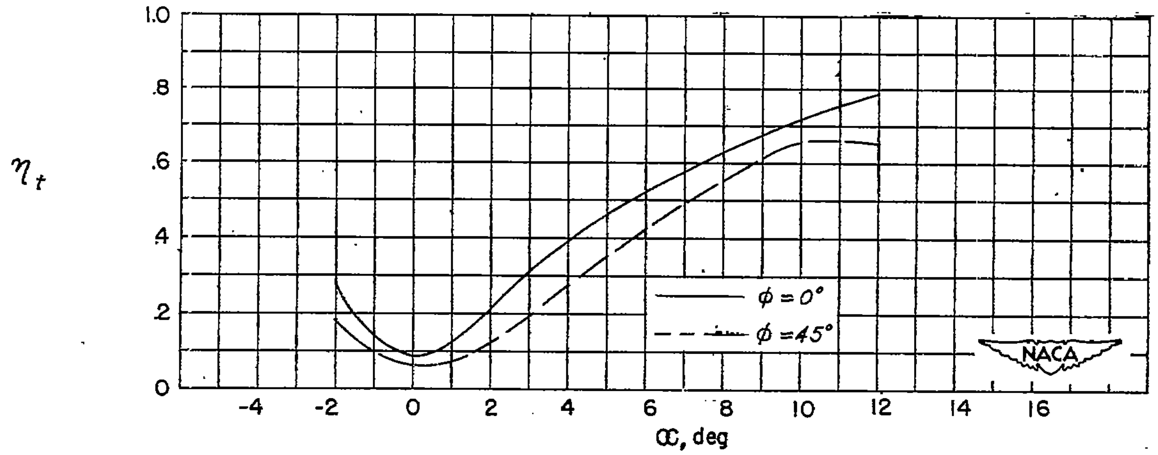

(2) Tail-lift efficiency factor variation for $BW_{3F}{}^{0}T_2$.

(a) $BW_{3F}{}^{0}T_2$.

Figure 23.- Center-of-pressure characteristics and body-wing-tail interference factors for configurations having W_3 and T_2.

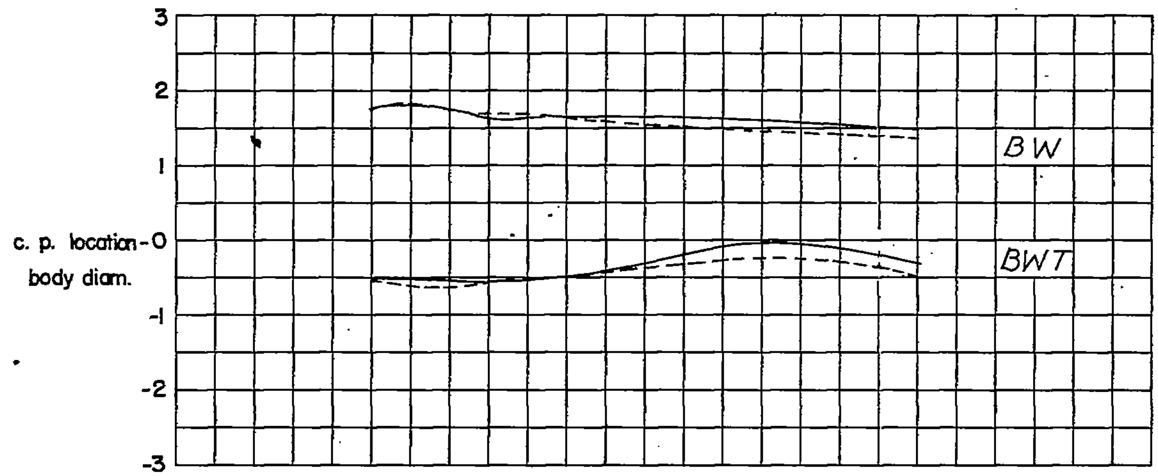

(1) Center-of-pressure variation for $BW_{3F}{}^{45}T_2$ and BW_{3F}.

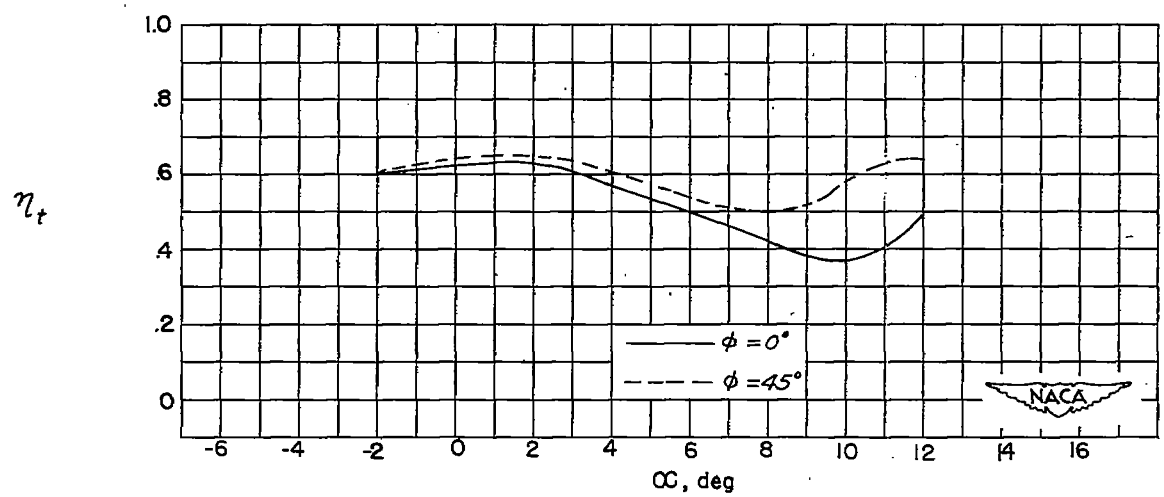

(2) Tail-lift efficiency factor variation for $BW_{3F}{}^{45}T_2$.

(b) $BW_{3F}{}^{45}T_2$.

Figure 23.- Continued.

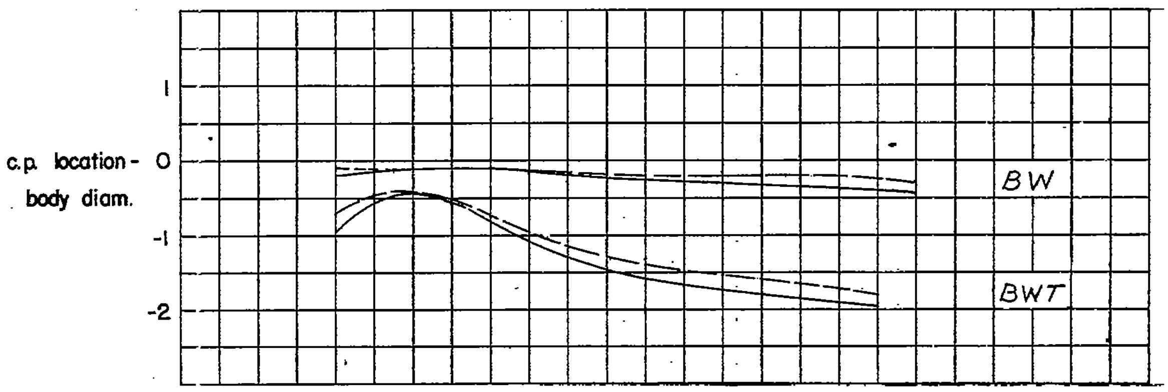

(1) Center-of-pressure variation for $BW_{3R}{}^{O}T_2$ and BW_{3R}.

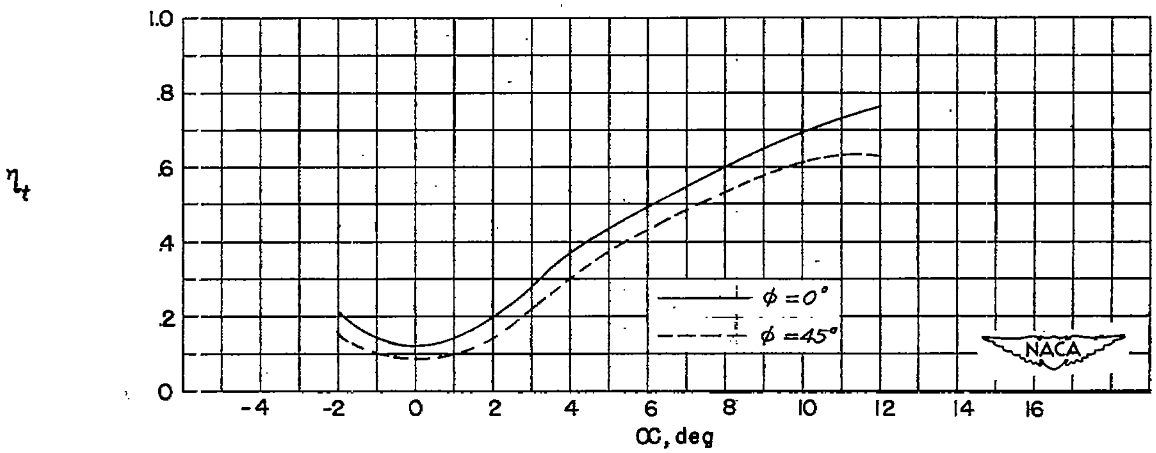

(2) Tail-lift efficiency factor variation for $BW_{3R}{}^{O}T_2$.

(c) $BW_{3R}{}^{O}T_2$.

Figure 23.- Continued.

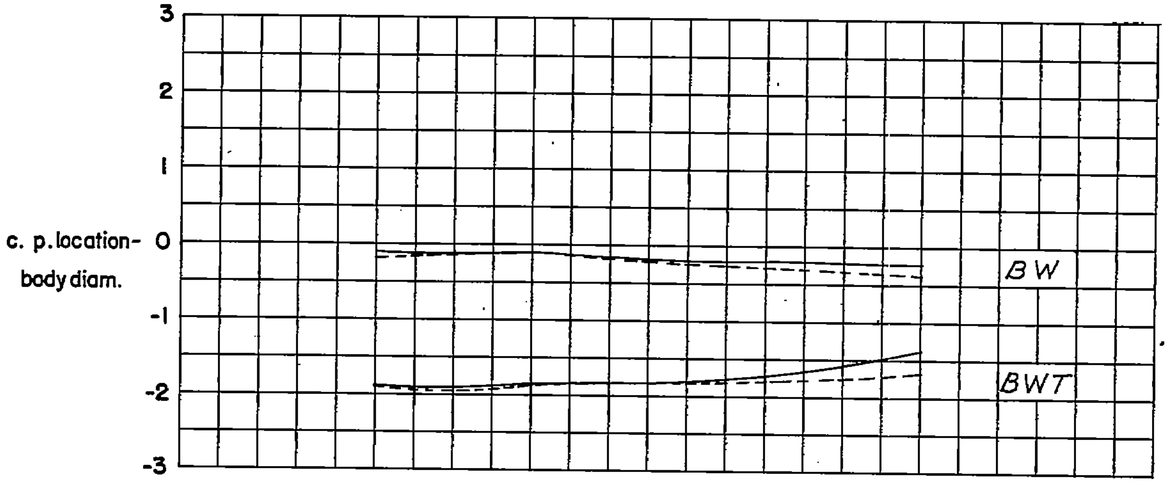

(1) Center-of-pressure variation for $BW_{3R}{}^{45}T_2$ and BW_{3R}.

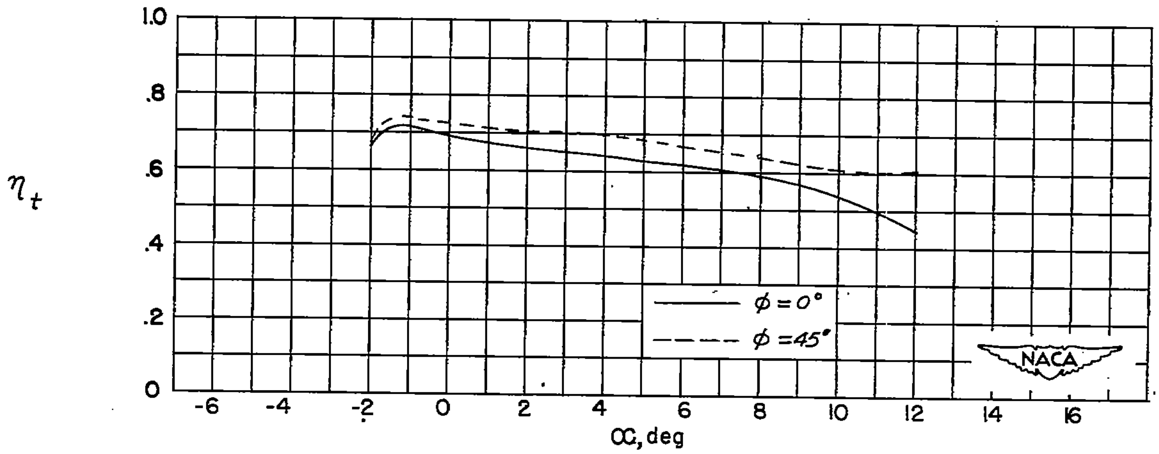

(2) Tail-lift efficiency factor variation for $BW_{3R}{}^{45}T_2$.

(d) $BW_{3R}{}^{45}T_2$.

Figure 23.- Concluded.

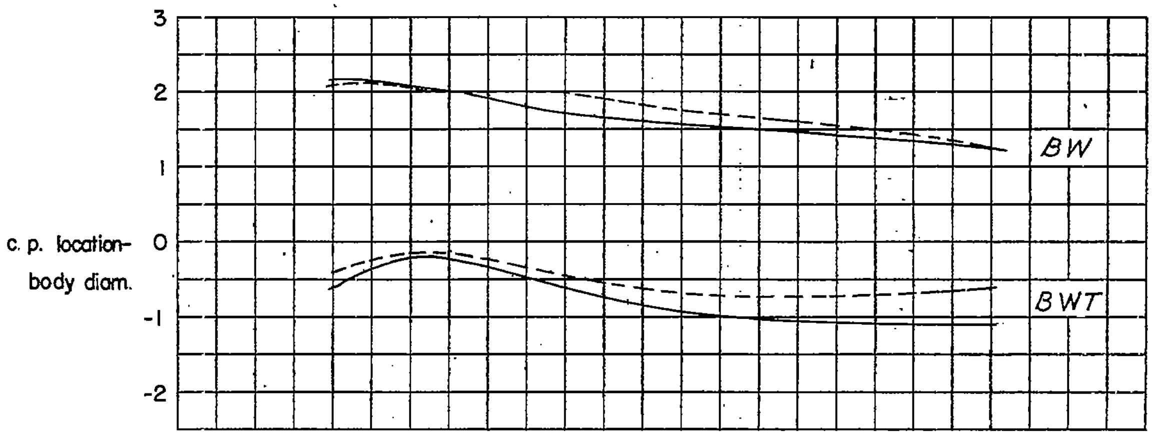

(1) Center-of-pressure variation for $BW_{4F}{}^{O}T_4$ and BW_{4F}.

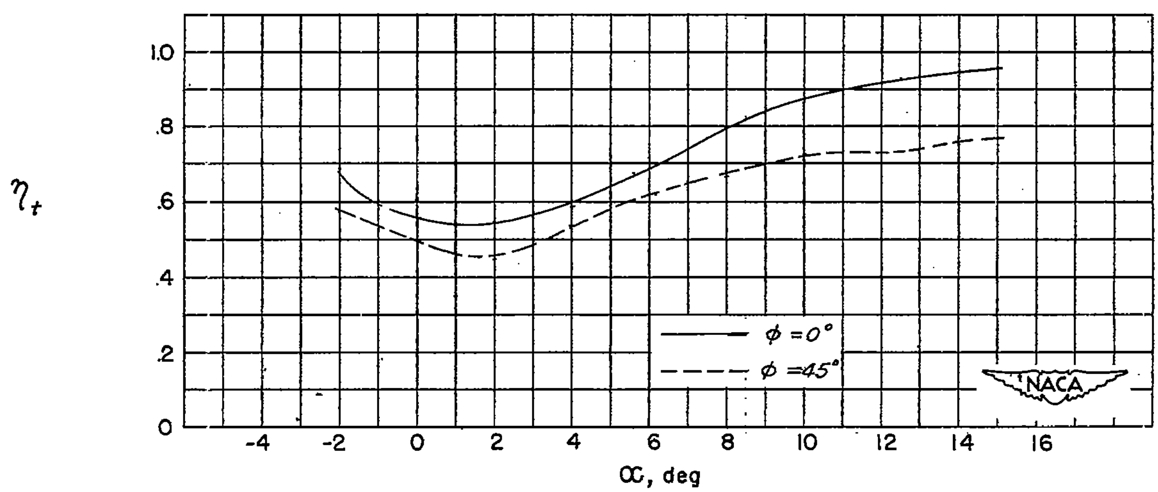

(2) Tail-lift efficiency factor variation for $BW_{4F}{}^{O}T_4$.

(a) $BW_{4F}{}^{O}T_4$.

Figure 24.- Center-of-pressure characteristics and body-wing-tail interference factors for configurations having W_4 and T_4.

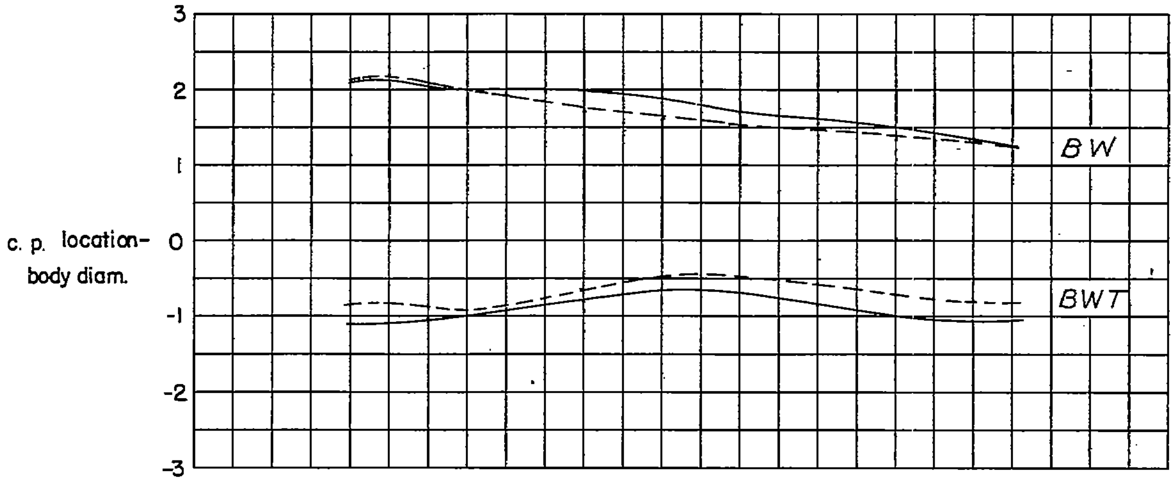

(1) Center-of-pressure variation for $BW_{4F}{}^{45}T_4$ and BW_{4F}.

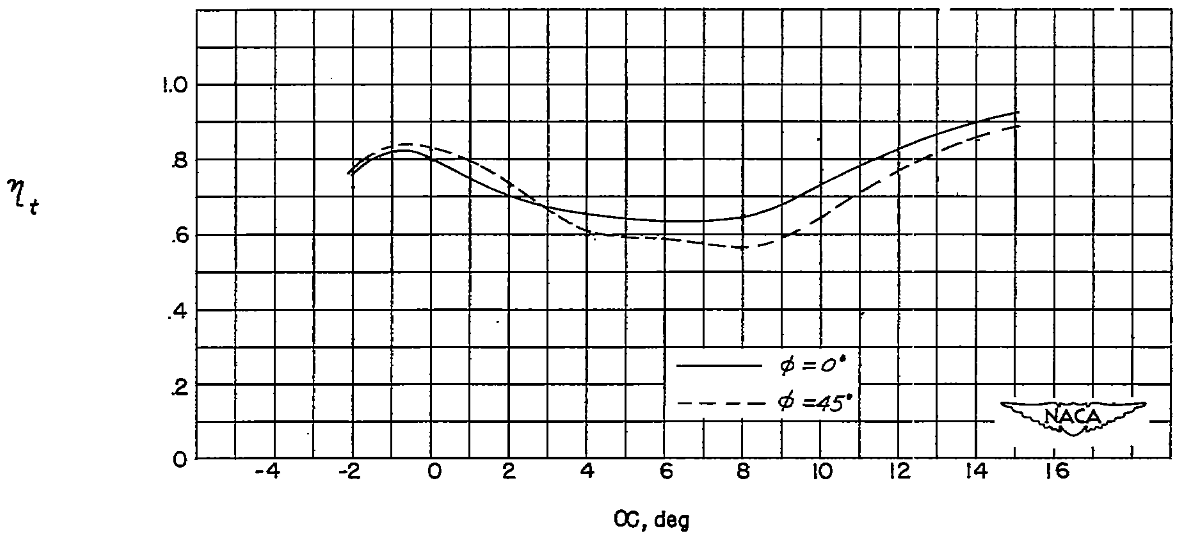

(2) Tail-lift efficiency factor variation for $BW_{4F}{}^{45}T_4$.

(b) $BW_{4F}{}^{45}T_4$.

Figure 24.- Continued.

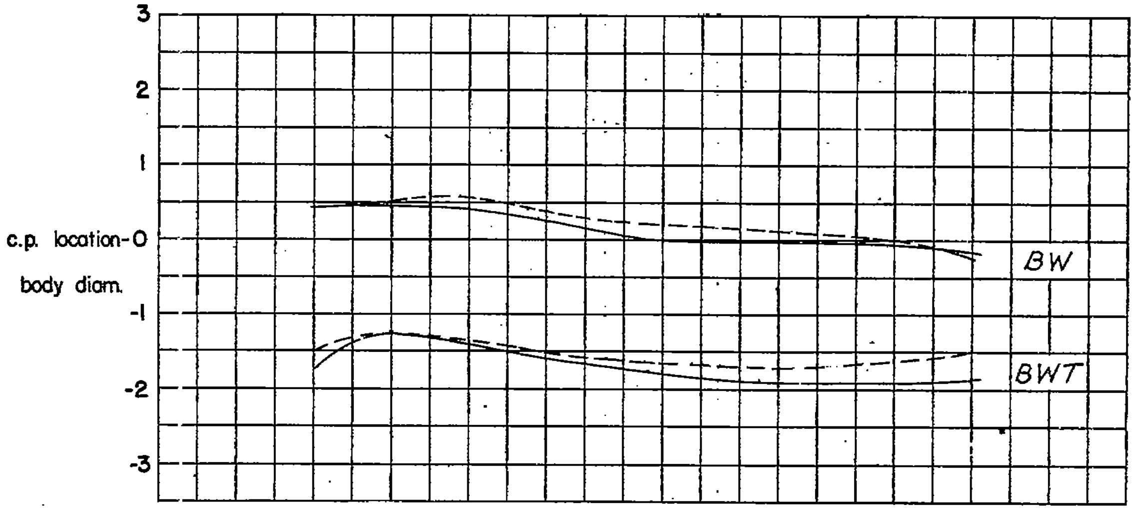

(1) Center-of-pressure variation for $BW_{4R}{}^{O}T_4$ and BW_{4R}.

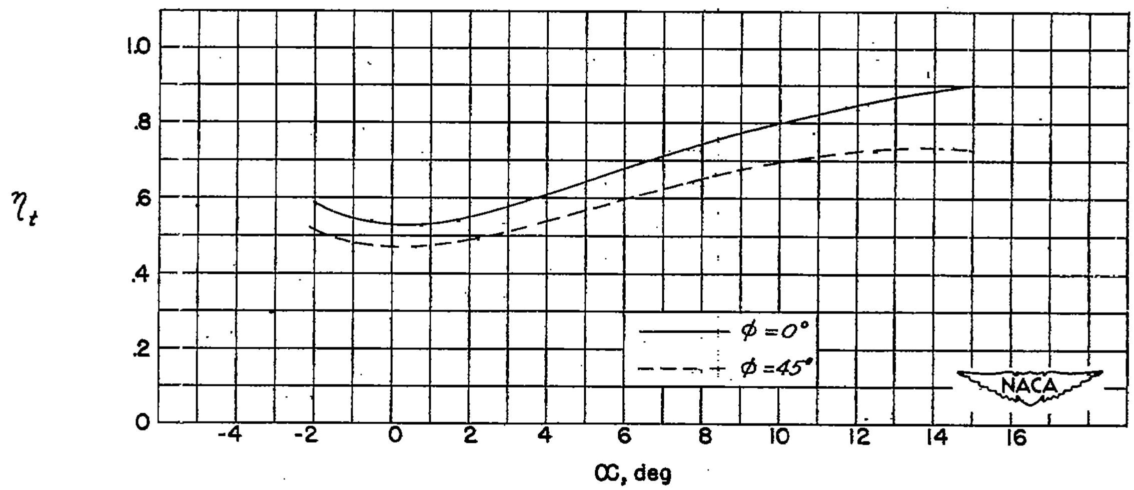

(2) Tail-lift efficiency factor variation for $BW_{4R}{}^{O}T_4$.

(c) $BW_{4R}{}^{O}T_4$.

Figure 24.- Continued.

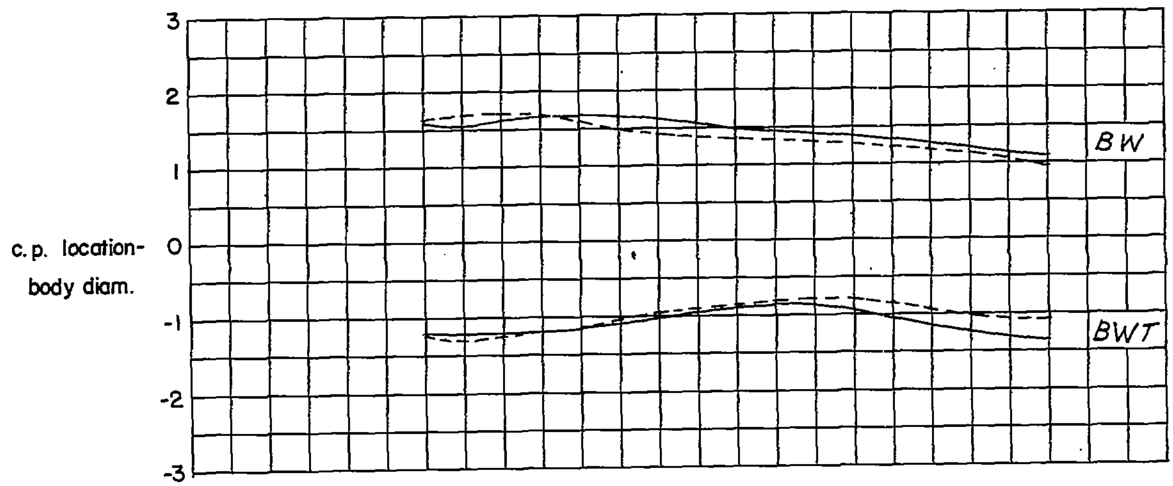

(1) Center-of-pressure variation for $BW_{5F}{}^{45}T_4$ and BW_{5F}.

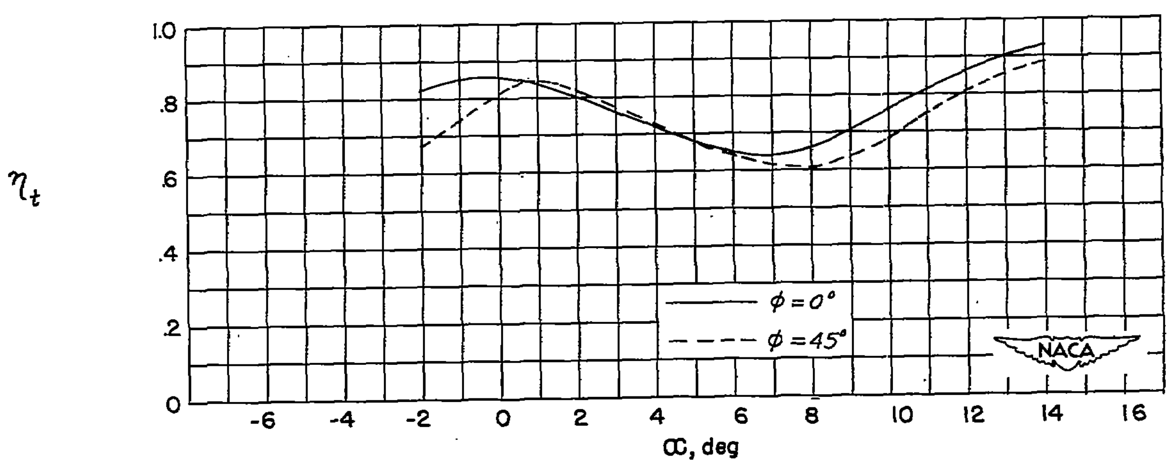

(2) Tail-lift efficiency factor variation for $BW_{5F}{}^{45}T_4$.

(b) $BW_{5F}{}^{45}T_4$.

Figure 25.- Continued.

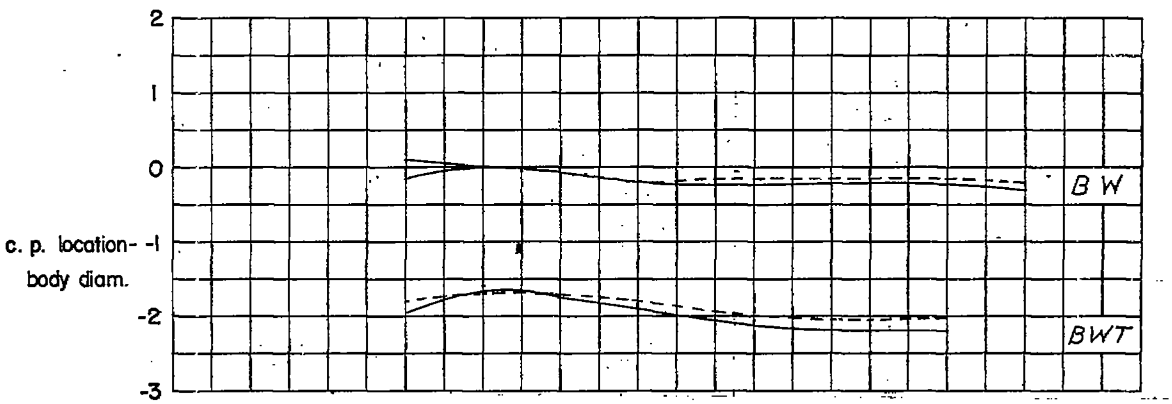

(1) Center-of-pressure variation for $BW_{5R}{}^{O}T_4$ and BW_{5R}.

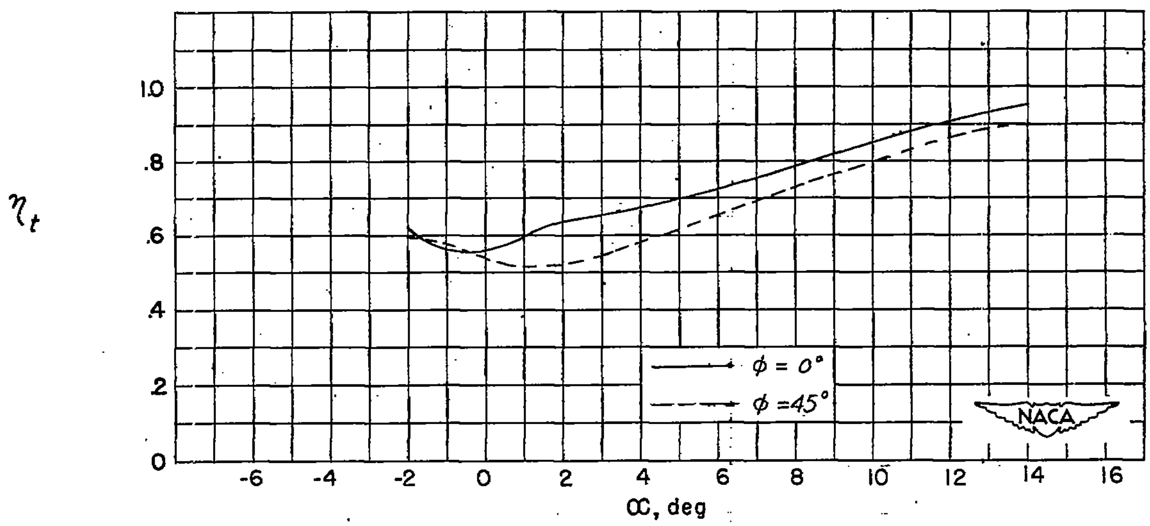

(2) Tail-lift efficiency factor variation for $BW_{5R}{}^{O}T_4$.

(c) $BW_{5R}{}^{O}T_4$.

Figure 25.- Continued.

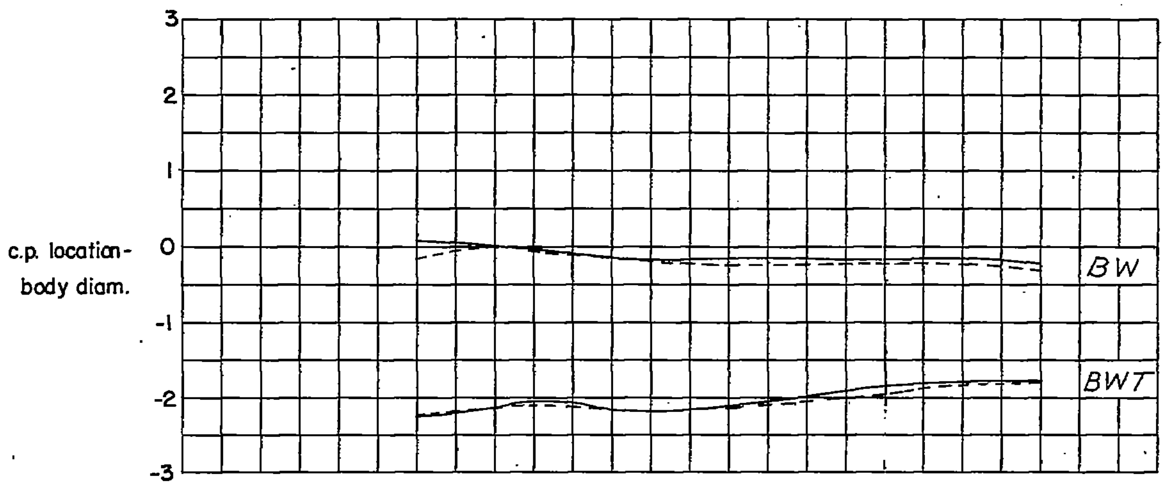

(1) Center-of-pressure variation for $BW_{5R}^{45}T_4$ and BW_{5R}.

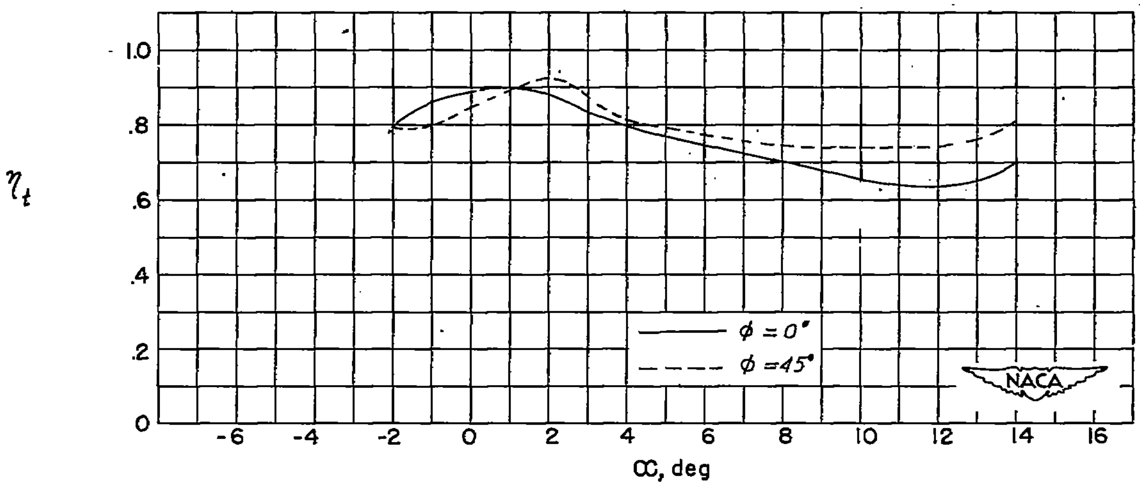

(2) Tail-lift efficiency factor variation for $BW_{5R}^{45}T_4$.

(d) $BW_{5R}^{45}T_4$.

Figure 25.- Concluded.

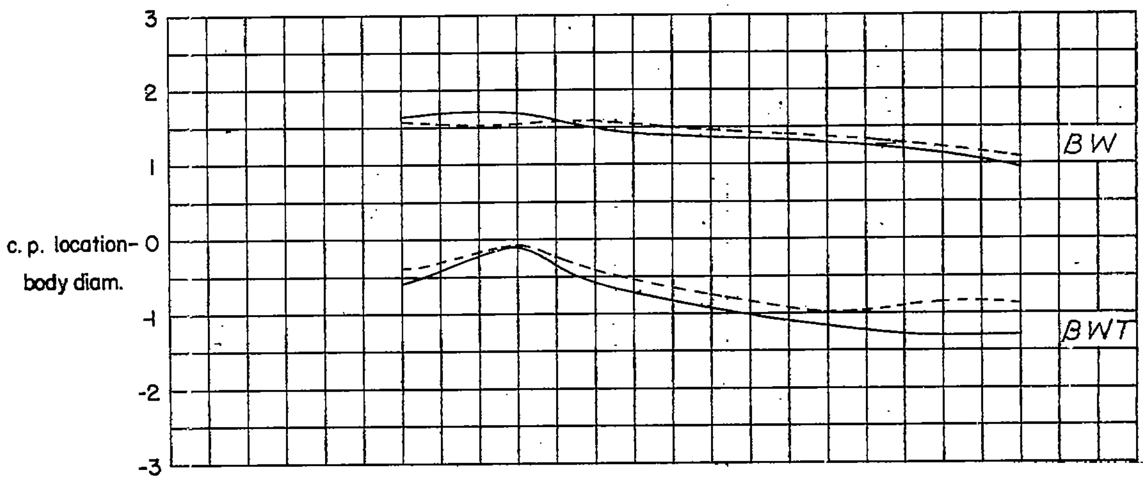

(1) Center-of-pressure variation for $BW_{5F}{}^{O}T_5$ and BW_{5F}.

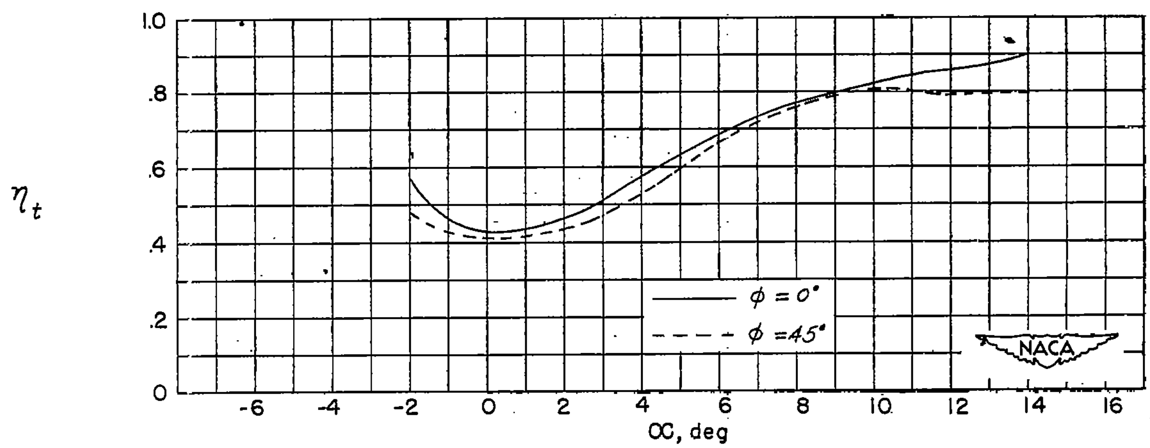

(2) Tail-lift efficiency factor variation for $BW_{5F}{}^{O}T_5$.

(a) $BW_{5F}{}^{O}T_5$.

Figure 26.- Center-of-pressure characteristics and body-wing-tail interference factors for configurations having W_5 and T_5.

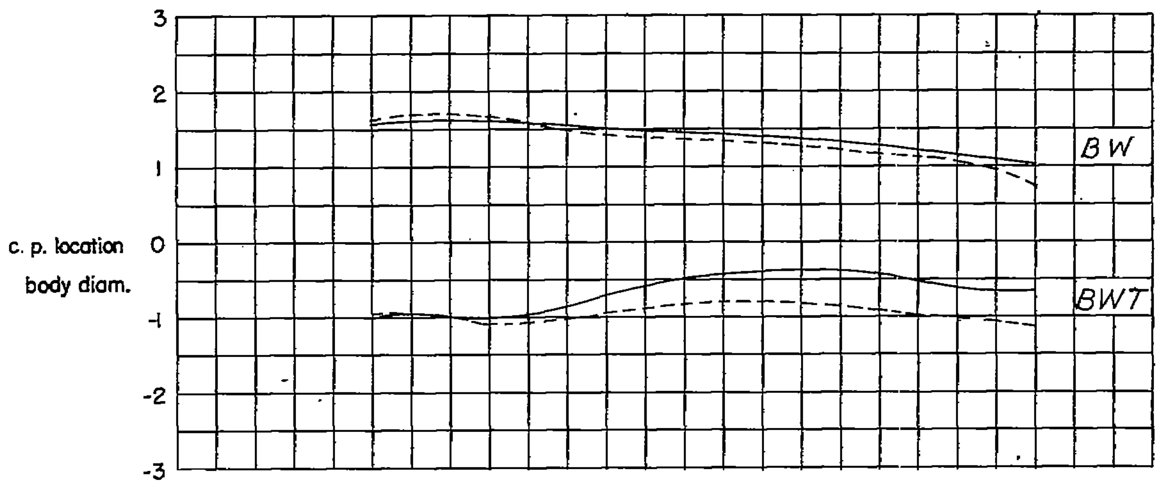

(1) Center-of-pressure variation for $BW_{5F}{}^{45}T_5$ and BW_{5F}.

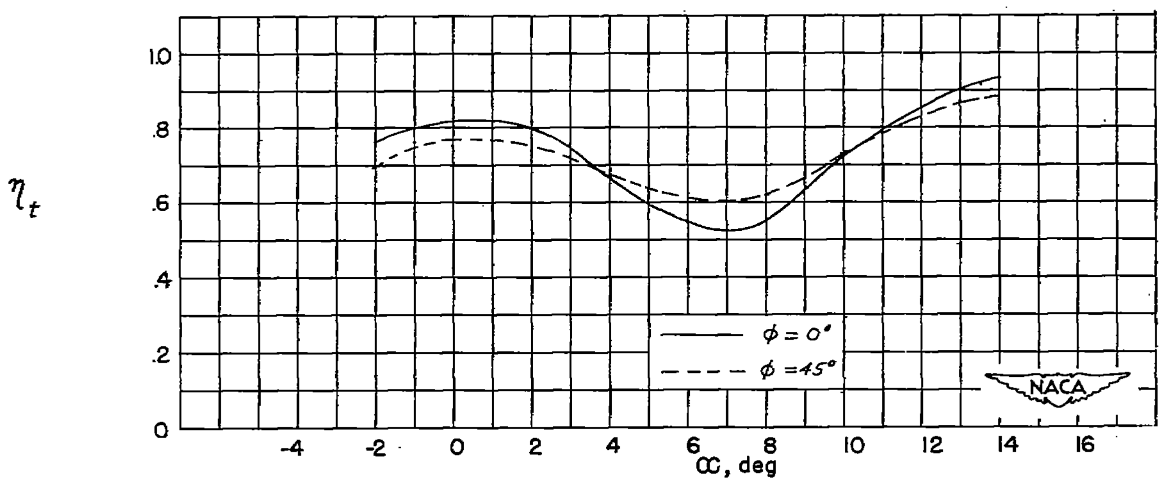

(2) Tail-lift efficiency factor variation for $BW_{5F}{}^{45}T_5$.

(b) $BW_{5F}{}^{45}T_5$.

Figure 26.- Continued.

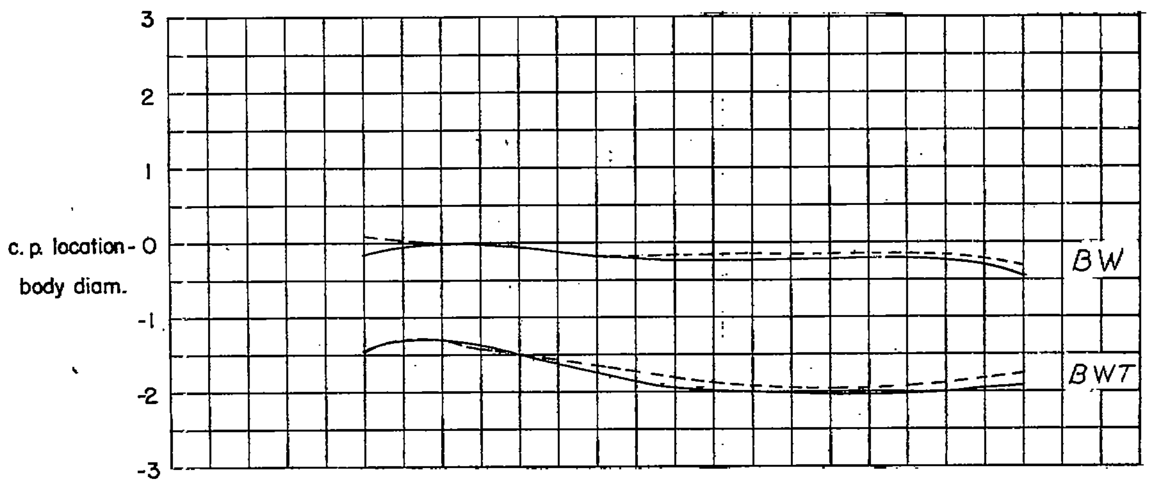

(1) Center-of-pressure variation for $BW_{5R}{}^{0}T_{5}$ and BW_{5R}.

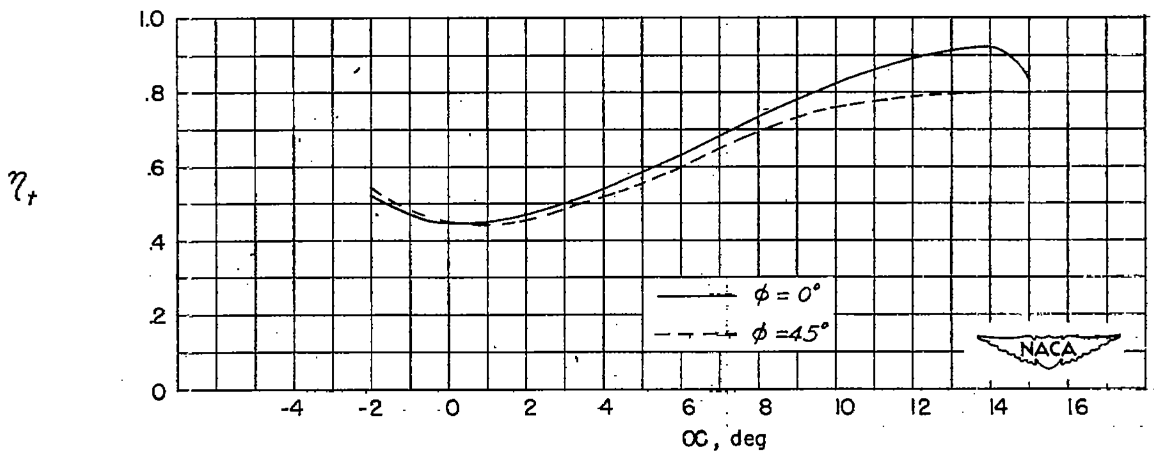

(2) Tail-lift efficiency factor variation for $BW_{5R}{}^{0}T_{5}$.

(c) $BW_{5R}{}^{0}T_{5}$.

Figure 26.- Continued.

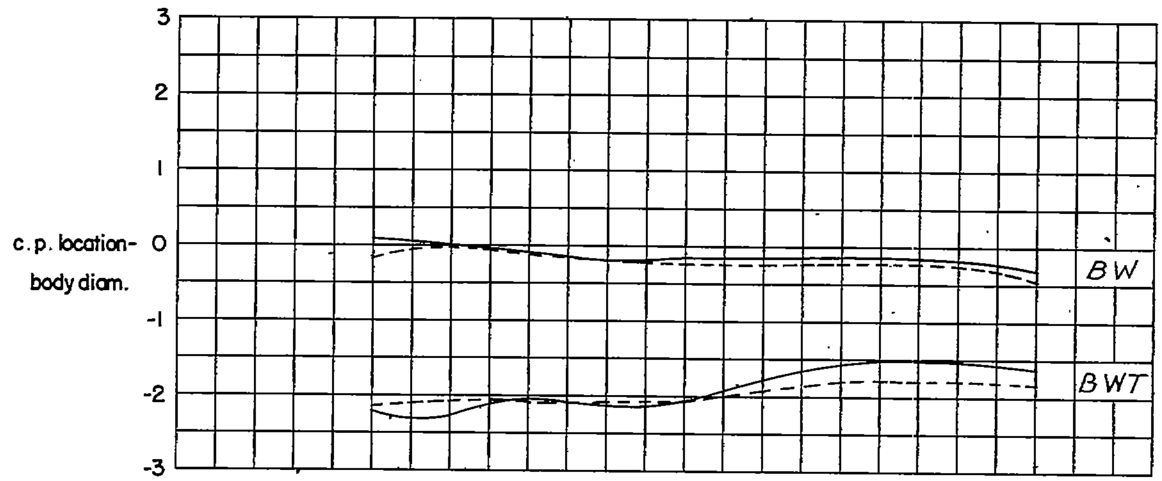

(1) Center-of-pressure variation for $BW_{5R}{}^{45}T_5$ and BW_{5R}.

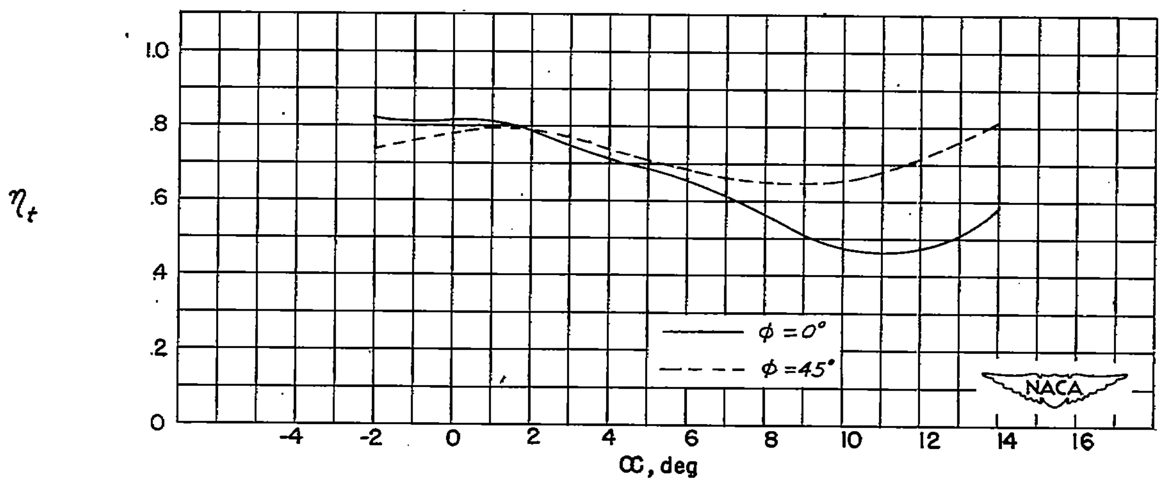

(2) Tail-lift efficiency factor variation for $BW_{5R}{}^{45}T_5$.

(d) $BW_{5R}{}^{45}T_5$.

Figure 26.- Concluded.

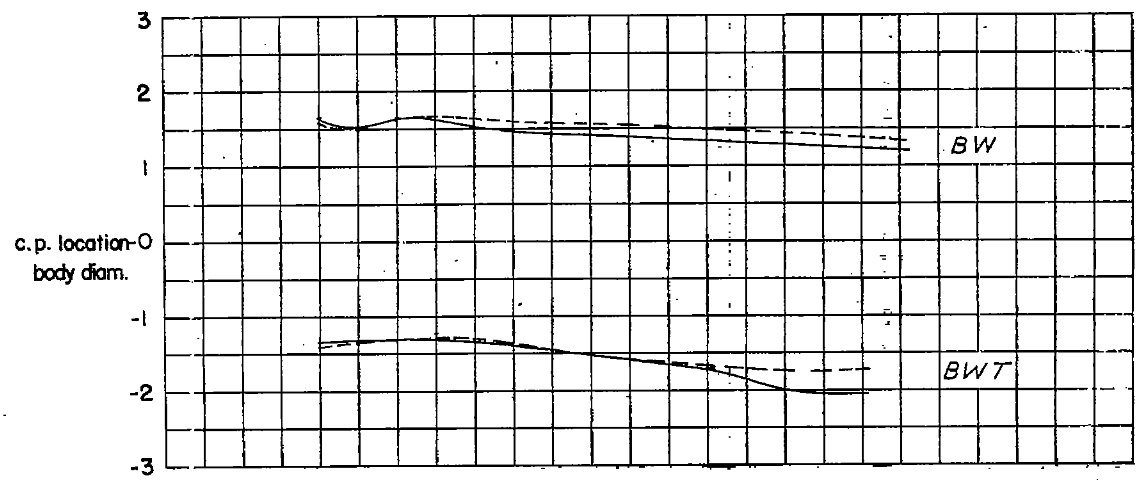

(1) Center-of-pressure variation for $BW_{2F}{}^{0}T_3$ and BW_{2F}.

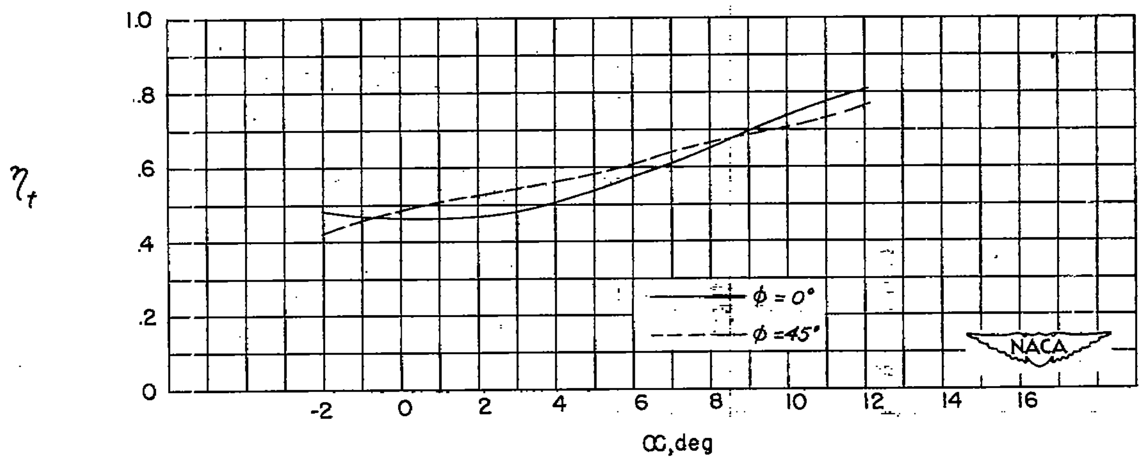

(2) Tail-lift efficiency factor variation for $BW_{2F}{}^{0}T_3$.

(a) $BW_{2F}{}^{0}T_3$.

Figure 27.- Center-of-pressure characteristics and body-wing-tail interference factors for configurations having W_2 and T_3.

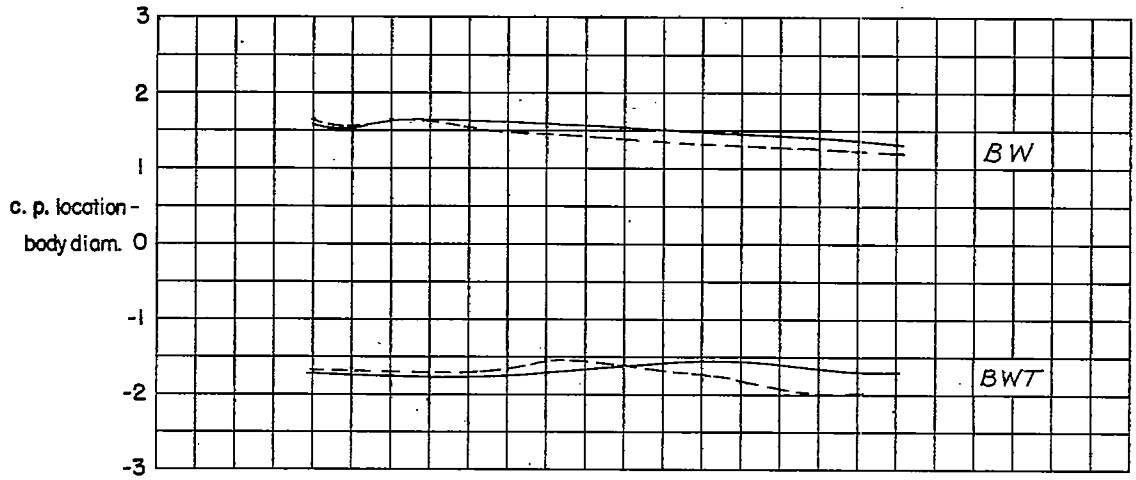

(1) Center-of-pressure variation for $BW_{2F}{}^{45}T_3$ and BW_{2F}.

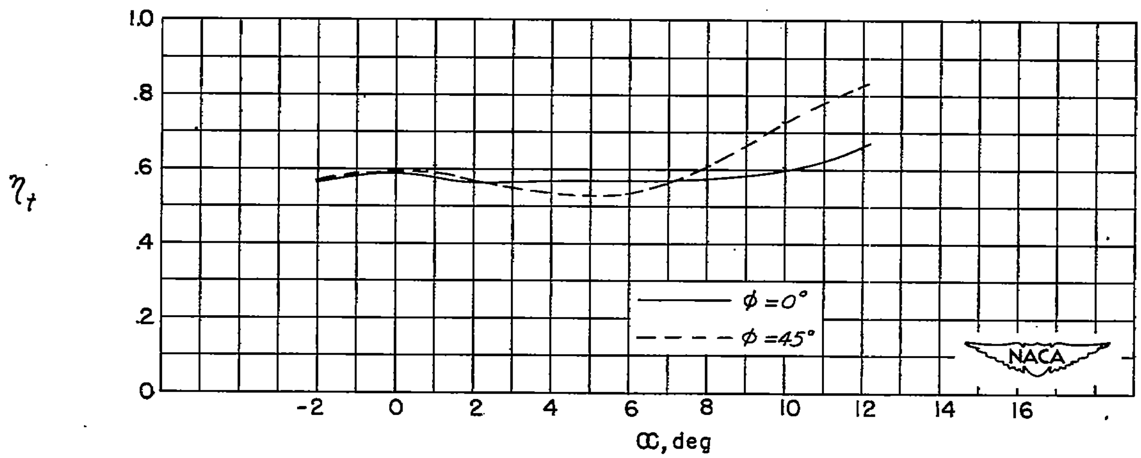

(2) Tail-lift efficiency factor variation for $BW_{2F}{}^{45}T_3$.

(b) $BW_{2F}{}^{45}T_3$.

Figure 27.- Continued.

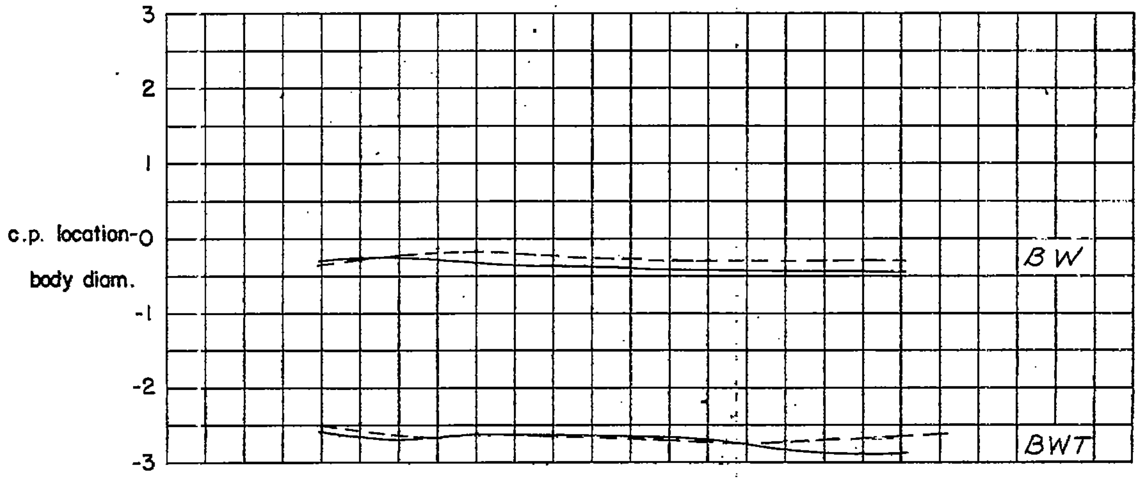

(1) Center-of-pressure variation for $BW_{2R}{}^{0}T_3$ and BW_{2R}.

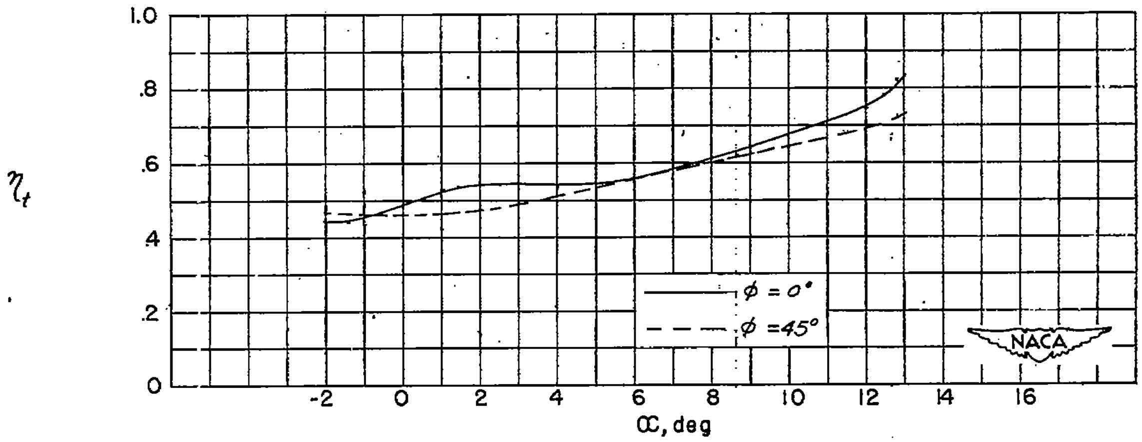

(2) Tail-lift efficiency factor variation for $BW_{2R}{}^{0}T_3$.

(c) $BW_{2R}{}^{0}T_3$.

Figure 27.- Continued.

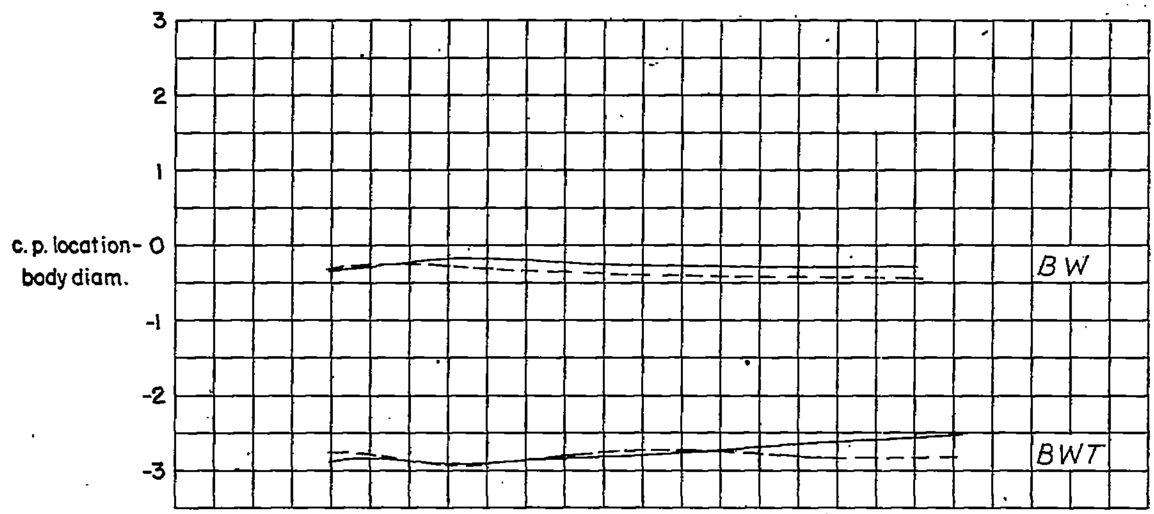

(1) Center-of-pressure variation for $BW_{2R}{}^{45}T_3$ and BW_{2R}.

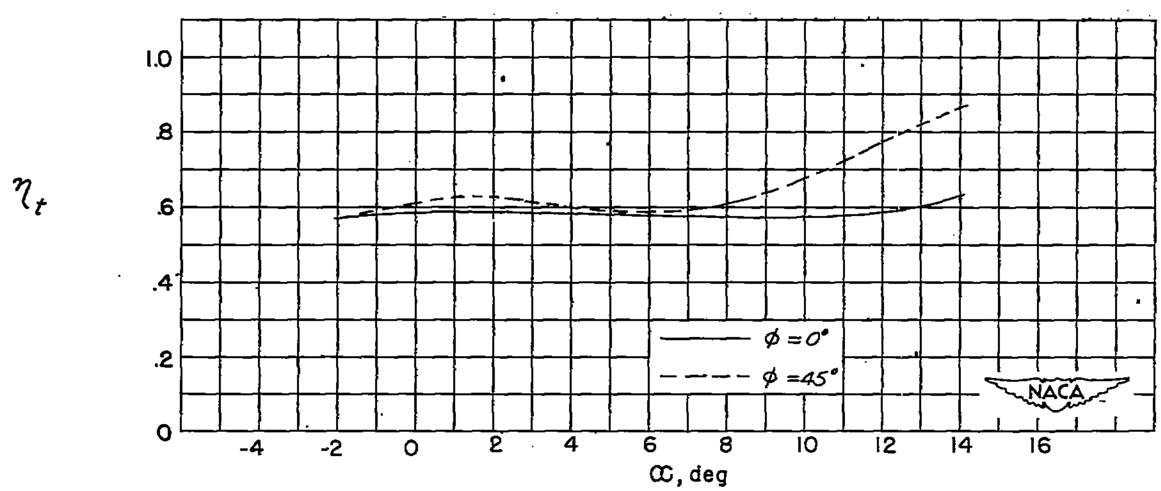

(2) Tail-lift efficiency factor variation for $BW_{2R}{}^{45}T_3$.

(d) $BW_{2R}{}^{45}T_3$.

Figure 27.- Concluded.

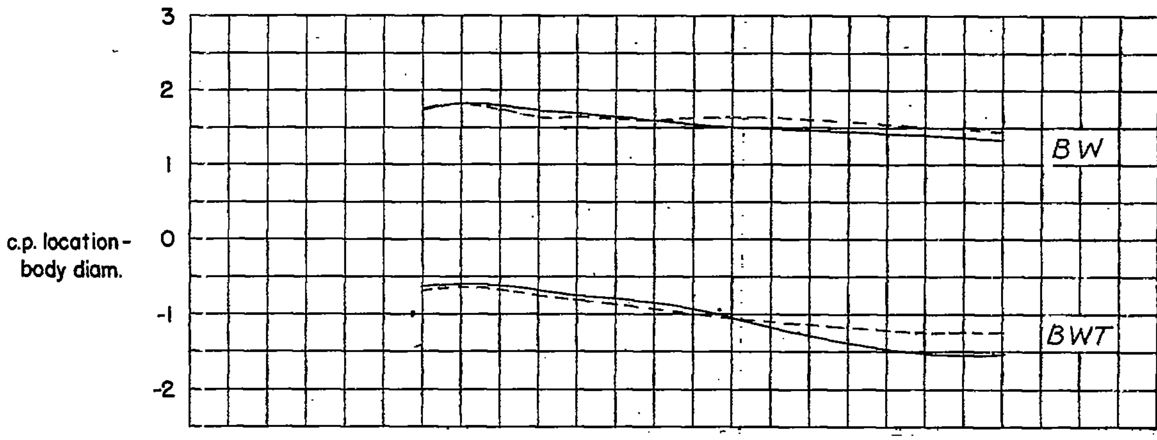

(1) Center-of-pressure variation for $BW_{3F}{}^{O}T_3$ and BW_{3F}.

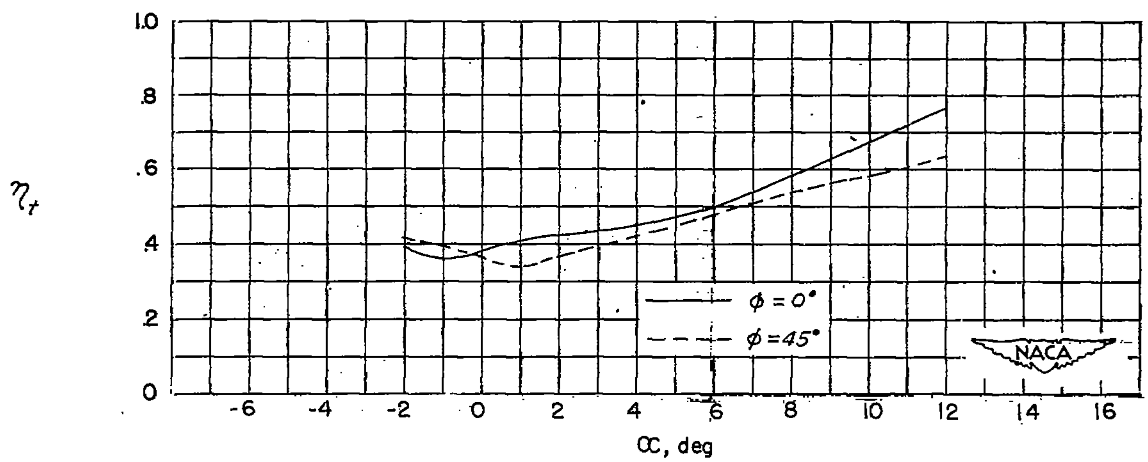

(2) Tail-lift efficiency factor variation for $BW_{3F}{}^{O}T_3$.

(a) $BW_{3F}{}^{O}T_3$.

Figure 28.- Center-of-pressure characteristics and body-wing-tail interference factors for configurations having W_3 and T_3.

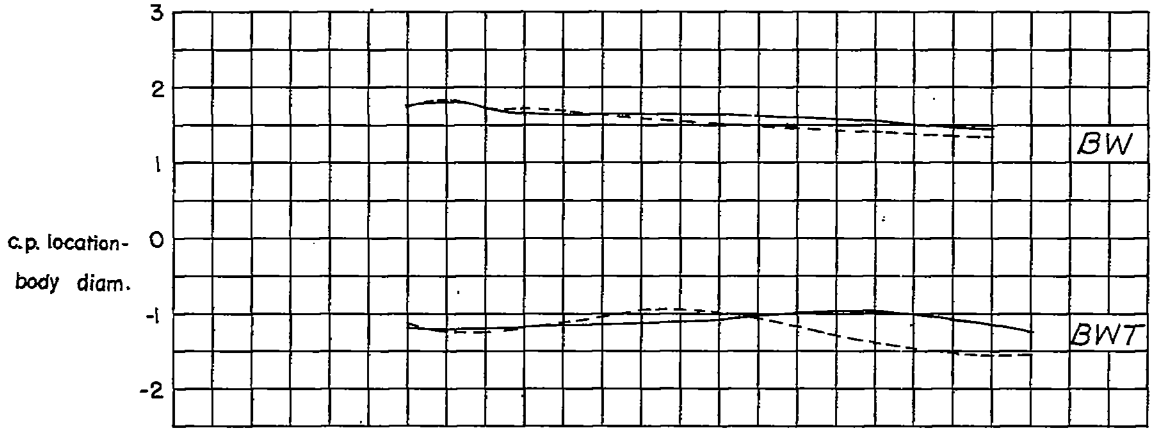

(1) Center-of-pressure variation for $BW_{3F}{}^{45}T_3$ and BW_{3F}.

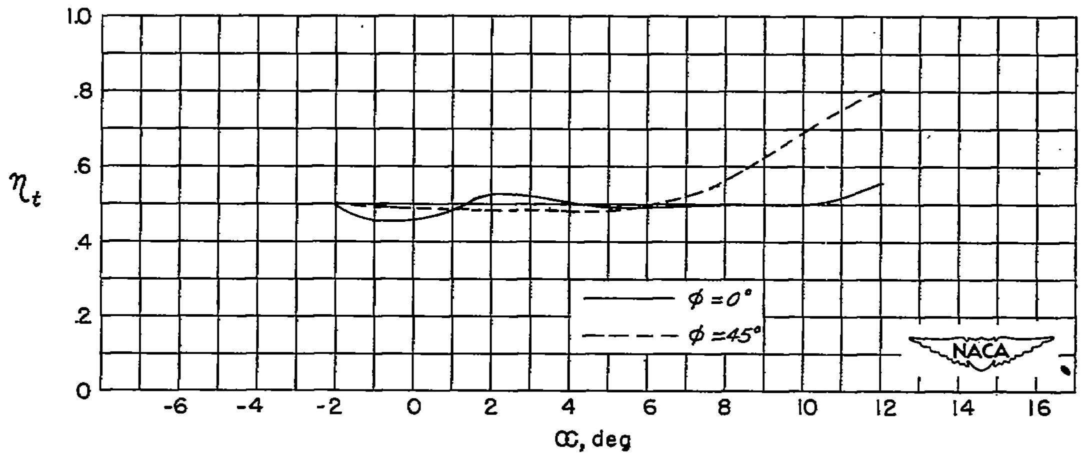

(2) Tail-lift efficiency factor variation for $BW_{3F}{}^{45}T_3$.

(b) $BW_{3F}{}^{45}T_3$.

Figure 28.- Continued.

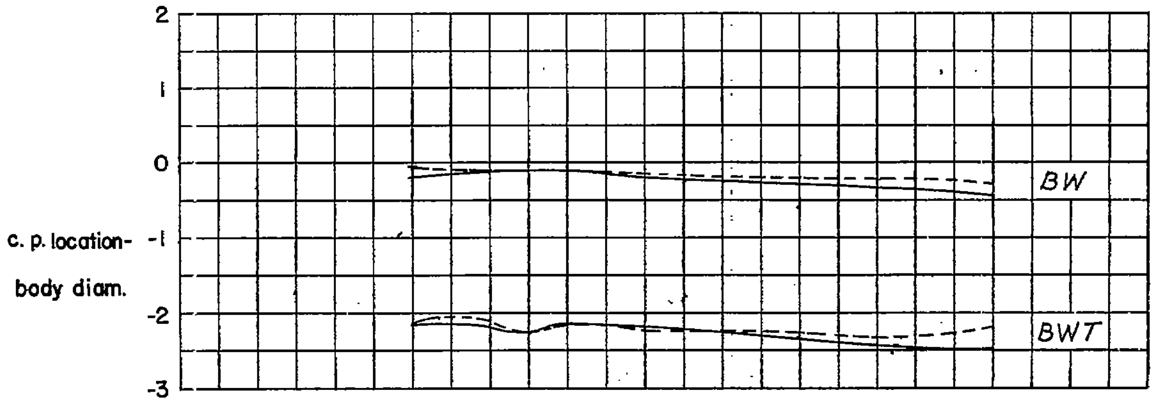

(1) Center-of-pressure variation for $BW_{3R}{}^{O}T_3$ and BW_{3R}.

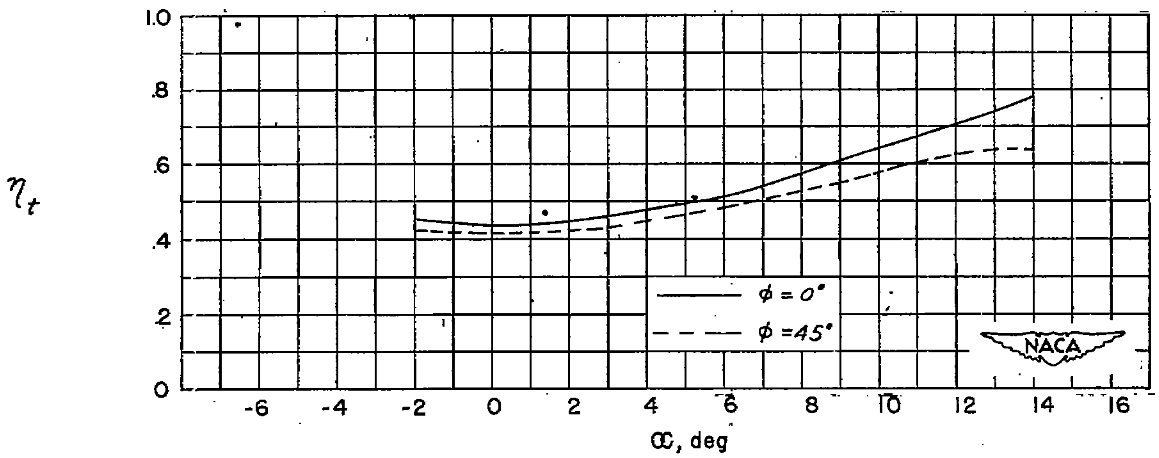

(2) Tail-lift efficiency factor variation for $BW_{3R}{}^{O}T_3$.

(c) $BW_{3R}{}^{O}T_3$.

Figure 28.- Continued.

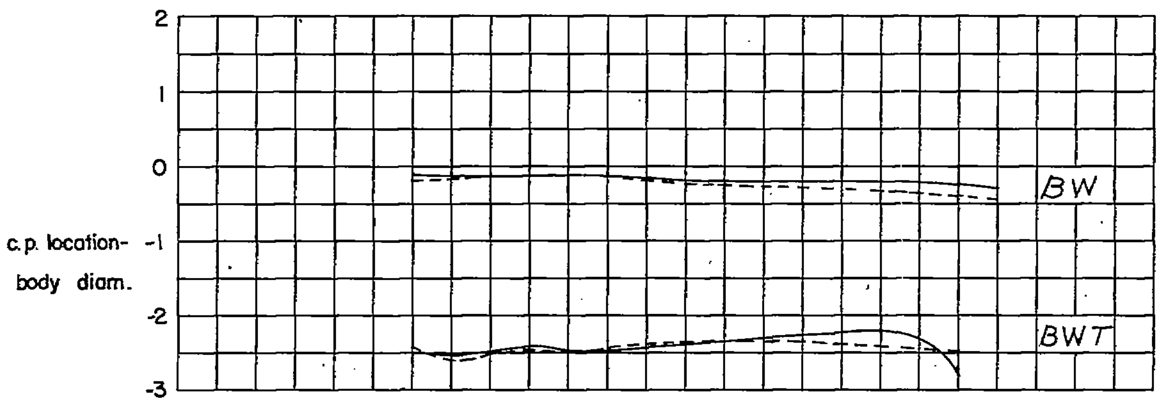

(1) Center-of-pressure variation for $BW_{3R}{}^{45}T_3$ and BW_{3R}.

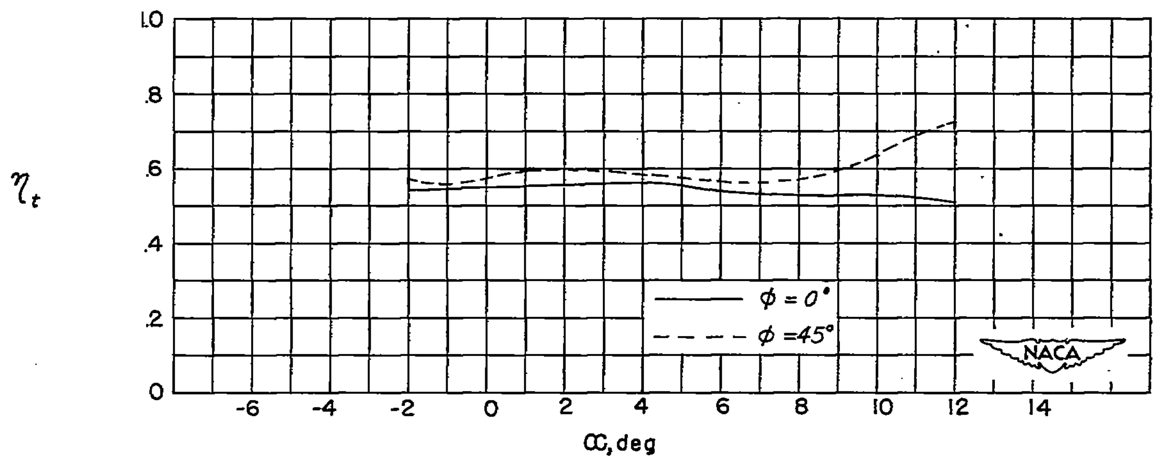

(2) Tail-lift efficiency factor variation for $BW_{3R}{}^{45}T_3$.

(d) $BW_{3R}{}^{45}T_3$.

Figure 28.- Concluded.

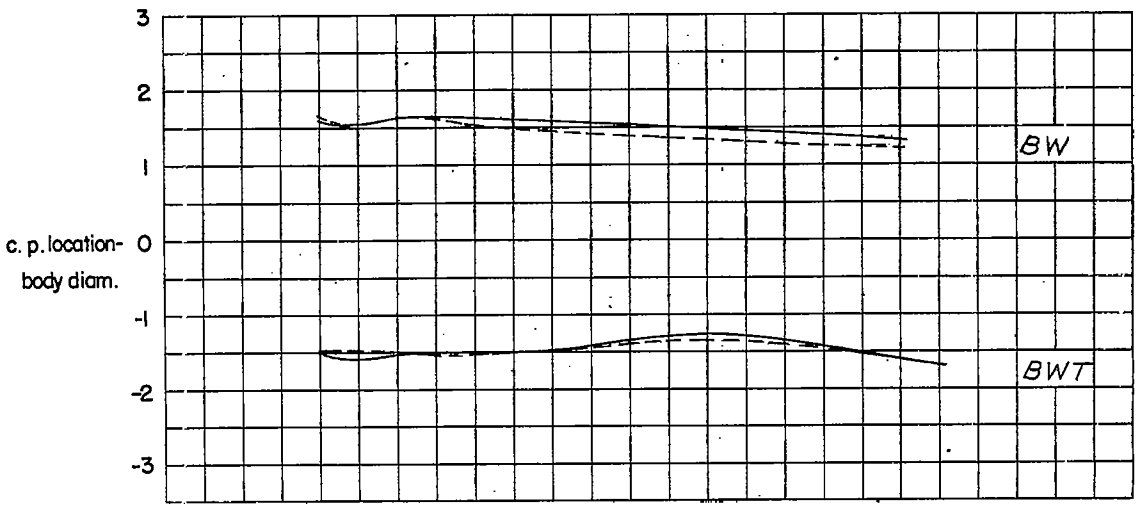

(1) Center-of-pressure variation for $BW_{2F}{}^{45}T_6$ and BW_{2F}.

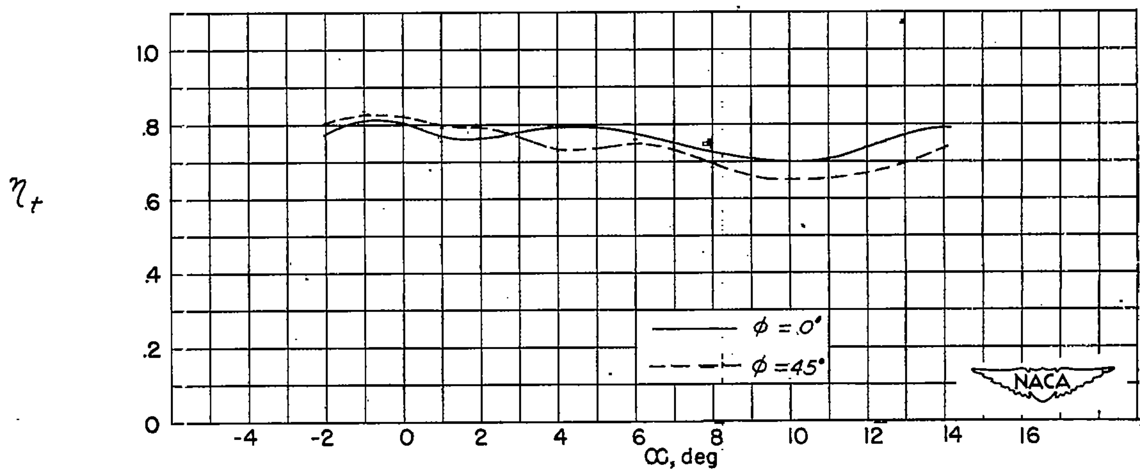

(2) Tail-lift efficiency factor variation for $BW_{2F}{}^{45}T_6$.

(a) $BW_{2F}{}^{45}T_6$.

Figure 29.- Center-of-pressure characteristics and body-wing-tail interference factors for configurations having W_2 and T_6.

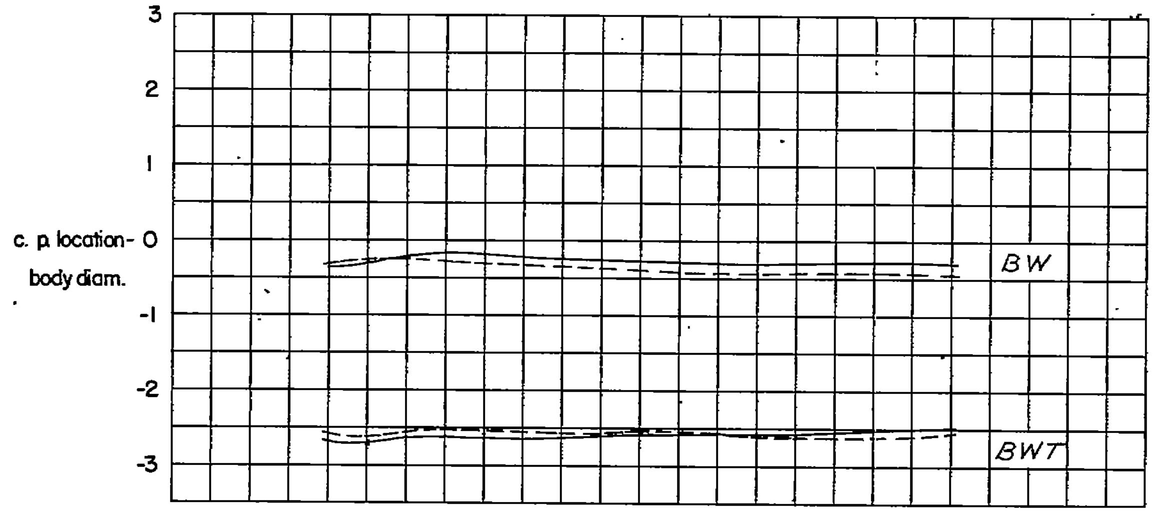

(1) Center-of-pressure variation for $BW_{2R}{}^{45}T_6$ and BW_{2R}.

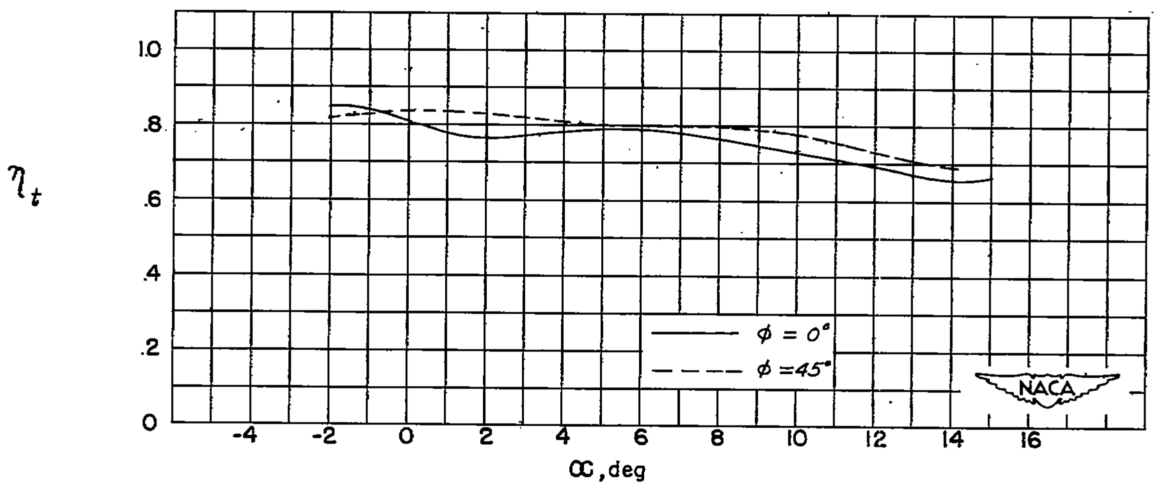

(2) Tail-lift efficiency factor variation for $BW_{2R}{}^{45}T_6$.

(b) $BW_{2R}{}^{45}T_6$.

Figure 29.- Concluded.

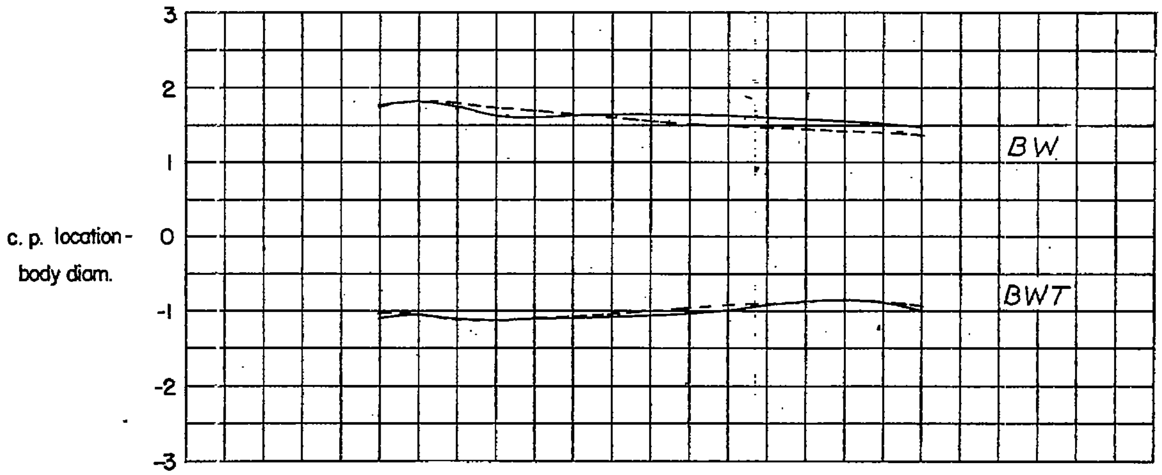

(1) Center-of-pressure variation for $BW_{3F}{}^{45}T_6$ and BW_{3F}.

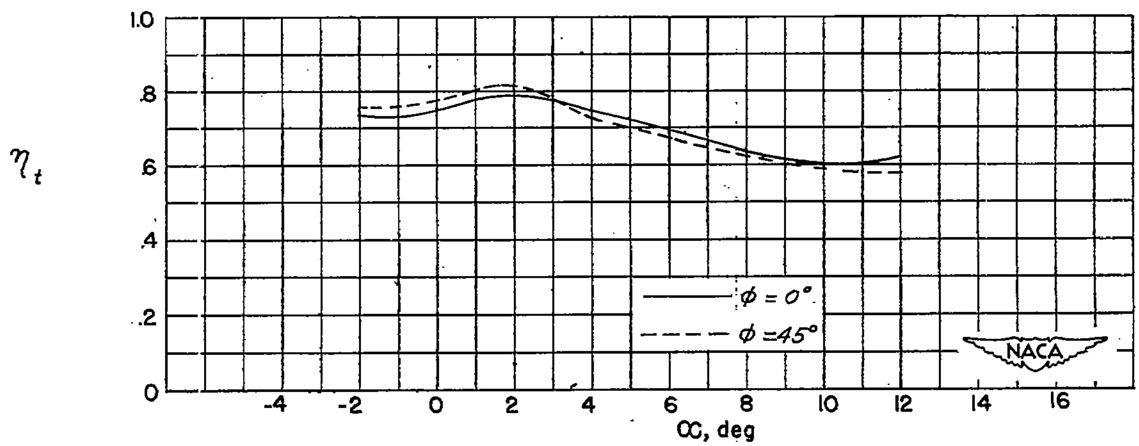

(2) Tail-lift efficiency factor variation for $BW_{3F}{}^{45}T_6$.

(a) $BW_{3F}{}^{45}T_6$.

Figure 30.- Center-of-pressure characteristics and body-wing-tail interference factors for configurations having W_3 and T_6.

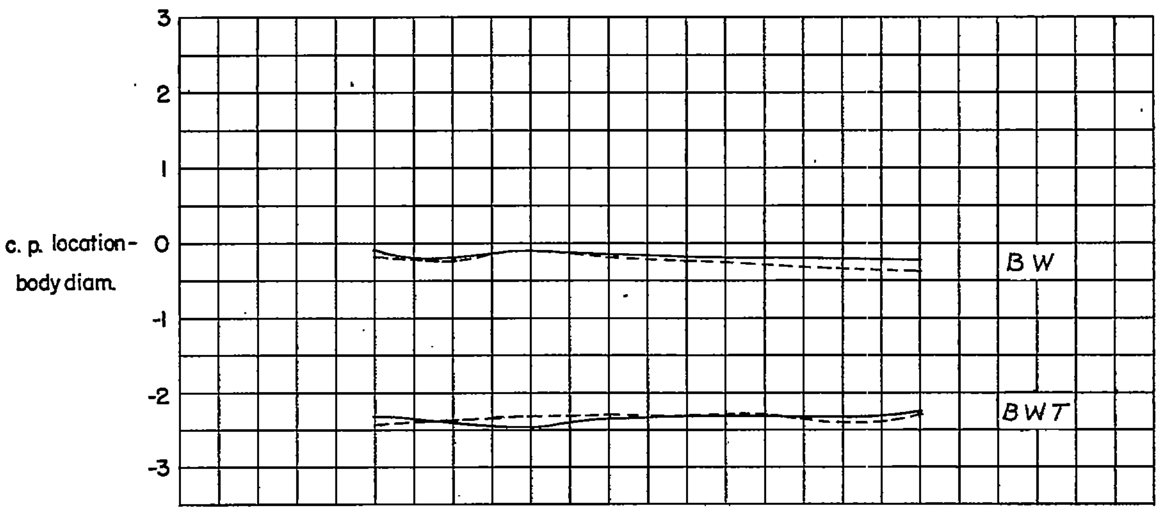

(1) Center-of-pressure variation for $BW_{3R}{}^{45}T_6$ and BW_{3R}.

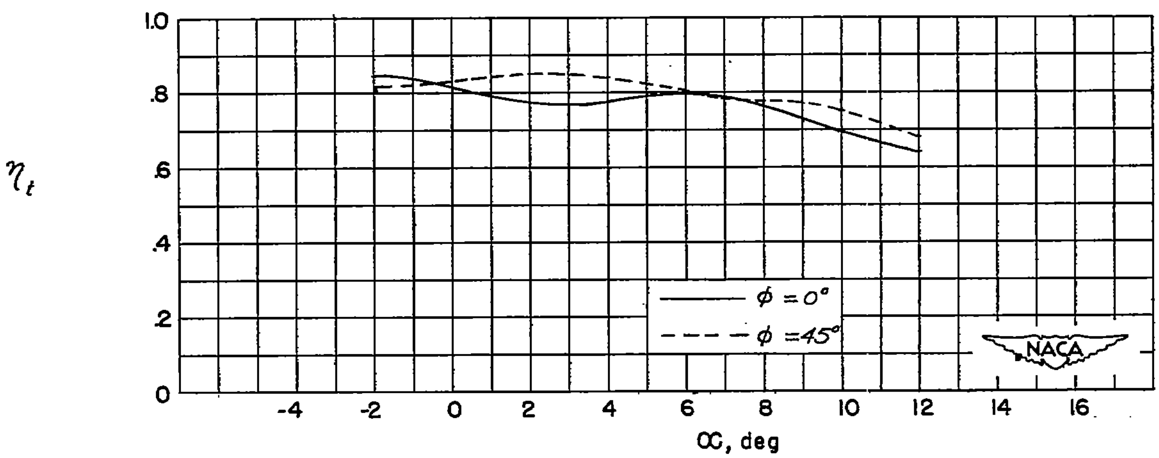

(2) Tail-lift efficienty factor variation for $BW_{3R}{}^{45}T_6$.

(b) $BW_{3R}{}^{45}T_6$.

Figure 30.- Concluded.

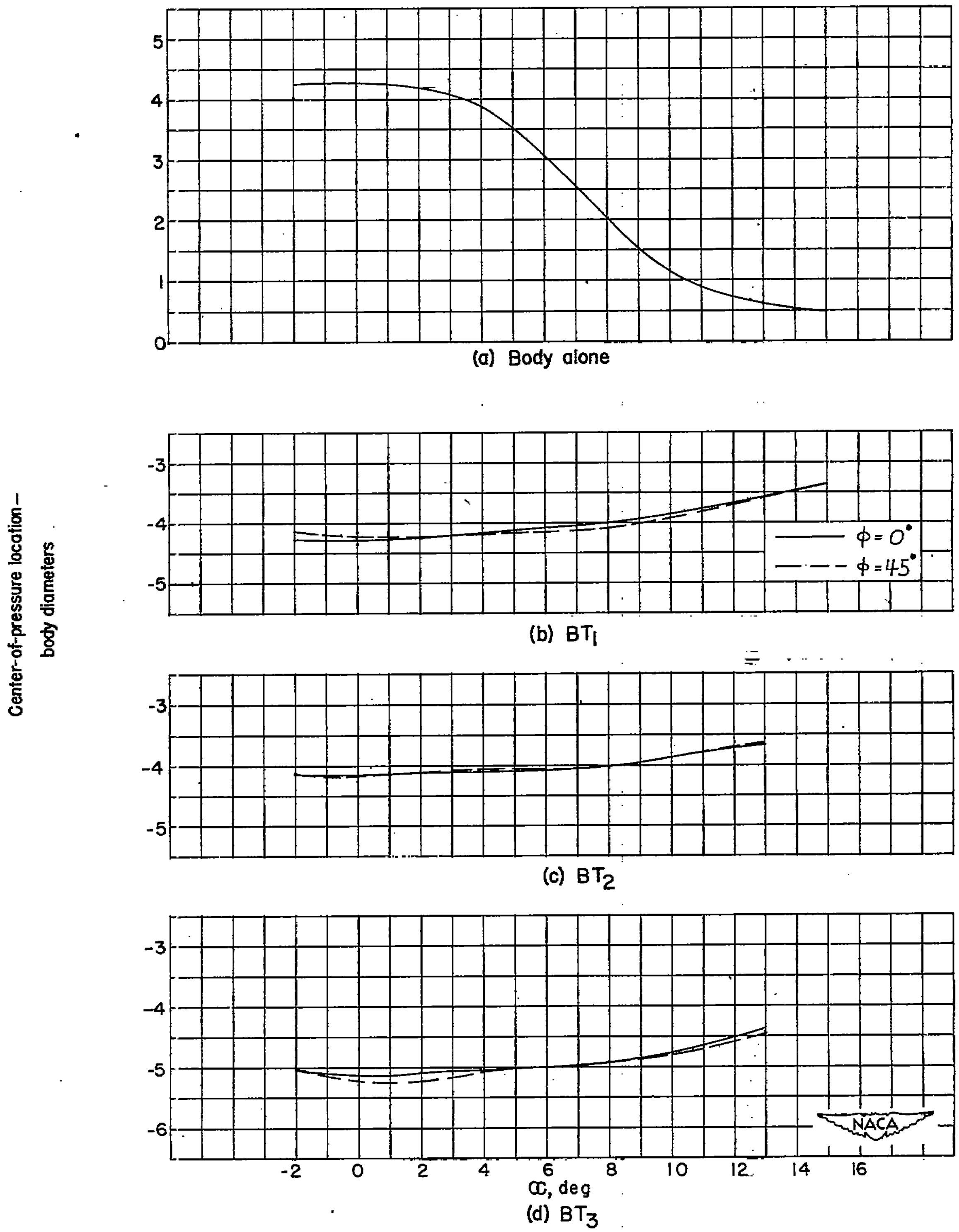

Figure 31.- Center-of-pressure characteristics of the body and BT configurations.

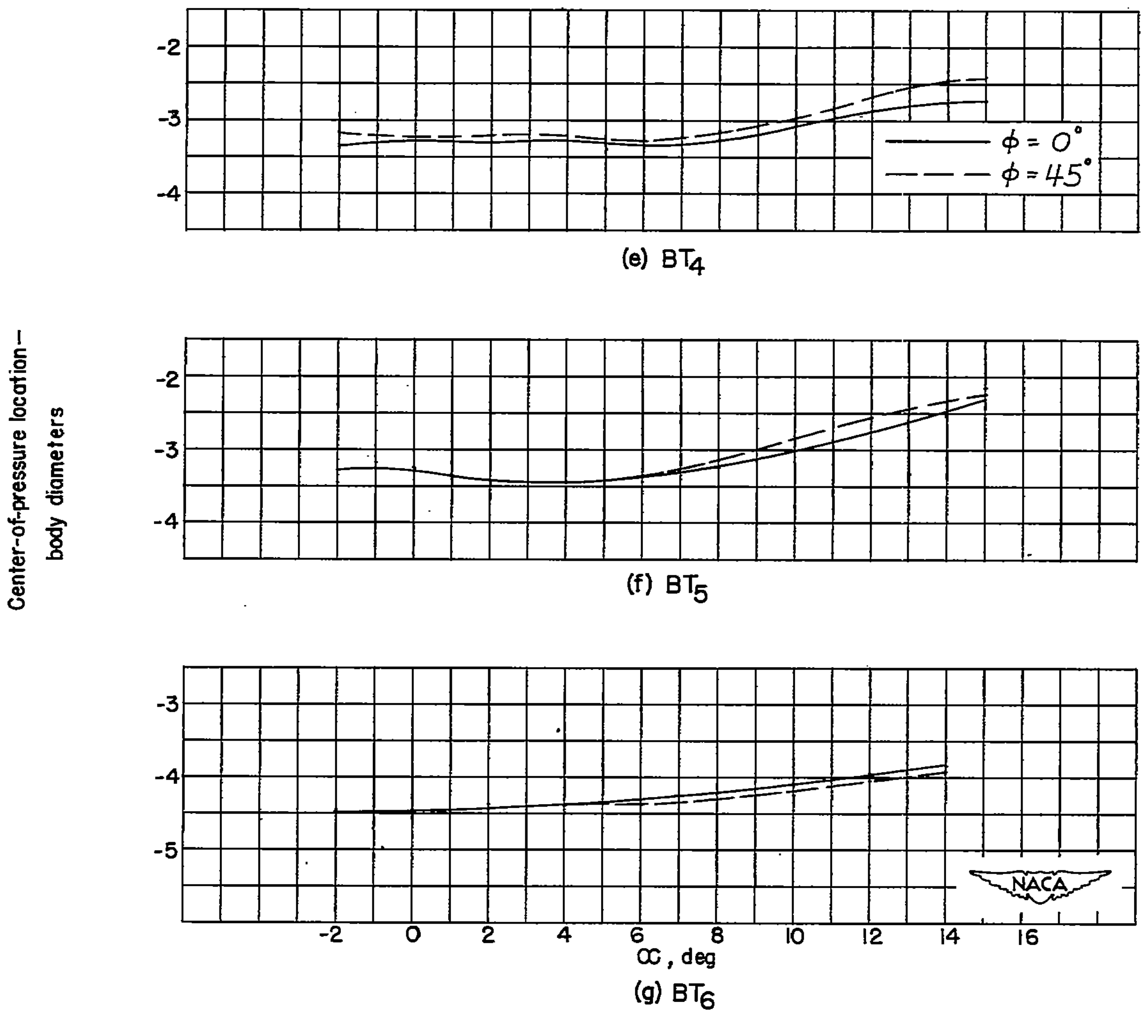

Figure 31.- Concluded.

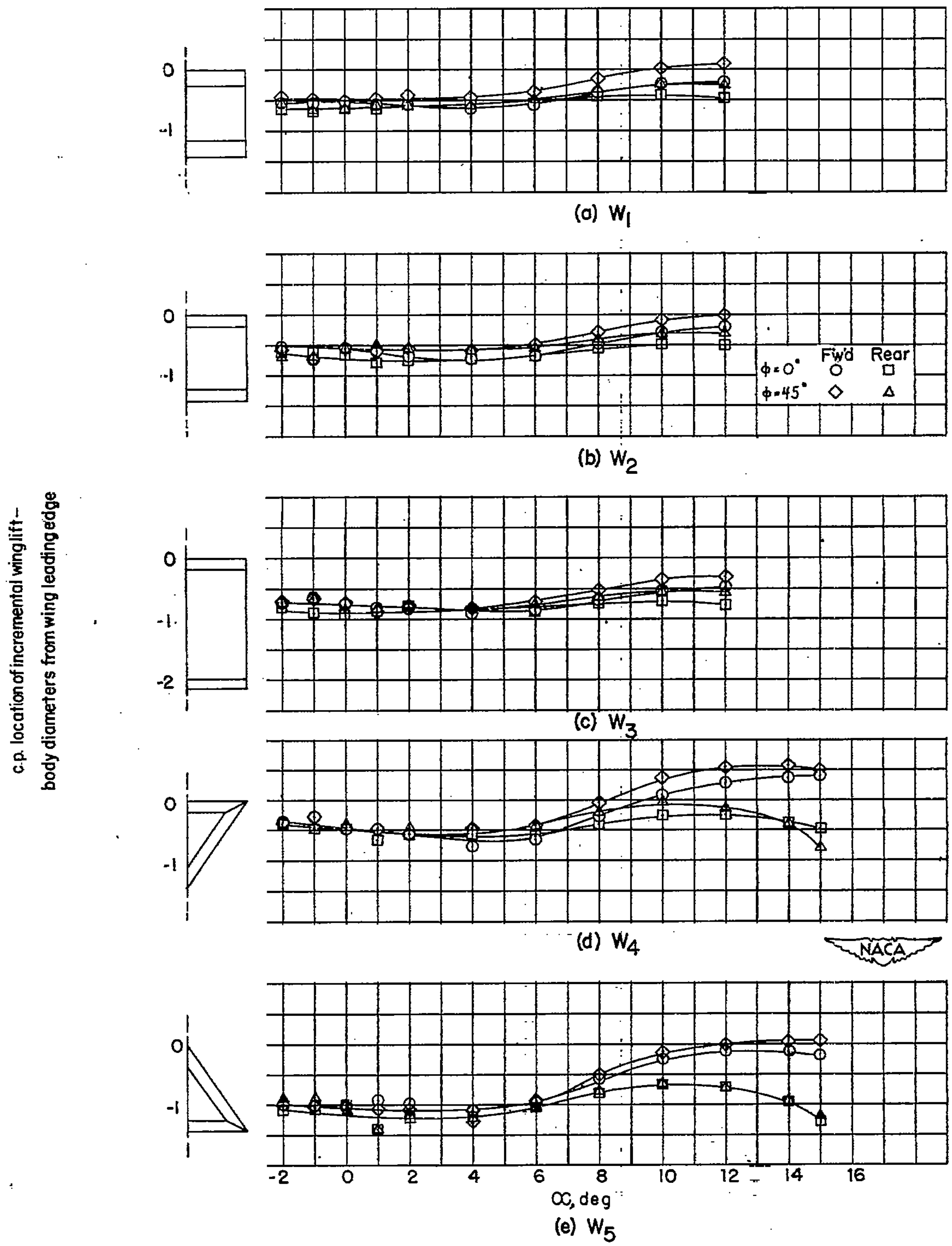

Figure 32.- Center-of-pressure characteristics of the incremental wing lift, $\dfrac{C_{m_{BW}} - C_{m_B}}{C_{L_{BW}} - C_{L_B}}$.